PhD-FSTC-2016-26
The Faculty of Sciences, Technology and Communication

DISSERTATION

Defense held on 06/07/2016 in Belval

to obtain the degree of

DOCTEUR DE L'UNIVERSITÉ DU LUXEMBOURG

EN PHYSIQUE

by

Tobias BERTRAM
Born on 06 February 1986 in Gießen, (Germany)

DOPING, DEFECTS AND SOLAR CELL PERFORMANCE OF CU-RICH GROWN $CuInSe_2$

Dissertation defense committee

Dr Susanne Siebentritt, dissertation supervisor
Professor, Université du Luxembourg

Dr Thomas Schmidt, Chairman
Professor, Université du Luxembourg

Dr Valérie Depredurand, Vice Chairman
Université du Luxembourg

Dr Wolfram Heimbrodt
Professor, Philipps Universität Marburg

Dr Johan Lauwaert
Professor, Universiteit Ghent

CONTENTS

ABSTRACT

Cu-rich grown $CuInSe_2$ thin-film solar cells can be as efficient as Cu-poor ones.
However record lab cells and commercial modules are grown exclusively under Cu-poor conditions. While the Cu-rich material's bulk properties show advantages, e.g. higher minority carrier mobilities and quasi-Fermi level splitting - both indicating a superior performance - it also features some inherent problems that led to its widespread dismissal for solar cell use. Two major challenges can be identified that negatively impact the Cu-rich's performance: a too high doping density and recombination close to the interface.
In this work electrical characterisation techniques were employed to investigate the mechanisms that cause the low performance. Capacitance measurements are especially well-suited to probe the electrically active defects within the space-charge region. Under a variation of applied DC bias they give insights into the shallow doping density, while frequency and temperature dependent measurements are powerful in revealing deep levels within the bandgap.
$CuInSe_2$ samples were produced via a thermal co-evaporation process and subsequently characterized utilizing the aforementioned techniques. The results have been grouped into two partial studies. First the influence of the Se overpressure during growth on the shallow doping and deep defects is investigated and how this impacts solar cell performance. The second study revolves around samples that feature a surface treatment to produce a bilayer structure - a Cu-rich bulk and a Cu-poor interface.
It is shown that via a reduction of the Se flux during absorber preparation the doping density can be reduced and while this certainly benefits solar cell efficiency, a high deficit in open-circuit voltage still results in lower performance compared to the Cu-poor devices. Supplementary measurements trace this back to recombination close to the interface. Furthermore a defect signature is identified, that is not present in Cu-poor material. These two results are tied together via the investigation of the surface treated samples, which do not show interface recombination and reach the same high voltage as the Cu-poor samples. The defect signature, normally native to the Cu-rich material, however is not found in the surface treated samples. It is concluded that this deep trap acts as a recombination centre close to the interface. Shifting it towards the bulk via the treatment is then related to the observed increase in voltage.
Within this thesis a conclusive picture is derived to unite all measurement results and show the mechanisms that work together and made it possible to produce a high efficient Cu-rich thin-film solar cell.

CHAPTER
ONE

INTRODUCTION

In a span of less than two hours, enough energy from the sun hits the surface of earth, to satisfy humanities' energy demands for a whole year [1]. In the year 2015, photovoltaics (PV) contributed 1.3 % of the global demand for electricity, with at least 227 GW installed capacity [2]. Even accounting for the finite conversion efficiency of solar to electric or thermal power, those two facts show that there is a nearly limitless potential resting in solar energy technology left to be utilized. The worlds growing need for sources of clean, sustainable energy is one of the great challenges of our time. Small scale PV installations can not only be installed much faster than any of the conventional power sources, but also offer electricity supply far-off the grid, an advantage for developing countries. There are indeed challenges associated with the availability of solar energy throughout the day, making research on new ways of energy storage, mobility and smart grids imperative. Despite this, PV in combination with other renewable energies could be able to fully replace fossil fuels, provided a worldwide effort is made and policy changes are put in place [3, 4]. However a number of economic incentives exist aside from the obvious ecological ones. Already today, out of the globally 8.1 million jobs in renewable energy, solar PV supplies a major share with a total of 2.8 million jobs in 2015 [5]. The price learning curve, which showcases average module price over cumulative production has shown a steady decline, due to scaling effects and advances in technology [6]. Furthermore, the energy payback time (EPT) of various PV technologies - namely the time it takes for a power plant to generate enough energy to offset the energy that went into production and installation of that certain plant - is very low, much lower than for conventional sources [6]. Especially thin-film technology shines in this regard, due to its low material usage with an EPT in the order of 1/10 of their lifetime, an advantage which has a potential for growth, with new low cost growth techniques being researched [7].

1.1. The case for Cu(In,Ga)Se_2 thin-film solar cells

Despite not being an ideal candidate for PV applications due to its indirect bandgap, silicon wafer technology dominates the PV market. Thin-film PV however has been able to take its share, with highly efficient modules becoming commercially available in recent years [6]. This work focusses on the chalcopyrite $CuInSe_2$(CIS), which was first developed in 1974 as an IR-photodetector at Bell labs [8] and optimized for the use in PV, reached an efficiency of 12 % one year later [9]. It has to be pointed out, that while this thesis focusses on the ternary, the commercial available absorber material is an alloy between

CIS and $CuGaSe_2$ (CGS). $Cu(In,Ga)Se_2$ (CIGS) has become the efficiency leader in thin-film PV, with lab record efficiencies of 22.3 % [10]. The advantages, which will be pointed out within this section where mostly studied on CIGS technology. However they are also important for the present study on CIS, since the ultimate goal going further from here will be to apply the findings on the ternary to CIGS, provided they merit repeating.
CIS is a direct semiconductor with a forbidden gap of around 1 eV [11–13]. Due to this, it is an excellent material for high efficiency single junction or tandem solar cells. Commercially available single junction modules are usually fabricated with an absorber layer, made from an alloy of $CuInSe_2$ and $CuGaSe_2$, in short CIGS. By this the bandgap can be increased, leading to larger open-circuit voltages. Furthermore it features a high absorption coefficient in the range of 10^5 cm^{-1} [13] over most of the visible spectrum. Therefore $Cu(In,Ga)Se_2$ layers can be grown very thin compared to standard silicon wafer technology. This allows for the growth on flexible substrates, which has not only been shown successfully, but even yielded world-record efficiencies [14]. Growth on foils does not only allow for new deposition methods and storage concepts, but due to the ability of being rolled $Cu(In,Ga)Se_2$ also supplies the most power per weight of all thin film technologies with 919 W/kg specific power [15]. Resulting in another potentially huge factor for reducing cost and EBT for this technology, since framing and glass substrate play a big part in both [6].
Rooftop PV has the smallest environmental impact of all renewable energy technologies, since it requires no additional land usage like any free standing power sources would [16]. Lighter, frameless thin film PV will allow for easier deployment on existing structures, which is another advantage of $Cu(In,Ga)Se_2$. This is even more important for applications beyond terrestrial, as mass is a big cost factor associated with the logistics of transport into orbit. But a reduction of weight and storage space are not the only unique abilities, which make it a very interesting material in this sector, i.e. as a power supply for satellites. For one, it exhibits an exceptional resistance against radiation damage, which allows for greatly increased module lifetimes, once exposed to the conditions of high-energy particle bombardment outside the earth's atmosphere and magnetic field. Irradiation tests with electrons of 1 MeV show a radiation hardness of at least one order of magnitude higher than any other PV technology [17]. This self-healing ability can be explained by the mobility of defects and formation of complexes [18, 19]. Back on earth, this ability also provides exceptional stability in outdoor tests [20].
All this together shows that $Cu(In,Ga)Se_2$ is a very versatile material for solar cell use. However, CIGS still lags behind the efficiency records of Si wafer technology. One key difference between the two technologies is that, while Si can be made virtually defect free and subsequently doped with the right element in order to create shallow defects within just the right energy range at just the right concentration, the case is very different for CIGS. As an intrinsically doped material, CIGS features a wide range of defects even without the addition of foreign elements. Therefore a number of parameters during the growth of the absorber determine the formation and profile of the different defects in the absorber layer. Understanding these defects, especially their position within the bandgap as a function of different growth parameters, is crucial in order to produce better solar cells. In section 2.1 the material CIS will be discussed with a focus on its intrinsic defects, paying special attention to the advantages of CIS grown under an excess of copper. However, this material also features a number of challenges, which reduce final device performance and can be traced back to its electrical properties. The aim of this study is to characterize those properties and find ways to overcome these challenges.

1.2. Electrical measurements on solar cells

There is a number of semiconductor characterization techniques that focus on defects, both electrical and optical methods. An advantage of electrical measurements is that they are inherently performed on fully finished solar cell devices. This means they can be employed under conditions very close to how a device would operate normally. Admittance measurements (first introduced by Losee [21]) is the technique to measure the capacitance of a solar cell under different alternating current (AC) frequencies. Variation of the device temperature allows for measurements of shallower defects, which is then called thermal admittance spectroscopy (TAS). With this technique one can probe the density of states within the band gap and thereby deduce defect energies and capture cross-sections. However, this is not a trivial technique and knowledge about many device parameters is crucial in order to be able to interpret the gathered data properly.
Current-voltage curves under the variation of temperature (IVT) can help to find fundamental, macroscopic parameters of the device, especially the resistance in series and parallel to the device. An equivalent circuit model can be calculated from these two. This is important, as the capacitive response of such a circuit can interfere with the measurement.
Capacitance-voltage measurements (CV) are performed by measuring capacitance at fixed frequency and temperature under a variation of the external bias voltage. They can be used to determine the built-in voltage and density of free carriers and thereby gain insights into the width of the space-charge region (SCR). These quantities are in itself important for device characterization, but also are needed in order to perform the defect density evaluation of admittance measurements. In chapter 2.3 the utilized characterization techniques are described in-depth. This is then followed by chapter 3 about the growth and sample structure of the studied devices.

This thesis mainly comprises two studies, both of which address problems of Cu-rich grown CIS solar cells whose origins are revealed via electrical characterization methods. The first study investigates the influence of the Se supply during absorber growth on the doping density (chapter 4) and finds a new defect native to the Cu-rich material. The second study is focussed on absorbers, which are grown Cu-rich with an ex-situ In-Se surface treatment (chapter 5), delivering solar cells on-par with the Cu-poor material. A mechanism how this treatment improves solar cell performance is then proposed.
The last chapter (6) summarizes all results gathered in this thesis and aims to give an outlook as to how to proceed from here.

CHAPTER

TWO

THIN-FILM SOLAR CELL BASICS AND CHARACTERIZATION

The purpose of this chapter is to introduce the fundamentals of thin-film solar cells based on $CuInSe_2$ and their characterization by electrical measurements. It will form a concise theoretical background, which enables the description and interpretation of the data, generated within the framework of this thesis. It is divided into three sections with the first (2.1) focussing on the properties of the absorber material, the second (2.2) describing the fundamental physics behind photovoltaic cells and their operation, and the third (2.3) will introduce the different methods of electric characterization, which were applied during this study.

2.1. The chalcopyrite $CuInSe_2$

2.1.1. Crystallography

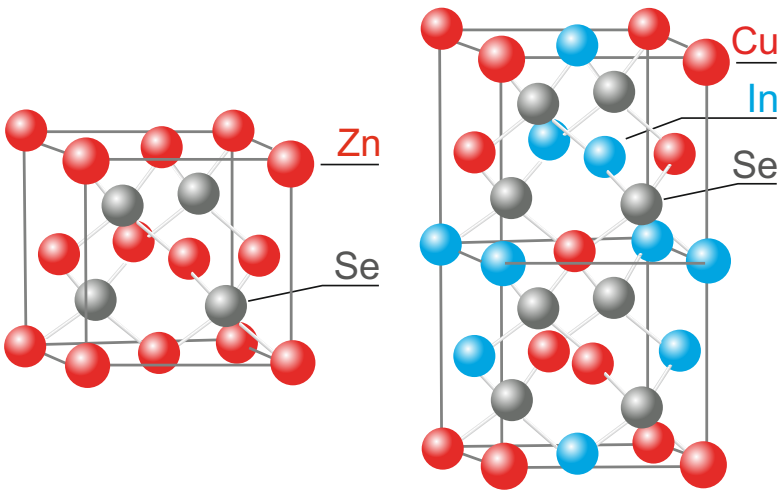

Figure 2.1.: ***Zincblende and chalcopyrite crystal lattic*** *- The chalcopyrite structure is formed by two zincblende unit cells on top of each other. Modified version, from [22]*

The preferred structure for photovoltaic applications of the I-III-VI_2 semiconductor $CuInSe_2$ (CIS) is the chalcopyrite crystal structure (α-phase). This structure is essen-

tially formed by two zincblende unit cells sitting on top of each other, this is illustrated in figure 2.1. It fills a cuboid with quadratic base of a = 5.784 Å and height of c = 11.616 Å. The bond lengths are then: $d_{Cu\text{-}Se} = 2.484$ Å and $d_{In\text{-}Se} = 2.586$ Å. The first X-ray diffraction (XRD) measurements of the lattice parameters were published by Hahn *et al.* [23], however the here given values are from later XRD measurements [24], confirmed by extended X-ray absorption fine structure [25]. One characteristic of this semiconductor is its wide existence range, from very Cu-poor to stoichiometric growth it can form a stable α-phase. This is due to the ability of defects to form complexes, which stabilize the crystal lattice. Especially the defect pair consisting of two Cu vacancies and an In-on-Cu antisite ($2V_{Cu}$+In_{Cu}) has a very low formation energy [26].
The phase diagram [27] is shown in figure 2.2, a number of additional phases appear in the various temperature and composition regions.
The diagram displays the growth temperature on the ordinate and In content on the ab-

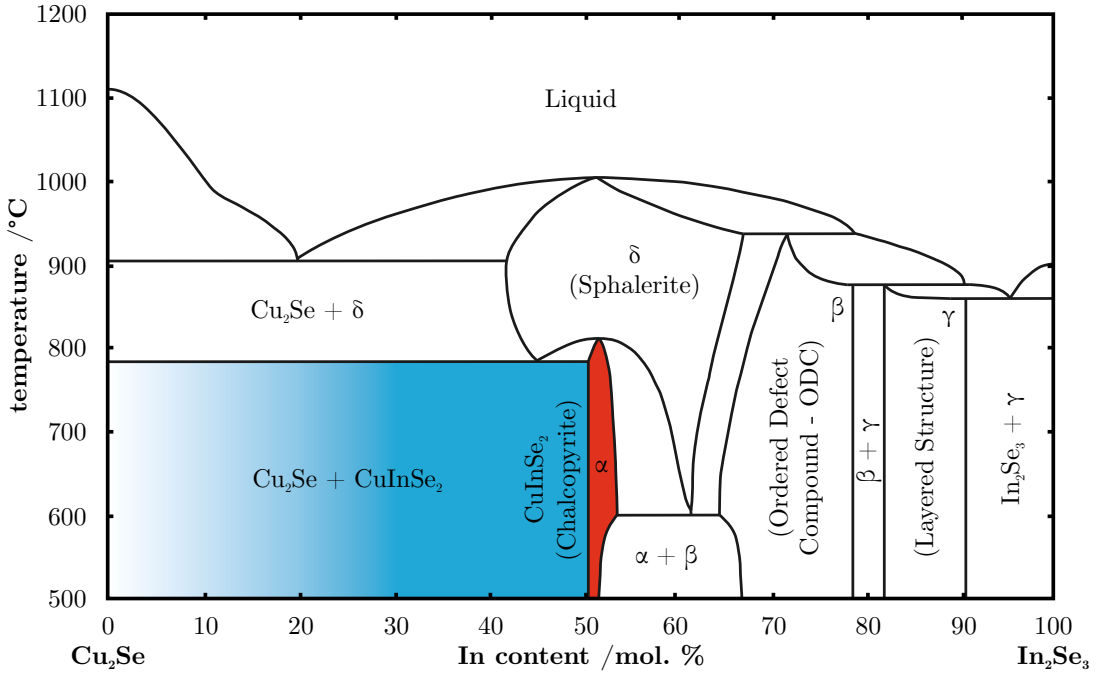

Figure 2.2.: ***Pseudobinary phase diagram of CIS*** *- The Cu-rich and Cu-poor $CuInSe_2$ composition ranges have been highlighted blue and red respectively. All the samples, shown in this thesis, fall in the coloured regions of the diagram. The growth temperature is plotted on the ordinate and In content on the abscissa. Reproduced from ref. [27].*

scissa, therefore Cu-rich compositions are left from the centre of the graph. An important note is, that a phase separation occurs for Cu contents above stoichiometry and the excess is absorb into a secondary Cu_xSe phase, which grows on top of the α-phase [28]. This Cu_xSe is highly conductive and has to be etched away, before solar cell finishing. Therefore the term Cu-rich in the context of solar cells refers to material, which was grown with a secondary phase that was removed afterwards. However the given Cu/In-ratios for Cu-rich solar cells, which are above one, always refer to the material before etching.
The additional phases are outside the temperature and composition ranges, utilized for sample growth within this thesis, therefore they will only be treated rather quickly in the following. Despite the fact that for conventional PV use, CIS is usually grown Cu-poor, there is still a lot dispute over the In-rich region of the phase diagram. A number of compositions and lattice structures have been proposed for this β-phase, which sometimes

called "ordered defect compound" (ODC) . There is however the wide agreement that this ODC layer grows on top of the chalcopyrite and might be important for the high performance of Cu-poor devices [29].
At even higher Cu-deficiencies the γ-phase becomes dominant, which has a composition of $CuIn_5Se_8$. This phase marks a structural transition of the Se sublattice from the chalcopyrite, in which the Se sublattice is face-centred cubic, to the hexagonal stacked ordering in In_2Se_3. The γ-phase is then a layered structure of partial hexagonally close packed Se anions.
Additionally at high temperatures there is the δ-phase, which grows in the sphalerite crystal structure. However this phase becomes unstable with decreasing temperature and decomposes into a mix of α and β.

Advantages of Cu-rich grown $CuInSe_2$

There are a number of studies on the material properties of Cu-rich grown $CuInSe_2$. The crystal quality in general is higher in Cu-rich, than Cu-poor $CuInSe_2$. In polycrystalline $CuInSe_2$ this is exhibited by the larger crystal size in Cu-rich material. As mentioned previously the Cu-poor material is stabilized by vacancy and antisite defects, which allows for high Cu deficits, while the Cu-rich growth mode yields two phases: stoichiometric $CuInSe_2$ and Cu_xSe, which growths mostly on the top of it. This fact indicates a better material quality and less defective structure for $CuInSe_2$ grown under Cu-excess. Positron annihilation Doppler broadening spectroscopy experiments on epitaxial samples have confirmed different vacancy type defects in Cu-rich and Cu-poor material. For the Cu-rich samples only Cu vacancies could be detected, while below stoichiometry the double vacancy of Cu and Se dominates [30] . Furthermore, these double vacancies show metastable behaviour, leading to voltage and light bias dependant effects.

As shown by Hall measurements on epitaxially grown $CuGaSe_2$ [31], the mobility of free charge carriers shows an increase for material grown with Cu/In-ratios above 1. Unfortunately there are no comparable studies on Cu-rich grown $CuInSe_2$, but measurements of Cu-poor single crystals found very low mobilities in the Range of $4 - 60\ \frac{cm^2}{Vs}$ [32] in p- and n-type material, $4\ \frac{cm^2}{Vs}$ [33] (only p-type). In recent years there have been more studies on the mobility in $CuInSe_2$ by optical pump terahertz spectroscopy [34]. They find very high mobilities of photoexcited electrons at room temperature of $1000\ \frac{cm^2}{Vs}$ for stoichiometric material. A comparison to Cu-poor material shows them to be much lower in the latter at only $200\ \frac{cm^2}{Vs}$ [35]. It can be deduced that Cu-rich $CuInSe_2$ has a high advantage in transport properties.

The optical properties also show a number of advantages. Studies by excitation power calibrated photoluminescence on bare $CuInSe_2$ reveal that the quasi-Fermi level splitting increases profoundly above the stoichiometry point [36]. Furthermore degradation of these samples under air exposure is severely reduced in Cu-rich compared to Cu-poor samples [37]. Unfortunately these advantages are negated, when measuring $CuInSe_2$-absorber, which have been coated with a CdS-buffer layer. For these samples the quasi-Fermi level splitting is consistently higher in the Cu-poor ones and degradation is halted independent of Cu content [37]. This highlights the importance of the interface, in chapter 5 Cu-rich samples with a Cu-poor layer (description of the surface treatment in section 3.3) were investigated to address this issue.

2.1.2. Native electrical defects

In contrast to the classical semiconductor Si, $CuInSe_2$ has the advantage that it can be doped through native point defects, i.e. without adding foreign dopants into the crystal structure. Furthermore it is an amphoteric material, meaning that its majority and minority carrier concentrations can be changed with composition, for example as shown by Noufi *et al.* [38] reduction of the Selenium/Metal (Se/Me) flux ratio leads to majority inversion from p- to n-conductivity.
The different possible types of native defects are shown in fig. 2.3. They are:

- Vacancies: Missing atoms in the crystal structure, they are V_{Cu}, V_{In} and V_{Se}.
- Antisites: Atoms that are on the wrong spot of the lattice: In_{Cu}, Cu_{In}.
- Interstitials: Atoms that are in between grid sites: Cu_i, In_i and Se_i.

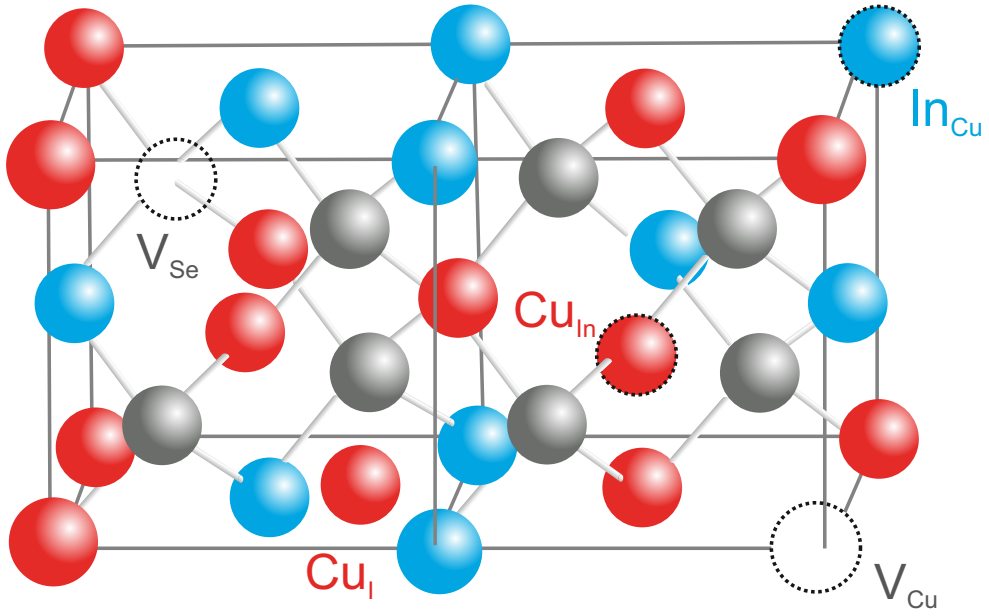

Figure 2.3.: ***Native point defects in CIS*** *- Ideal crystal of $CuInSe_2$ (left) vs. structure showing a number of native point defects (right)*

Still many fundamental facts about the native defects are unknown, it is therefore unclear which are prevalent in samples of differing composition and their effect on the optoelectronic properties and ultimately the solar cell characteristics. Numerous theoretical and experimental studies have been trying to shine a light on the native defects in $CuInSe_2$, but so far it has not been possible to create a congruent model which describe the measured defect energies. In the following there will be a summary of some results from experimental methods and the defect calculations and where these overlap and differ. As an optical characterization method, photoluminescence measurements can give an insight into the radiative recombination processes which govern the absorber materials' properties. Some general trends that are observed in photoluminescence studies of the Cu-poor material are a high level of compensation [39] and Urbach tailing. These effects are generally seen in the spectra as very broad, asymmetrical peak-shapes of the PL-transitions at

low temperatures. Contrary to this, Cu-rich material shows very sharp, Gaussian peaks for the high temperature band-to-band transition [37] and a multitude of excitonic and donor-acceptor transitions at low temperatures [40]. Regarding defect energies, there has been some controversy about the attribution of low temperature PL-transitions to native defects in $CuInSe_2$ [40]. In the cited work $CuInSe_2$ samples of varying compositions from Cu-excess to deficiency are investigated with temperature and excitation intensity dependant PL measurements. They identify two donor-acceptor pairs plus an excitonic transitions, which is only visible in the Cu-rich samples. A model is then proposed, which consists of two transitions involving the same shallow donor, that is about 10 meV below the conduction band edge. The two acceptors, dubbed 'A1' and 'A2' are at 40 meV and 60 meV above the valence band, respectively. The first one is found in material, which was grown Cu-poor or slightly Cu-rich, while the second only appears in that of high Cu-excess [40]. Results from optical and electrical measurements are not congruent due to reasons that will be explored deeper in chapter 2.3.5. Historically two signatures, which were reported frequently for a number of different samples - the so-called 'N1' and 'N2' defect, stand out and their nature has been discussed to a great extend. Krysztopa *et al.* have compiled an overview of different publications regarding a number of electrical measurement methods on Cu-rich, Cu-poor, polycrystalline and epitaxial samples with the reported activation energy and thermal pre-factor of different defect signatures [41]. There have been a number of theoretical studies on the topic of defects in $CuInSe_2$, with widely varying results regarding the values of defect energies. Commonly a mixture of density functional theory (DFT) and Hartree-Fock (HF) calculations are employed to accurately describe bandgap values of the evaluated semiconductor, these calculations are then called hybrid density functionals. This is due to the fact that DFT usually returns too small bandgap values, while HF calculations overestimate it. A widely used approach was proposed by Heyd, Scuseria and Ernzerhof(HSE) [42], in which they introduce a screened Coulomb potential into exchange term of the HF calculation, thereby effectively reducing its range. The Coulomb screening strength and length can be adjusted to reproduce the known bandgap of a studied material. Another advantage of this approach is considerably less computational costs, compared to pure DFT calculations [42]. Some studies, that use this approach have been published by Pohl *et al.* [43], Oikkonen *et al.* [44] and Bekaert *et al.* [45], but results are rather disputed.

The first study [43] calculates four defects with low formation energies, with In_{Cu} as a very shallow donor abundantly present under all process conditions. Also independent of growth conditions appear V_{Cu}, a very shallow acceptor (< 50 meV, main dopant) and Cu_i, which they find to also be very mobile and the driver of Cu-migration and metastable effects [46]. Finally there is Cu_{In}, a slightly deeper hole trap whose concentration depends on the growth parameters.

In contrast to previous literature they find the binding energies of defect complexes with Cu-vacancies to be very low and generally state that their calculations suggest that those are not present in measurable quantities in the CIS material. Same goes for V_{In}, V_{Se}, In_i, Se_i to whom they also ascribe high formation energies and therefore low concentrations.

In the second work [44] they find the Cu-vacancy to have the lowest formation energy of all vacancies, but with no defect ionization levels within the bandgap. A little bit higher formation energy, the Se-vacancy contributes an acceptor state at 0.85 eV. The In-vacancy features the highest formation energy in nearly all growth conditions and also has no level within E_g [47]. Both cation antisite defects' formation energies are highly dependent on the growth conditions, but become very low under high Cu-or In-excesses, respectively.

The Cu-interstitial also has a low formation energy in contrast to the In-interstitial [48], Se_i is possible and they assign a shallow acceptor level to the Se-Se dumbbell, meaning a comples out of a Se-interstitial and a Se lattice atom [49]. Generally they argue in favour of defect complexes, the argument being that the low binding energies found for calculations in thermodynamic equilibrium, don not reflect thin film growth conditions and kinetics have to be taken into account. Their defect complexes are electrically passive, with the exception of Se-vacancy containing complexes that are electron traps.
According to the last reference [45] the In-on-Cu antisite is a shallow donor, while Cu-and In-vacancy and Cu-on-In antisite are shallow acceptors. A special point is made to look at the influence of the cation stoichiometry on defect formation energies. In increasingly In-rich (which they say is also equivalent to Se-poor) conditions, the formation energy of In-on-Cu is decreased, while under In-poor growth In-on-Cu antisite and Cu-vacancy defects are more abundant and the Cu-on-In antisite is less. At high Cu-excesses Cu_{In} surpasses V_{Cu} and becomes the dominant acceptor, leading to the high doping in Cu-rich. However, they neither discuss Se-related defects, nor complexes.
This shows that also from a theoretical point of view, there is still a lot that has not been fully understood about the defects in CIS.

2.2. Photovoltaic devices

To achieve their purpose of generating energy a number of processes have to go on within a thin-film solar cell. First, charge carriers have to be generated through the absorption of photons, then a separation of those charges has to occur and finally charge extraction needs to take place, to get the positive and negative carriers into their respective terminals. The basic structure of all the cells described in this work consists of a diode, which rectifies the photo current that is generated within the absorber layer and allows charges to pass to their respective terminals. In the following section semiconductor junctions and their basic physics will be discussed.

2.2.1. Semiconductor junctions

As described in the last chapter doping can be utilized to form shallow defects in the semiconductor material. At room temperature there is enough thermal energy available to ionize these defects, which leads to a contribution of free carriers in the bands. The nature of the dominant defects determines the conductivity type of the semiconductor, shallow acceptors eject holes into the valence band resulting in p-type material, while shallow donators release electrons into the conduction band to form an n-type conductor. Most semiconductor devices are based on the joining of a p- and an n-type material into a so-called pn-junction. Depending on the utilized materials, alignment of the respective bands can vary, resulting in different types of interfaces. Generally one differentiates between homojunctions, which are formed by the contact between two differently doped parts of the same material, and heterojunctions between two different materials with different bandgap energies. For the later one discriminates three different types of alignments [50], they are depicted in figure 2.4:

- Type I: (Straddling) The bandgap energy of the narrow-gap material lies fully within the energy range of the forbidden zone of the wide-gap material.
- Type II: (Staggered) The energy ranges of both materials are overlapping partially.

- Type III: (Broken) There is no overlap of band gap ranges.

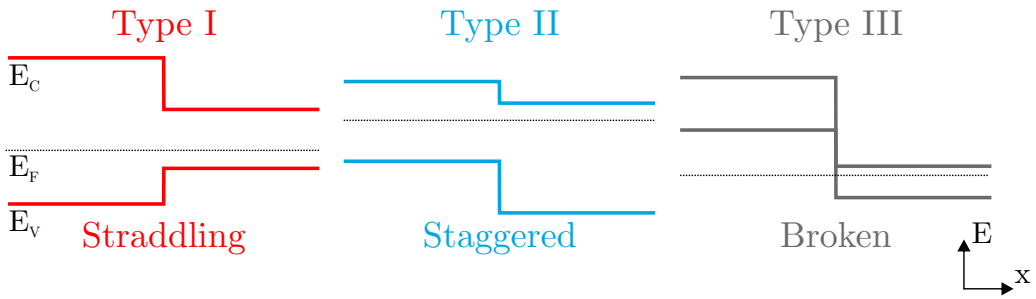

Figure 2.4.: ***Heterojunction classification*** *- Depiction of the three different types of semiconductor heterojunctions.*

The physics of pn-junctions are discussed in depth by Peter Würfel [51]. If not differently stated, the information given in this section and the next is taken from that reference and for easier illustration is derived for a homojunction. Two conditions describe the junction in thermal equilibrium with the 300 K background radiation, without an external energy supplier.

- No charges are flowing through the junction, therefore $J_Q = 0$.
- The electrochemical potentials of electrons μ_n and holes μ_p are in equilibrium with the surrounding background radiation, $\mu_n + \mu_p = 0$.

There are two driving forces, that act on the charge carriers, a diffusion and a field force. Both of these forces can be combined into the electrochemical potentials μ and conductivities κ, therefore the current can be written as:

$$J_Q = \frac{\kappa_n}{q_e} \cdot \mathrm{grad}(\mu_n) - \frac{\kappa_h}{q_e} \cdot \mathrm{grad}(\mu_p), \tag{2.1}$$

with q_e, the elementary charge. From the two conditions then follows that:

$$J_Q = \frac{\kappa_n + \kappa_h}{q_e} \cdot \mathrm{grad}(\mu_n) = 0. \tag{2.2}$$

Since the sum of the conductivities is not equal to zero it follows that the gradients of the electrochemical potentials (of both electron and holes) throughout the device have to be zero. In other words this means that in equilibrium the Fermi level is flat throughout the pn-junction. Due to the fact that different p- and n-type materials usually don't have the same Fermi levels a potential difference between both sides arises, as soon as contact is made. This is the built-in voltage V_{bi} (as illustrated in figure 2.5), it can be understood as follows: when contacting the neutral p and n-type materials, the difference in their electrochemical potentials leads to a diffusion current of electrons from the n-side and holes from the p-side, which results in a spatially fixed charge (positive on the n-side and negative on the p-side) until the electrochemical potentials are equalized and the Fermi level is flat throughout the junction. We can link the built-in voltage to the density of donors from the n-side N_d and acceptors from the p-side N_a [50].

$$V_{bi} = \varphi_n - \varphi_p = \frac{k_B T}{q_e} \cdot \ln\left(\frac{N_d \cdot N_a}{{N_i}^2}\right), \tag{2.3}$$

with the intrinsic carrier density N_i=N_d+N_a. The potential difference φ across the junction is linked to the charge distribution ρ by Poisson's equation. Since the interface area is much larger than the space-charge region width, this can be simplified to one dimension

$$\text{div } (\text{grad}(\varphi)) = \frac{d^2\varphi}{dx^2} = -\frac{\rho}{\epsilon_0 \epsilon_r}. \tag{2.4}$$

Assuming a constant and rectangular space-charge distribution on either side of the junction, the solution of this differential equation can be found, a schematic depiction of this is shown in figure 2.5.

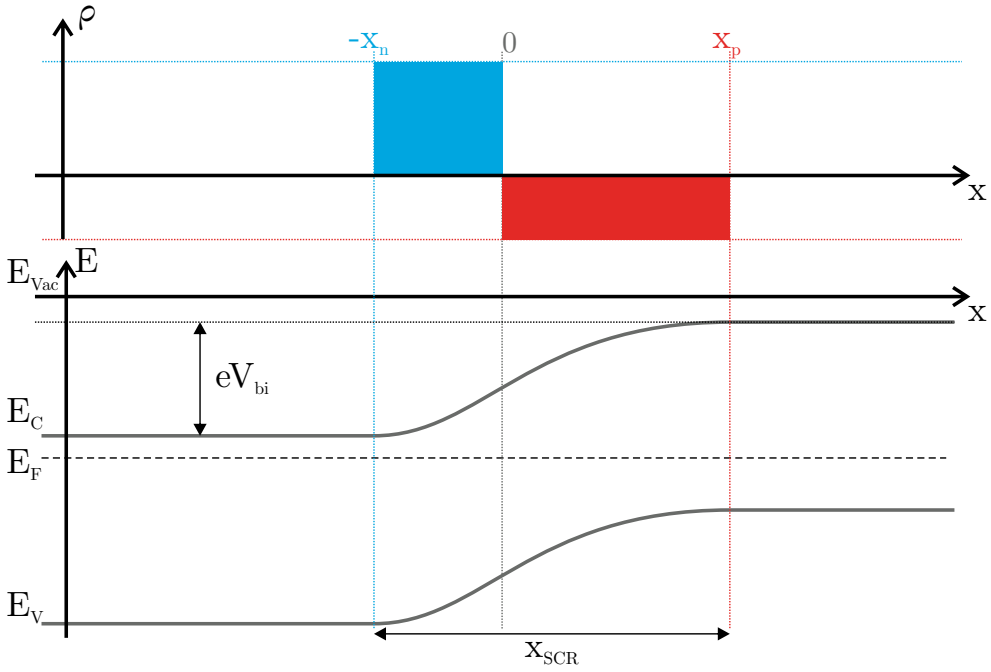

Figure 2.5.: ***Rectangular space-charge distribution and resulting banddiagram*** *- Schematic of the bandbending in a pn-homojunction with a positve constant space charge on the n-side and a negative one in the p-region, E_{vac} is the vacuum level.*

To achieve charge neutrality the sum of charges on both sides of the junctions has to cancel each other out, therefore the width on either side can be written as:

$$x_p = \frac{N_a}{N_d} \cdot x_n. \tag{2.5}$$

The total space-charge region width can be written as:

$$x_{SCR} = x_n + x_p = \left(1 + \frac{N_a}{N_d}\right) \cdot x_p. \tag{2.6}$$

With the boundary condition that the electric field is zero at the edges of the space-charge region, the potential is there equal to the respective bulk values and the charge densities are constant, integration of Poisson's equation yields:

$$x_{SCR} = \sqrt{\frac{2\epsilon_0 \epsilon_r}{q_e} \cdot \frac{N_a + N_d}{N_a N_d} \cdot V_{bi}}. \tag{2.7}$$

It becomes directly apparent, that for an asymmetric pn-junction the space-charge region extends much deeper into the lower doped side. This is usually the case for thin-film solar cells: the n type window layer is much more highly doped than the absorber, therefore $N_a << N_d$. For this reason it is valid to make the assumption of a one-sided pn-junction, which is used as the base for most capacitive measurement techniques and will be utilized in the framework of this thesis. The equation then reads:

$$x_{SCR} = \sqrt{\frac{2\epsilon_0\epsilon_r}{q_e} \cdot \frac{V_{bi}}{N_a}}. \tag{2.8}$$

2.3. Electrical characterization

Electrical characterization as a means of investigating solar cells offer a wide variety of measurement methods, which allow insight into many aspects and parameters of the finished devices. They range from very basic techniques that quantize macroscopic properties, for example current-voltage measurements, to advanced techniques, which probe the microscopic defect distributions within the solar cell devices like thermal admittance spectroscopy. The advantage of electrical characterization methods is, that they generally don't require very sophisticated or expensive equipment and can be performed under a number of conditions namely device temperature, illumination and voltage bias, which can be easily tuned in order to obtain the quantities to be measured. Though the measurements mostly utilize rather basic tools, their evaluation and interpretation is not always straightforward and care has to be taken in order to choose the right models and assumptions.

2.3.1. Temperature dependent current-voltage analysis

One very basic but nonetheless important analysis technique that can be performed on a finished device is the measurement of the current under an applied bias voltage. These measurements result in the current-voltage (IV) curves, from which a number of essential solar cell parameters can be extracted, namely the power conversion efficiency (η), fill factor ($\mathcal{FF}$), short-circuit current density (J_{SC}) and open-circuit voltage (V_{OC}). They can be performed under different temperature and illumination conditions. For comparability the parameters are usually extracted under an irradiance of 1000 $\frac{W}{m^2}$ with an air mass 1.5 spectrum (A.M 1.5) at room temperature. This spectrum is an approximation to the sun spectrum at ground level.

The governing equation which describes the dependence of the current density J_{light} on the applied voltage V under illumination is [52]:

$$J_{light}(V) = J_0 \left(e^{q_e \frac{V - J_{light} R_S}{A k_B T}} - 1 \right) + \frac{V - J_{light} \cdot R_S}{R_{Sh}} - J_{SC} \cdot \Gamma(V). \tag{2.9}$$

This 1-diode model describes the solar cell as a diode parallel to a current generator J_{SC} in reverse direction and shunt resistance R_{Sh}, which represents losses over the diode. Losses due to contacts, that occur in forward direction are represented by the series resistance R_S. It is dependant on the diode quality factor A and saturation current density J_0, which describe the underlying recombination mechanisms in the junction, as well as the measurement temperature T. The constants q_e and k_B are the elementary charge and

Boltzmann constant, respectively. A well-behaved solar cell should exhibit quality factors below 2. If the quality factor shows a strong increase with decreasing temperatures, this might be due to tunnelling enhanced recombination close to the interface. Furthermore, to allow for the superposition principle to be valid (which states that the total current density can be written as the sum of the diode and photo current densities), the last term is given by the external collection efficiency Γ times J_{SC}. Γ is a function of the applied voltage and can also be illumination dependent, usually it is set to be unity at zero bias, henceforth the photo-current term is equal to the short-circuit current density.

The basic parameters that are used to compare the performance of solar cell devices can be directly extracted from the current voltage curves. The intersections with the axes yield the short-circuit current density and the open-circuit voltage, so the current that can be extracted without an applied bias and the voltage without external load. The peak position of the product between current density and voltage is the maximum power point P_{max}, which has been illustrated in figure 2.6. With these three quantities the fill factor can be calculated as:

$$\mathcal{FF} = \frac{P_{max}}{J_{SC} \cdot V_{OC}}. \tag{2.10}$$

The power conversion efficiency is then defined as the maximum power point divided by the input power P_{in}:

$$\eta = \frac{\mathcal{FF} \cdot J_{SC} \cdot V_{OC}}{P_{in}}. \tag{2.11}$$

The other quantities can not be extracted from the IV curves as easily. To obtain

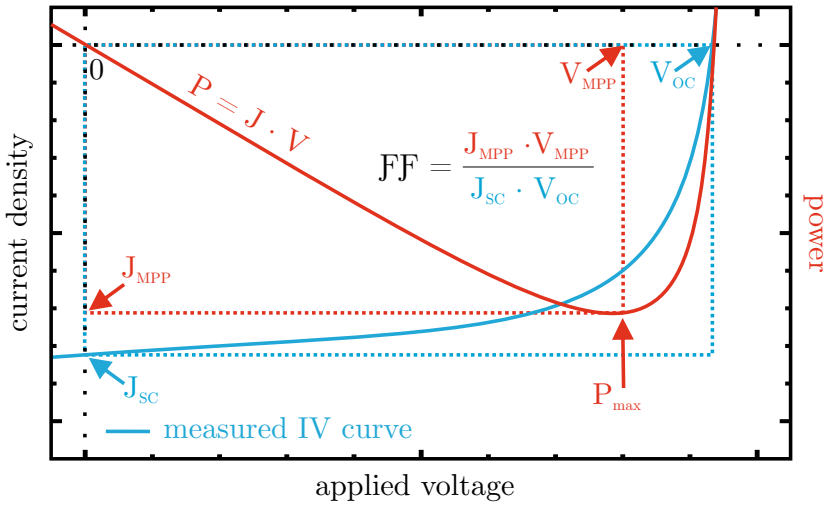

Figure 2.6.: ***Maximum power point*** *- Schematic to illustrate the maximum power point and its relation to open-circuit voltage and short-circuit current density.*

the values of R_{Sh}, R_S, A and J_0 one can fit the 1-diode equation 2.9 with programs like ECN's IVFit [53]. Performing IV measurements at different temperatures can yield more information about the solar cell. From equation 2.9 the temperature behaviour of the open-circuit voltage can be extracted, this denotes the voltage at which no current flows through the device. By setting $V = V_{OC}$ equation 2.9 can be written as [52]:

$$V_{OC} = \frac{A k_B T}{q_e} \cdot \ln\left(-\frac{V_{OC}}{R_{Sh} \cdot J_0} + \frac{J_{SC} \cdot \Gamma(V_{OC})}{J_0}\right). \tag{2.12}$$

For a typical cell the short-circuit current density has a value that is magnitudes higher than the factor $\frac{V_{OC}}{R_{Sh}}$, therefore the first term is neglected. Furthermore, the saturation current shows a temperature activated behaviour, which can be described by [52]:

$$J_0 = J_{00} \cdot e^{-\frac{E_{A,rec}}{Ak_BT}}, \tag{2.13}$$

J_{00} is only weakly temperature dependent, it is called the reference current density. Plugging equation 2.13 into 2.12 yields the final representation of V_{OC}:

$$V_{OC} = \frac{E_{A,rec}}{q_e} - \frac{Ak_BT}{q_e} \cdot \ln\left(\frac{J_{00}}{J_{SC} \cdot \Gamma}\right). \tag{2.14}$$

Assuming A as a temperature independent quantity, one is able to deduce the activation energy $E_{A,rec}$ of the main recombination pathway from the extrapolation of the open-circuit voltage's temperature dependence to 0 K. This quantity gives an insight to the origin of the recombination that limits the open-circuit voltage.
For recombination within the bulk this activation energy is equal to the bandgap, as measured from QE (see section 2.3.2). If the measured value is below E_g then the recombination is taking place close to the interface between absorber and buffer.
This is due to charge carriers not recombining directly between the two bands, but over interface defects. These defects are spread over a wide range of energies, and can trap holes from the valence band. Once trapped they recombine from there with electrons from the conduction band. The activation energy is reduced, since the defect is located in the bandgap and therefore the energetic distance to the conduction band is smaller than E_g. This has been illustrated in figure 2.7.
The graph also further illustrates the role, which the band-bending and space-charge

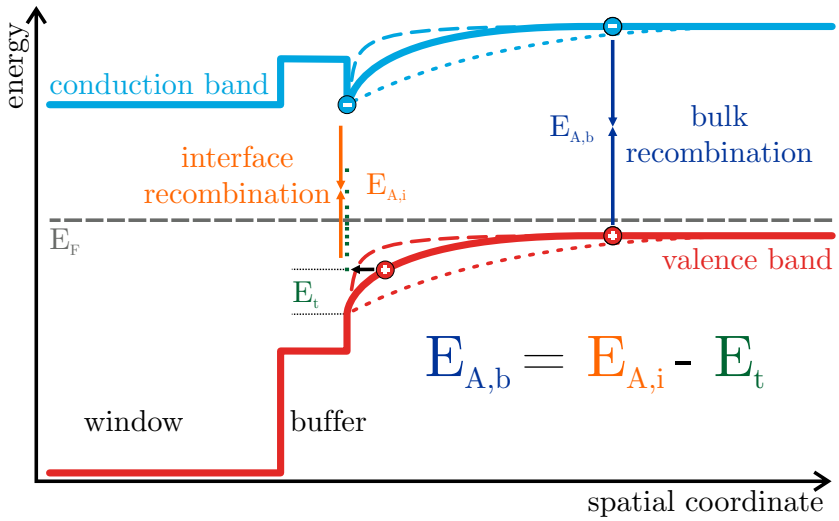

Figure 2.7.: *Dominant recombination pathway* - *If the dominant recombination lies within the bulk of the absorber, the voltage extrapolation to* 0 K *(see eq. 2.14) equals the bandgap. If however interface recombination is dominant, then $E_{A,rec}$ is smaller than E_g. This can be explained by holes getting traped into interface defects at E_t. Since these lie within the bandgap, the energetic distance to recombine is smaller than the bandgap energy. Different band-bending conditions have been indicated by the dashed and dotted lines. For steeper bands (dashed) the effect is enhanced, while it is surppressed for a flatter profile (dotted).*

region width play on the activation energy. As the tunnelling probability decreases exponentially with the distance that has to be overcome, steeper bands (indicated by the dashed line) enhance this effect, while a flatter band-bending in a long SCR (dotted line) suppresses it. Coupled with the temperature behaviour of the diode quality factor and saturation current density, one can get information about the dominant recombination pathway, this is described en detail in [52]. Due to the freeze out of charge carriers and mobility at low temperatures, there can be a strong increase in the series resistance. This is of importance to consider, when performing admittance measurements, as the equivalent circuit can forms a RC-resonator with a response frequency in the measurement range. To model this behaviour the values for series and shunt resistance should be recorded at low temperatures, this will be further elaborated on in section 2.3.3.

IV and IVT measurement setup

In the framework of this thesis two different setups were used to measure current-voltage curves, one for measurements at room temperature and one for the temperature dependence (IVT). Figure 2.8 depicts the utilized IVT measurement setup. Both, the IV and

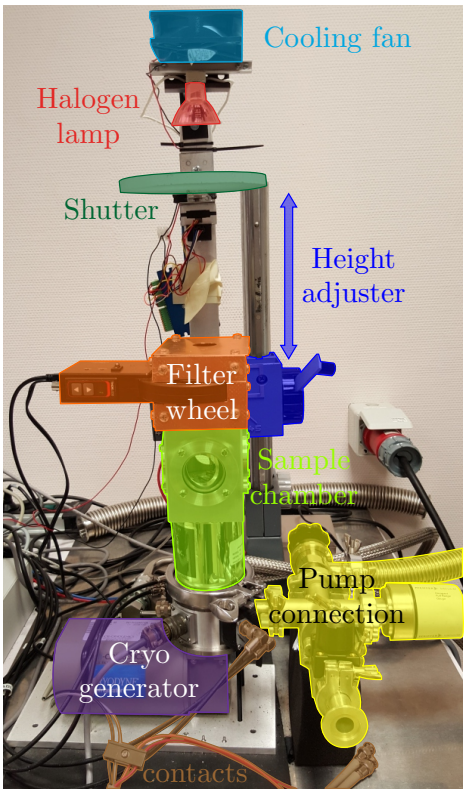

Figure 2.8.: ***The IVT/Admittance/CV setup.*** *- Photo of the utilized measurement setup. The samples are mounted in the sample chamber. For IVT illumination a halogen lamp is mounted above a shutter and cooled by a fan. The neutral density filters in the wheel and height adjustment can be used to tune the illumination intensity. The cryo-generator cooles the pumped sample chamber down to about* 60 K.

IVT setup are equipped with a Sourcemeter to supply the voltage and collect the current data. Illumination was done by a halogen lamp. To keep the temperature stable the lamp was running continuously, dark measurements were then performed by shading the samples. The desired light output power can be adjusted by changing the height of the lamp, a calibrated Si device is used as reference to achieve illumination conditions similar to AM 1.5 at 1000 $\frac{\mathrm{W}}{\mathrm{m}^2}$. In the IVT setup it is also possible to change the illumination intensity by adding a filter wheel that is equipped with different neutral density filters. For the temperature dependence the samples were mounted in a closed-cycle helium cryostat. For measuring the cell temperature a temperature diode was glued onto the sample holder on a 2 mm glass substrate, similar to the glass used for cell fabrication. The contacting of the samples in the IVT setup was done by fixing a copper wire on top of the front and back contacts with a conductive 2-component epoxy glue. Simple press contacts as used in the room temperature setup did indeed not stay in place during cooling. The sample is mounted in a closed-cycle helium cryostat, a cryo-generator allows to cool down the chamber. A temperature control allows for stable temperatures, by an electric heater underneath the sample temperatures in between 320 K and about 40 K can be reached .

2.3.2. Quantum efficiency

Quantum efficiency measurements (QE) are a quick way to asses the light absorption and transport characteristics of a thin-film solar cell. They can give insights into the optical and electrical losses that limit the short-circuit current density and basic absorber properties, namely the bandgap and effective collection length. QE measurements are performed by shining intensity modulated, monochromatic light on the device while measuring the resulting current for each wavelength. By comparing this current to that obtained from a calibrated diode, one is able to determine the ratio of generated charge carriers over incident photons. This is the external quantum efficiency or EQE. By application of a forward or reverse bias electrical losses can be enhanced or suppressed, making it possible to distinguish them from the optical ones.

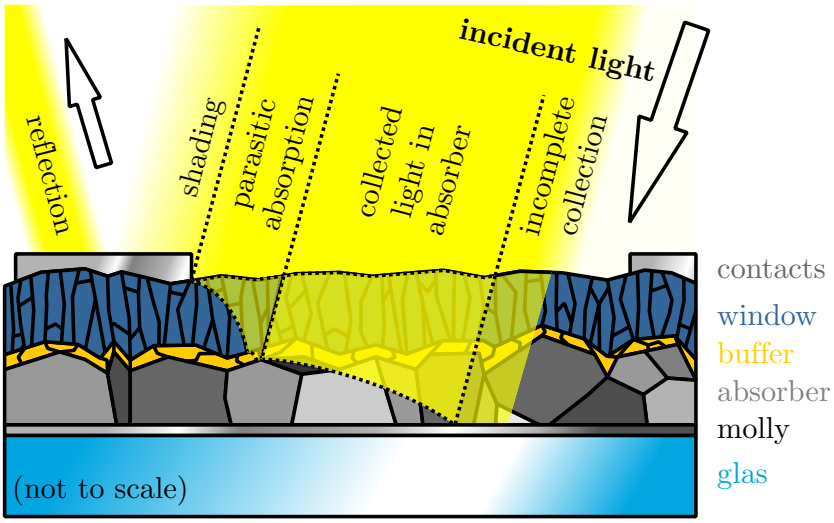

Figure 2.9.: ***Optical losses of a thin-film solar cell.*** *- Scematic drawing of the occuring losses in a solar cell. Not all the light can be collected within the absorber, part of it is reflected on the different interfaces, part is lost due to the shading of the opaque front contact, another part is absorbed within the window and buffer layer and in the case of too thin solar cells there is also the possibility that light passes through without being absorbed.*

The spectra are plotted as EQE (either in percent or as a fraction) over the wavelength. The characteristic shape can then be evaluated in regard of losses, furthermore QE measurements can be used to obtain the bandgap energy of the absorber material. To do this one can plot the EQE over photon energy and extrapolate the absorption edge on the low energy side of the spectrum to the intersection with the energy axis. By integration of the product of the obtained QE spectrum and the AM spectrum (or that of the lamp, utilized in the current-voltage measurements) over the measured wavelength range one can calculate J_{SC} [54]. Ideally this should be the same short-circuit current density as extracted from the current-voltage measurements. The "American Society for Testing and Materials" has established an array of standard spectra for differing air mass conditions (AM spectra), which have subsequently been adapted internationally [55]. They are an approximation to the solar spectrum which results from the absorption of light within the earth's atmosphere. The different numbers correspond to the thickness of a model atmosphere, through which the light has to travel, for example AM 0 corresponds to the solar spectrum in outer space. An air mass of 1.5 was chosen historically, as this value approximated the mean solar radiation received in most of the United States [55], it is also

the spectrum utilized in this work, since it has been established as a widely used standard.

Typical loss mechanisms [54], which can affect the QE yield are described in the following and illustrated in figure 2.9. All the losses occur at different parts of the solar cell structure, which is described in detail in section 3.2. The first loss is shading from the Al:Ni grid, it reduces the quantum efficiency uniformly over the whole spectral range. From the ratio of shaded to active area one can determine the transmittance $\mathcal{T}_\mathrm{g}$ past the grid. This shading only plays a role in current-voltage measurements, because in the QE setup that was used in the framework of this thesis the spot size of the incident light is smaller than the space between the lines of the front contact, thus there are no grid losses. In general it is dependent on the solar cell design itself and grid size has to be optimized to allow for maximum charge extraction while minimizing the covered area. The reflection $\mathcal{R}_\mathrm{f}$ from the interfaces between materials of different refractive indices is the next optical loss. Anti-reflective coatings are used in high efficiency devices to reduce these losses. Absorbance of the window $\mathcal{A}_\mathrm{w}$ and buffer $\mathcal{A}_\mathrm{b}$ further lowers the $\mathrm{J_{SC}}$, the onset of the bandgaps of ZnO and CdS are visible on the short wavelength side of the QE. At around 500 nm the absorption in the CdS begins. Due to the small thickness of this layer, part of the higher energy light can still pass and be converted to electron-hole pairs, the reduction is exponential with buffer thickness according to the Beer-Lambert law. This thickness should be as small as possible, without sacrificing junction quality. Below around 400 nm the QE rapidly drops to zero, because the light gets fully absorbed in the ZnO window. This layer also has a sizeable absorption in the near infrared region above 900 nm, due to free carriers. If the layer is not very thick or the absorption coefficient α of the layer is rather small, also incomplete absorption in the absorber layer can reduce the QE. Spectral absorbance and reflectance measurements can be used to obtain $\mathcal{A}_\mathrm{w}$, $\mathcal{A}_\mathrm{b}$, α and $\mathcal{R}_\mathrm{f}$ for the different materials. The last loss mechanism is due to the limited collection length of minority charge carriers. A short space-charge region width or low carrier lifetime within the absorber can lead to recombination of charge carriers before extraction. This electrical loss can be reduced in measurements by application of a reverse bias. Factoring in all the optical losses one is able to determine the internal quantum efficiency or IQE after formula 2.15:

$$\begin{aligned} EQE\left(\lambda, \mathrm{V}, \mathrm{J}\right) = \mathcal{T}_\mathrm{g} \cdot \left[1 - \mathcal{R}_\mathrm{f}\left(\lambda\right)\right]\left[1 - \mathcal{A}_\mathrm{w}\left(\lambda\right)\right]\left[1 - \mathcal{A}_\mathrm{b}\left(\lambda\right)\right] \\ \cdot IQE\left(\lambda, \mathrm{V}, \mathrm{J}\right) \cdot \Gamma\left(\lambda, \mathrm{V}, \mathrm{J}\right). \end{aligned} \tag{2.15}$$

The external collection efficiency (or gain-function) $\Gamma\left(\lambda, \mathrm{V}, \mathrm{J}\right)$ describes a factor that depends on the illumination and bias conditions during the measurement. Usually this factor can be set to unity, if the measurement isn't strongly biased either through an applied voltage or lighting [54]. If all these parameters are known for the whole spectral range one is able to calculate IQE and subsequently the effective collection length $\mathrm{L_{eff}}$ [56], which is an important measure of the transport properties of the absorber:

$$IQE\left(\lambda, \mathrm{V}\right) \cong 1 - \frac{\mathrm{e}^{\alpha(\lambda) \cdot \mathrm{x_{SCR}(V)}}}{\alpha\left(\lambda\right)\mathrm{L_{eff}} + 1}. \tag{2.16}$$

The space-charge region width $\mathrm{x_{SCR}}$ can be obtained from capacitance-voltage measurements. This approximation is only valid for absorbers thick enough to fully absorb the incident light, with complete collection within the space-charge region and if all carriers generated in the neutral bulk can diffuse to the depletion edge [54].

QE measurement setup

The setup is composed of two light sources a Xenon and a quartz halogen lamp, which provide different parts of the spectrum. They are shining through a monochrometer and the resulting monochromatic light is then modulated by chopper wheel and directed on the sample. The illuminated area is a spot of about 2 mm diameter. The sample itself is electrically connected by press-contacts at both the front and the back. The small signal of the light-induced current is amplified by a potentiostat and then measured by a lock-in amplifier, which is tuned to the modulation frequency of the chopper wheel. Also a DC bias can be applied to the solar cell. Two calibrated devices, an InGaAs and a Si diode, provide the current reference at each wavelength to convert the measured light-induced of the device into EQE.

2.3.3. Admittance spectroscopy

Admittance spectroscopy is a method to measure the response of a sample under application of a small AC bias as a function of test frequency ω and sample temperature T. In the case of semiconductor junctions this can be used to study defects in the structure, either on interfaces or in the bulk. A defect crossing the Fermi level can be filled with or depleted of charge carriers. Through its response behaviour with a change of temperature it becomes possible to measure its energetic distance to the band, while its frequency dependence gives insight into its capture/emission rates. The contribution of deep traps to the admittance is outlined in detail in chapter 9.4 of [57], the derivation shown there will be sketched in the following.

The physical quantity admittance Y (eq. 2.17), describes how current flows through a circuit under an oscillating voltage. It can be separated in an in-phase current component, the conductance $\mathrm{G}(\omega)$ and an out-of-phase part the susceptance $\mathrm{S}(\omega)$, which is related to the capacitance as $\mathrm{C}(\omega) = \frac{\mathrm{S}(\omega)}{\omega}$.

$$\mathrm{Y}(\omega) = \mathrm{G}(\omega) + i\mathrm{S}(\omega) \tag{2.17}$$

A small alternating voltage ($\mathrm{V_{AC}}$) is applied to the junction, which periodically steepens (in reverse bias) and then flattens (under forward bias) the bands.

This results in charge carriers moving into or away from the depletion region, effectively shortening or increasing it, the resulting current is given by eq. 2.18. In the case of a p-type absorber layer, like CIS, the charge carriers in question are holes, which can be trapped at shallow acceptors or deep defects:

$$\mathrm{J(t)} = \frac{\mathrm{d}}{\mathrm{dt}}\delta\mathrm{q_a(t)} + \frac{\mathrm{d}}{\mathrm{dt}}\delta\mathrm{q_t(t)}. \tag{2.18}$$

The different terms are due to the storing of charge carriers in the shallow acceptors $\delta\mathrm{q_a(t)}$ and deep trap states $\delta\mathrm{q_t(t)}$ or emission from them. The admittance can be derived by expressing J(t) in terms of the AC voltage $\mathrm{V_{AC}(t)} = \mathrm{V_0} \cdot \exp(i\omega\mathrm{t})$. At the edge of the space-charge region the holes on the shallow acceptors can react basically instantaneously to the modulation due to their high capture/emission rates. Therefore the change of the acceptor charge is given by:

$$\delta\mathrm{q_a(t)} = \mathrm{q_e N_a(x_{SCR})}\delta\mathrm{x_{SCR}(t)}. \tag{2.19}$$

This is not the case for the deep traps, whose response is highly dependent on their rates, generally their charge response can be written as:

$$\delta q_t(t) = q_e \int_0^{x_{SCR}} \delta N_p(x,t) dx. \tag{2.20}$$

The variable $\delta N_p(x,t)$ is the deviation of trapped holes from the steady state value at the point where the trap crosses the Fermi level. The density of free carriers can be written as:

$$N(x,t) = N_0(x,t) + \delta N(x,t), \tag{2.21}$$

with $N_0(x,t)$ being the equilibrium distribution of holes in the depletion region. Under the assumption of a small oscillating voltage at a depth x ($q_e V(x,t)/k_B T << 1$), the change in hole density $\delta n(x,t)$ is given by:

$$\delta N(x,t) = N_0(x) \cdot \frac{q_e V(x,t)}{k_B T}. \tag{2.22}$$

This is equal to an instantaneous response of the shallow acceptors to the local potential change. For the deep defects the same mechanism drives the trapped charges, however due to their hole capture c_h and emission coefficients e_h their response is delayed. The capture rate $\tilde{c}_h$ is equal to the product of the thermal velocity of the holes v_{th} and the capture cross section of the trap σ_t. Therefore if the defects can respond fast enough, the quasi-static distribution that describes the hole occupation of the traps is given by the rate equation:

$$\frac{\partial}{\partial t}\delta N_p(x,t) = \tilde{c}_h N(x,t) \cdot [N_t - N_p(x,t)] - e_h N_p(x,t). \tag{2.23}$$

One can easily see, while the capture term of the equation is limited by the number of free holes times the unoccupied trap states, the emission is only limited by the number of occupied traps. This is due to the higher density of states in the valence band compared to that of a defect, therefore a hole can always be emitted to the band, but for a capture process to occur, always both, a free hole and an unoccupied trap are needed. In steady state conditions the time derivative of the equation is zero and the capture and emission rate balance each other:

$$\tilde{c}_h N_0(x) \cdot [N_t - N_{p,\,0}(x)] = e_h N_{p,\,0}(x). \tag{2.24}$$

Now with the expression for the free carrier density (eq. 2.21) and the response frequency $f_0 = \tilde{c}_h N_0(x) + e_h = c_h(x) + e_h$ the local response of $\delta N_p(x,t)$ to an external modulation $\delta N(x,t)$ can be approximated as:

$$\frac{\partial}{\partial t}\delta N_p(x,t) = -f_0(x)\delta N_p(x,t) + \tilde{c}_h \cdot [N_t - N_{p,\,0}(x)]\delta N(x,t). \tag{2.25}$$

For high frequencies $f_0(x)$ the response is instantaneous and a quasi-static distribution can be derived, under the condition that $f_0(x)\delta N_p(x,t) >> \frac{\partial}{\partial t}\delta N_p(x,t)$:

$$\delta N_{p,\,0}(x,t) = \frac{\tilde{c}_h \delta N(x,t)}{\tilde{c}_h N_0(x) + e_h} \cdot [N_t - N_{p,\,0}(x)] \tag{2.26}$$

The next step is to derive the external modulation as a function of the applied voltage. Through Poisson's equation the charge distribution and external voltage are related by:

$$V(t) = \frac{1}{\epsilon_r \epsilon_0} \cdot [x_{SCR}\delta q_a(t) + \tilde{x}_t \delta q_t(t)]. \tag{2.27}$$

The band-bending at a depth x within the space-charge region depends on the outer applied voltage and the charge within the interval between x and the depletion edge. The contribution of the donors $\delta q_a(t)$ is spread out over δx at x_{SCR}, while the charge contribution of the traps is located at $\tilde{x}_t$. It follows:

$$V(x,t) = \frac{1}{\epsilon_r \epsilon_0}(x_{SCR} - x)\delta q_a(t) + V_t(x,t). \tag{2.28}$$

Now by assuming:

- The trap energy crosses the Fermi level at a fixed depth within the junction, that is to say $\tilde{x}_t(t)$ is constant in time
- Capture and emission rates are the same, therefore $f_0(x) = 2e_h = f_0$
- There is only a small potential drop due to $\delta N_p(x,t)$ at $\tilde{x}_t(t)$, $V_t(x,t)$ will thus be neglected.

With this, eq. 2.27 can be inserted into eq. 2.28, yielding the expression for $V(\tilde{x}_t, t)$:

$$V(\tilde{x}_t, t) = \frac{1}{\epsilon_r \epsilon_0} \frac{x_{SCR} - \tilde{x}_t}{x_{SCR}} \cdot [\epsilon_r \epsilon_0 V_{AC}(t) - \tilde{x}_t \delta q_t(t)]. \tag{2.29}$$

Through these assumptions $\delta N_p(x,t)$ becomes independent of x, all traps respond instantaneously with the same f_0, with the same free hole density $N(\tilde{x}_t(t), t)$ therefore the change in charge is given by $\delta q_t(t) = q_e N_t \delta x$ at low frequencies. Utilizing this, a differential expression for $\delta q_t(t)$ can be found after substituting eq. 2.28 into eq. 2.25, one receives:

$$\begin{aligned} \frac{\partial}{\partial t}\delta q_t(t) &= -f_{crit}\delta q_t(t) + g_t V_{AC}(t) \\ \text{with } f_{crit} = f_0 \left[1 + \frac{\tilde{x}_t}{x_{SCR}} \frac{N_t}{N_a}\right] &\text{ and } g_t = f_0 \frac{\epsilon_r \epsilon_0}{x_{SCR}} \frac{N_t}{N_a}. \end{aligned} \tag{2.30}$$

The solution to this differential equation is given by:

$$\delta q_t(t) = \frac{g_t}{f_{crit} + i\omega} V_0 e^{i\omega t}. \tag{2.31}$$

Now all the parts are in place to derive the complex admittance as $J(t)/V_{AC}(t)$. For this, equation 2.18 is divided by eq. 2.27 and eq. 2.31 can be substituted in, to yield:

$$\begin{aligned} Y(\omega) = &\left(1 - \frac{\tilde{x}_t}{x_{SCR}}\right) \frac{\omega^2 g_t}{{f_{crit}}^2 + \omega^2} \\ &+ i\omega \left[\frac{\epsilon_r \epsilon_0}{x_{SCR}} + \left(1 - \frac{\tilde{x}_t}{x_{SCR}}\right) \frac{f_{crit} \cdot g_t}{{f_{crit}}^2 + \omega^2}\right]. \end{aligned} \tag{2.32}$$

The resulting capacitance is the imaginary part of the admittance:

$$C(\omega) = \frac{\epsilon_r \epsilon_0}{x_{SCR}} + \left(1 - \frac{\tilde{x}_t}{x_{SCR}}\right) \frac{f_{crit} \cdot g_t}{{f_{crit}}^2 + \omega^2}, \tag{2.33}$$

it is easily visible that for high measurement frequencies, the capacitance drops down to $C_{scr} = \epsilon_r \epsilon_0 / x_{SCR}$, while for decreasing frequencies there is a step to higher capacitance values by ΔC, with

$$\Delta C = \frac{g_t}{f_{crit}} + \left(1 - \frac{\tilde{x}_t}{x_{SCR}}\right). \tag{2.34}$$

The critical frequency f_{crit} between the high and low capacitance values denotes the response frequency of the measured defect. Within the measured admittance spectra f_{crit} is marked by the inflection point of the capacitance drop at a given temperature. With this it is possible to derive the defects' activation energy E_A, if the defects' temperature dependence is taken into account. In the quasi-static case the defect emits and captures holes at an equal rate, therefore $2 \cdot f_{crit}$ can be written as the sum of c_h and e_h. Utilizing eq. 2.24 and the Fermi-Dirac distribution, which gives the densities of charge carriers in the band and at the trap, the frequency dependence on the position of the defect in the forbidden gap can be written as:

$$f_{crit} = \nu_0 \cdot \exp\left(-\frac{E_A}{k_B T}\right). \tag{2.35}$$

The variable ν_0 denotes the attempt-to-escape frequency, which is the product of the holes' v_{th}, the defects' capture crosssection σ_p and the effective density of states in the valence band N_V. The quantities v_{th} and N_V are both temperature dependent, therefore often the thermal pre-factor ξ_0 is introduced. With the proportionalities $v_{th} \propto T^{1/2}$ and $N_V \propto T^{3/2}$ the attempt-to-escape frequency can be written as $\nu_0 = \xi_0 \cdot T^2$ and the final temperature dependence of the defect is:

$$\ln\left(\frac{f_{crit}}{T^2}\right) = \ln(\xi_0) - \frac{E_A}{k_B} \cdot \frac{1}{T}. \tag{2.36}$$

This is an activated behaviour, which is described by an Arrhenius law:

$$\ln(r) = \ln(r_0) + \frac{E_A}{k_B T}. \tag{2.37}$$

Therefore a plot of $\ln\left(\frac{f_{crit}}{T^2}\right)$ over $\frac{1}{T}$ yields the defects activation energy.

Modelling the density of states

Evaluation with the Arrhenius plot is a quick way of deducing the activation energy of a capacitance response in admittance measurements, but this is a simplified picture. A real defect is not characterized by a discrete energy level alone, but rather by a distribution of energies, this is illustrated in figure 2.10 with a distribution containing three signals. A deep trap can be approximated by a Gaussian profile, while the Arrhenius plot just returns the energy of it's maximum, the defect density of states(DOS) is intersected at different positions throughout the SCR. Walter *et al.* [58] derived a method of reconstructing the DOS for a given defect distribution from admittance measurements.
Equation 2.35 calculates the frequency, up to which a defect of a given energy depth can respond to the AC signal. However, by rearranging one can switch to a representation of the threshold in energy, up to which traps are able respond to a certain frequency. A change of the parameters for the activation energy $E_A \rightarrow E_\omega$, and $f_{crit} \rightarrow \omega$ accounts for the function of energy now being dependent on the frequency. Furthermore to include the weak T^2 temperature dependence of deep traps the attempt-to-escape frequency ν_0 is again replaced with the thermal pre-factor ξ_0. From this one receives:

$$E_\omega = k_B T \cdot \ln\left(\frac{2 \cdot \xi_0 \cdot T^2}{\omega}\right). \tag{2.38}$$

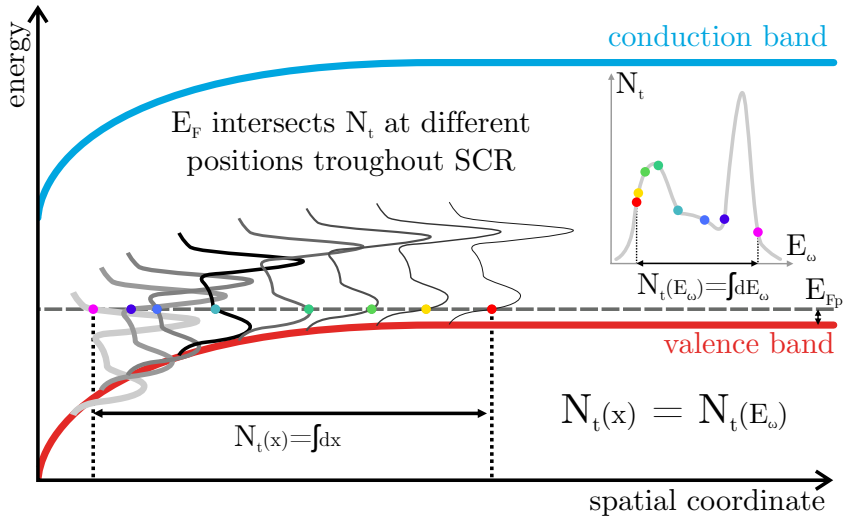

Figure 2.10.: ***Distribution of defects within the bandgap.*** *- Schematic drawing of a defect distribution in the absorber layer. It is assumed, that the defect distribution is spatially homogenous, as indicated by the repetetion of the same defect shape at various positions throughout the junction. If this is the case, the distribution $N_t(E_\omega)$ can be reproduced as a function $N_t(x)$ of the probing depth within the SCR. The same defect density is drawn in the inlay (albeit mirrored) to illustrate this relation.*

This is the energy axis of the Walter analysis. As illustrated in figure 2.10, the DOS as a function in space can be substituted by a DOS in dependence of E_ω. Since the capacitance contribution is proportional to the integration over all defects that cross the majority Fermi level E_{Fp} in the space-charge region, it can also be expressed as an integral over the DOS energy. From taking the derivative on both sides of the expression, the DOS can be calculated as a function of the Walter energy axis E_ω and the derivative of the capacitance $\frac{dC}{d\omega}$ [58]:

$$N_t(E_\omega) = -\frac{2(V_{bi} - V_{app})^{3/2}}{x_{SCR}\sqrt{q_e}\sqrt{E_\omega - E_{Fp}}} \cdot \frac{\omega}{k_B T} \cdot \frac{dC}{d\omega} \tag{2.39}$$

From this it becomes apparent, that the measurement can probe $N_t(E_\omega)$ via the differential change of the capacitance with frequency $\frac{dC}{d\omega}$ at a given temperature. V_{app} denotes an externally applied bias voltage, under standard measurement conditions it is zero. Since the Fermi level probes the same defect density within a range of temperatures, one is able to reconstruct the DOS by overlaying the calculated densities in this temperature range. Except for the bulk quasi-Fermi level E_{Fp} and the thermal pre-factor all necessary parameters are known or can be measured with supplementary techniques. Namely CV measurements, which will be described later in section 2.3.6 deliver the space-charge region and built-in voltage. The bulk quasi-Fermi level denotes the lower boundary, of the probing range, which is accessible to the measurement. This becomes directly clear from figure 2.10, as no crossing can occur below this value. Since it is the boundary condition, an educated guess is sufficient to approximate a value, where the fitting should be cut off. Lastly a starting value for the thermal pre-factor can be taken from the Arrhenius-plot. However, one still has to take care and compare multiple temperature curves. In the temperature range, where the defect step appears in the admittance spectra, the measurement probes the same DOS. Therefore all curves should line up and form the

same shape, however if the value of the thermal pre-factor was not chosen correctly (or differs from the value from Arrhenius), one has to adjust this value (and by this the energy axis E_ω) until they do line up. This is then the correct thermal pre-factor for this certain distribution. If more than one defect responses are visible within the spectrum, a different thermal pre-factor has to be chosen for each temperature interval, separately. This means, since distinct defects are characterized by different thermal pre-factor, one can not find a continuous energy axis for the whole measurement. To extract the defect parameters, namely the peak energy position E_A, defect density as area under the curve N_t and full-width-at-half-maximum w_{FWHM}, the data can than be fitted with a Gaussian curve. In the utilized representation the Gaussian can be written as:

$$N_t(E_\omega, \xi_0) = \frac{N_t e^{-\frac{4\ln(2)(E_\omega - E_A)^2}{w_{FWHM}{}^2}}}{w_{FWHM}\sqrt{\frac{\pi}{4\ln(2)}}}. \tag{2.40}$$

Note the difference between $N_t(E_\omega, \xi_0)$ as the function describing the Gaussian DOS of a certain defect density at a fixed thermal pre-factor and N_t as a scalar quantity, the measure of total integrated defect density of that defect.

Admittance setup

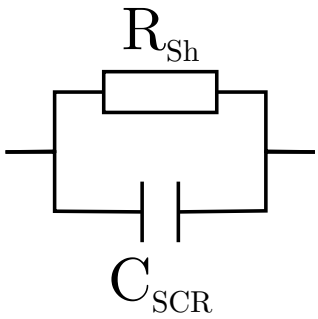

Figure 2.11.: ***Equivalent circuit model*** *- Simple model for for C_p-G measurement mode consisting of the capacitance of the pn-junction in parrallel to a shunt conductance.*

The measurement setup for admittance measurements is described in section 2.3.1. The only difference is, that instead of a Sourcemeter, an LCR-Meter is used to measure admittance curves. Capacitance is measured in parallel to a conductance (Cp-G mode, $G=R_{Sh}{}^{-1}$), the equivalent circuit is pictured in figure 2.11. Measurements were performed in the dark, in the temperature range of 320 K down to 40 K in 10 K-steps, as measured by the sensor in the cryostat. Sample temperatures deviated therefore slightly and where measured by a second diode close to the cell. The small AC test bias voltage was 30 mV and frequencies were varied in between 100 Hz and 10^6 Hz.

2.3.4. Non-defect related capacitance responses

The previous section showed the theoretical background of thermal admittance spectroscopy as a tool for the characterization of deep traps in a one-sided pn-junction. However there are other effects and device characteristics that can produce a similar step in the capacitance spectrum. Different kinds of such phenomena and potential methods to discriminate between them will be discussed in the following.

Interface defects

The growth of two different materials on top of each other is almost never perfect and a number of different causes can lead to electrically active defects in this region. Lattice mismatch, differences in bond strength, vacancies due to chemical etching before growth, inter-diffusion to name a few, can all lead to a continuum of states throughout the bandgap. Defects that are localized spatially at the interface but distributed continuously in energy, will intersect with the Fermi level close to the heterointerface, for all temperature and bias conditions.
Therefore they can always contribute to the capacitance and produce a step, dependent on their critical frequency similar to a deep trap [59]. The measured activation energy is then dependant on the position of the Fermi level in the bandgap, contrarily to a deep trap, whose position in the band is fixed. Therefore a shift in the Fermi level will only affect the measured energy of the interface defect, but not of the deep defect. Applying a reverse DC bias (or illumination) can be used to decrease the Fermi level E_F by an amount equal to applied bias times the elemental charge qV_{app}.
To discriminate interface and deep defects, TAS can be conducted under different external bias conditions. A step with a shifting activation energy can then be attributed to interface states [59]. However the reverse conclusion is not true, if the Fermi level is pinned at the interface, it will be stable regardless of applied bias. Therefore, one can not always directly make a distinction between interface and bulk states from admittance measurements. In some cases, a change in the sample structure, which only affects the heterointerface can help. For example air annealing has been employed to change the defect density at the interface, which could be used to identify an interface state, which did not shift with bias [60].

Carrier freeze-out

If the temperature of a semiconductor is decreased, there is also less thermal energy available for the charge carriers to be re-emitted into the bands. Therefore the number of free carriers in the band gets smaller with decreasing temperature [61]. This will also result in a capacitance step and will usually be the last step in the admittance spectrum. The exception being, if transport is still possible through variable range hopping, in that case the carrier freeze out step will be followed by a mobility freeze-out, which will be discussed in the following. Otherwise its high frequency value is the geometrical capacitance C_{geo}, without free carriers the absorber will act as a dielectric similar to a plate capacitor:

$$C_{geo} = \frac{\epsilon_r \epsilon_0}{d_{abs}}. \tag{2.41}$$

Due the lower free-carrier concentration in the bands, conductivity of the absorber layer will be decreased. Therefore a carrier-freeze-out will result in a rapidly growing series resistance.

Mobility freeze-out

The standard evaluation of TAS measurements, as described in chapter 2.3.3 assumes that the capture and emission process of holes is not limited by transport. However at lower temperatures, charge carriers might not have enough thermal energy to occupy the bands, but still be mobile. In disordered semiconductors, charge carriers can move through tail states by thermally activated hopping transitions [62], which is characterized by a decrease of carrier mobility. This has been shown to occur in CIGS by Schmitt *et al.* [63], who found the conductivity pathway shift to variable range hopping at temperatures below 200 K.
This change of the conduction process, the mobility freeze-out, can result in a capacitance step [64]. In that case, the critical frequency is no longer governed only by the hole emission rate, but rather the sum of the time constants of the capture/emission process τ_h, diffusion τ_{di} and drift τ_{dr} of holes, both of which depend on μ_p. Cycling of the small AC measurement voltage results in a drift current of holes moving away from the junction during reverse voltage and diffusing back under forward bias. The first one is governed by the mean electric field $\mathcal{E}$ and the drift length L_{dr}, following the relation $\tau_{dr} \approx \frac{L_{dr}}{\mu_p \mathcal{E}}$. The second one is usually derived from the Einstein relation for the diffusion constant $D = \frac{\mu_p k_B T}{q_e}$.
With the diffusion length L_{di} it can then be written as: $\tau_{di} \approx \frac{q_e {L_{di}}^2}{\mu_p k_B T}$, However as shown in the cited work [62], this is not valid at decreased temperatures, where the relation between D and μ_p becomes temperature independent. In that case the carriers can follow the measurement signal only up to a critical frequency $f_{crit} = \frac{2\pi}{\tau_{di}+\tau_{dr}}$, again producing a drop in the capacitance spectrum. However the temperature behaviour of this step is not the same as that of a deep defect, resulting in a curved Arrhenius, when performing the standard evaluation for TAS. This curving has been found in CIGS and was explained by thermally assisted tunnelling [65].
To remove this curvature, the right temperature dependence has to be derived from the diffusion constant, which is equal to ${x_H}^2 \cdot \mathcal{P}_H$ [66], with the parameters x_H for the range and $\mathcal{P}_H$ the corresponding probability of a hopping event. From Mott's law [67], one can derive the temperature proportionality for both variables, yielding $x_H \propto T^{-1/4}$ and $\mathcal{P}_H \propto \exp\left(T^{-1/4}\right)$. Therefore the Arrhenius evaluation can be replaced by plotting $\ln\left(f_{crit} T^{1/2}\right)$ over $T^{-1/4}$, which then should yield a straight line. If a mobility freeze-out occurs, in the sense that hopping conduction remains as a transport channel, it will form the lowest temperature step in the capacitance, below the carrier freeze-out response. In that case it will go down towards C_{geo}.

Thermally activated series resistance

Since the sheet resistance of semiconductor layer is anti proportional to both the free carrier concentration and their respective mobilities [50], it is directly apparent that both, mobility and carrier freeze-out directly result in an increase of the series resistance of the solar cell at low temperatures. In this case the describing the device via an equivalent circuit of just a capacitor in parallel to a shunt resistor is not valid anymore. The new situation can be described by including a second resistor which is connected in serial to both the capacitor and shunt resistor [68]. However this new circuit has to be included into the evaluation, since the measurement setup still utilizes the C_p-G mode.
If the values of serial R_S and shunt R_{Sh} resistance are known, the capacitance response of

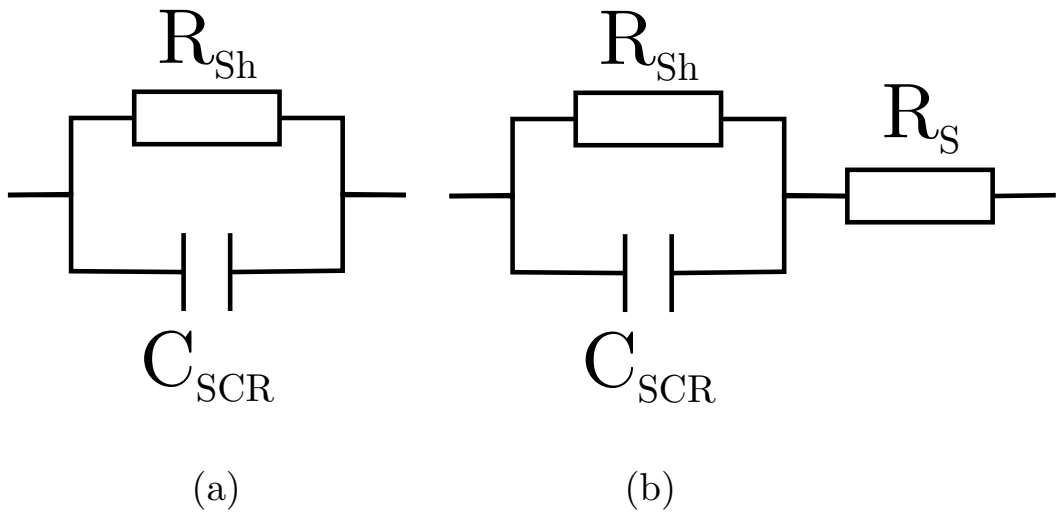

Figure 2.12.: ***Equivalent circuits for admittance measurements*** *- a) shows an equivalent circuit as utilized for evaluation of the measured admittance in C_p-G mode, b) shows the circuit with an added resistance in series to the junction.*

the equivalent circuit can be calculated from the measured value C_m using [68]:

$$C_m(f) = \frac{C}{\left(1 + \frac{R_S}{R_{Sh}}\right)^2 + (2\pi f)^2 (R_S C)^2}. \tag{2.42}$$

Usually a solar cell device is characterized by a very small series resistance and a reasonably high shunt, in that case it is directly visible that $C_m = C$ for low measurement frequencies. Only at high frequencies the second term in the denominator becomes significant and C_m is reduced by a factor of $((2\pi f)^2(R_S C)^2)^{-1}$. An estimate for a critical frequency can be made for a model solar cell with a high series resistance and capacitance. Values of series resistance = 1Ω and C = 100 nF, which are higher than the values of all presented samples, still deliver a time constant of $10^{-7} s$ surpassing the measurement range of 1 MHz by an order of magnitude. However if the series resistance is thermally activated, e.g. as in the case of a freeze-out, $\frac{R_S}{R_{Sh}}$ also becomes significant. In that case C is reduced at low frequencies due to the first term of the denominator, but also the critical frequency shifts into the measurement range, resulting in a step towards high frequencies. IVT measurements can be employed in order to measure the temperature behaviour of series and shunt resistance. From the calculation of the capacitance response as a function of the resistances one can then deduce the cut-off frequency, where the measurement is dominated by the series resistance [69].

Barrier at the back-contact

Contacting a semiconductor and a metal does not always yield an ohmic contact. Depending on the work functions of both materials, a potential barrier can form at the interface, this Schottky contact [70] results in a second SCR forming additionally to the pn-junction.

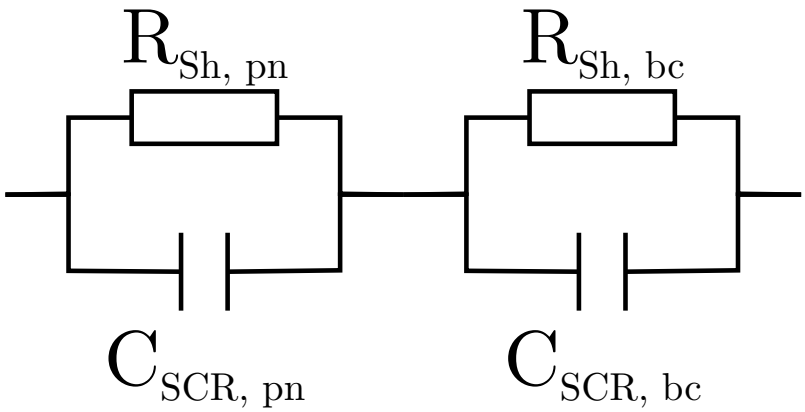

Figure 2.13.: ***Equivalent circuits for a pn-junction with a back contact barrier*** *- A Schottky barrier at the back contact (bc) leads to the formation of a second space-charge region in series with pn-junction (pn). Both can be characterized by a capacitor and parallel resistance.*

This second junction is oriented opposite to the primary pn-junction and blocks the DC current. In AC conditions this can be modelled by an equivalent circuit as illustrated in figure 2.13 [71]. Additionally to the RC element of the primary junction (labelled pn in the illustration) a second RC element is added in series with the first (labelled bc). The total capacitance of the resulting circuit can be written as [72]:

$$C = \frac{\frac{C_{scr,bc}}{{R_{Sh,pn}}^2} + \frac{C_{scr,pn}}{{R_{Sh,bc}}^2} + \omega^2 C_{scr,bc} C_{scr,pn} \left(C_{scr,bc} + C_{scr,pn}\right)}{\left(\frac{1}{R_{Sh,bc}} + \frac{1}{R_{Sh,pn}}\right) + \omega^2 \left(C_{scr,bc} + C_{scr,pn}\right)}. \tag{2.43}$$

Two different cases can be distinguished, the high and low frequency capacitance response:

$$C_{hf} = \frac{C_{scr,bc} C_{scr,pn}}{C_{scr,bc} + C_{scr,pn}} \tag{2.44}$$

If the AC frequency is high, the whole circuit acts as a serial connection of the two capacitors, while at low AC frequency it is not limited by the back contact and only the primary junction responds:

$$C_{lf} = C_{scr,pn}. \tag{2.45}$$

As with defects, the transition between low and high frequency values is marked by a critical frequency f_{crit}. From the temperature dependence of this, an activation energy can be extracted corresponds to the barrier height of the Schottky contact.

2.3.5. The Meyer-Neldel rule

The huge spread in activation energy and thermal pre-factor, that is usually observed in electrical defect measurements is often explained by the Meyer-Neldel (MN) law [73]:

$$\ln(\mathrm{r_0}) = \ln(\mathrm{r_{00}}) + \frac{\mathrm{E_A}}{\mathrm{k_B T_{iso}}}. \tag{2.46}$$

This behaviour can be found in activated processes that are related to each other by an isokinetic temperature $\mathrm{T_{iso}}$ and a constant $\mathrm{r_{00}}$. These processes all exhibit a characteristic value of $\mathrm{r_0}$ at $\mathrm{T} = \mathrm{T_{iso}}$. One explanation that is commonly found relies on the so-called multi-excitation entropy (MEE). The argument [74] [75] for this will be discussed in the following, starting out by considering the actual quantity which is measured in thermally activated measurements versus the quantity that is supposed to be measured. The energetic distance of the level to its corresponding band is what is seen as the activation energy $\mathrm{E_A}$. Thermodynamically this is an inner energy $\mathcal{U}$, it is the quantity that is supposed to be determined. But the energy value that is actually measured macroscopically is not the inner energy, but the Gibbs free energy $\mathcal{G}$ [76]:

$$\mathcal{G} = \mathcal{U} + \mathrm{p}\mathcal{V} - \mathrm{T}\mathcal{S}. \tag{2.47}$$

If the measurement is performed with no change in pressure p, volume $\mathcal{V}$ or entropy, only then the inner energy is equal to the Gibbs free energy. But this is usually not the case. In the common explanation [74, 75] of the MN behaviour in electrical defect measurements it is assumed that $\mathrm{p}\mathcal{V} = 0$, meaning there is neither a pressure nor a volume change involved, which doesn't have to be the case. Following through with this assumption the quantity that is measured will be set to $\mathcal{G} = \mathrm{E_A} - \mathrm{T}\mathcal{S}$. As for the entropy term: the way how admittance measurements work has been described in the previous section (2.3.3), for a trap to be able to respond to the AC measurement signal it has to be periodically emptied of charge carriers. For example a trap which interacts with the valence band has to be emptied of its hole. As stated previously, this is an activated process that follows the Arrhenius behaviour, see eq. 2.36. The hole has to overcome the associated energy barrier $\mathrm{E_A}$ by thermal excitation. In the case of deep defects the phonon energy $\mathrm{E_{ph}}$ is usually much smaller than this barrier. Therefore the number of excitations $\mathcal{N}_{\mathrm{x,n}} = \frac{\mathrm{E_A}}{\hbar\omega_{\mathrm{ph}}}$ can be large. This leads to an increase of possible ways how this energy can be supplied and therefore a number of microscopic states $\mathcal{W}$, which the system can pass through along the way. And this is the reason entropy now enters into the equation, as it is defined by the logarithm of this number of states: $\mathcal{S} = \mathrm{k_B} \cdot \ln(\mathcal{W})$. We can express $\mathcal{W}$ in terms of the number of necessary excitations $\mathcal{N}_{\mathrm{x,n}}$ out of all the possible excitations within the interaction volume $\mathcal{N}_{\mathrm{x,i}}$. With the Stirling approximation and the assumption that there are a lot more available excitations within the interaction volume than necessary, the equation simplifies to 2.48:

$$\mathcal{S} = \mathrm{k_B} \cdot \ln\left(\frac{\mathcal{N}_{\mathrm{x,i}}!}{\mathcal{N}_{\mathrm{x,n}}!(\mathcal{N}_{\mathrm{x,i}} - \mathcal{N}_{\mathrm{x,n}})!}\right) \overset{\text{Stirling}}{\Longrightarrow} \mathrm{k_B} \cdot \mathcal{N}_{\mathrm{x,n}} \cdot \ln\left(\frac{\mathcal{N}_{\mathrm{x,i}}}{\mathcal{N}_{\mathrm{x,n}}}\right) \overset{\mathcal{N}_{\mathrm{x,i}} \gg \mathcal{N}_{\mathrm{x,n}}}{\Longrightarrow} \frac{\mathrm{k_B E_A}}{\hbar\omega_{\mathrm{ph}}} \cdot \ln(\mathcal{N}_{\mathrm{x,i}}). \tag{2.48}$$

In chemistry there is a well-known Arrhenius-like equation, which instead of the inner energy uses the Gibbs free energy, this is the Eyring [77] equation:

$$\mathrm{r} = \frac{\mathrm{k_B T}}{h} \cdot \exp\left(-\frac{\mathcal{G}}{\mathrm{k_B T}}\right) = \frac{\mathrm{k_B T}}{h} \cdot \exp\left(-\frac{\mathcal{S}}{\mathrm{k_B}}\right) \cdot \exp\left(-\frac{\mathrm{E_A}}{\mathrm{k_B T}}\right). \tag{2.49}$$

This equation describes the rate r of a chemical reaction, which has to pass through a transition state, described by an energy barrier that the reactants have to overcome. Utilizing formula 2.48 for the multi-excitation entropy in 2.47 the Eyring equation reads:

$$r = \frac{k_B T}{h} \cdot \exp\left(\frac{E_A}{\hbar\omega_{ph}} \cdot \ln(\mathcal{N}_{x,i})\right) \cdot \exp\left(-\frac{E_A}{k_B T}\right). \tag{2.50}$$

From this equation it is apparent that if the condition $\frac{E_A}{\hbar\omega_{ph}} \cdot \ln(\mathcal{N}_{x,i}) = \frac{E_A}{k_B T}$ is fulfilled, then the reaction rate becomes a constant. In the context of traps within a semiconductor this means that there is a temperature, at which all traps would capture and emit carriers at the same rate, independent of their position within the band gap. This can be identified as the isokinetic temperature T_{iso} as already used in the MN law. Therefore by substituting $\frac{\ln(\mathcal{N}_{x,i})}{\hbar\omega_{ph}}$ for $(k_B T_{iso})^{-1}$, we find that the capture/emission process is governed by the MN behaviour, following the equation:

$$\ln(r) = \ln\left(\frac{k_B T}{h} \cdot \exp\left(-\frac{E_A}{k_B T}\right)\right) + \frac{E_A}{k_B T_{iso}}. \tag{2.51}$$

From this it becomes apparent, that by introducing entropy from multiple excitations that are necessary to overcome the energy barrier, a behaviour which can be described by a MN-type equation arises. It can be followed that entropy has to be taken into account, when evaluating electrical measurements that are dependent on thermal activation processes. By looking at the definition of T_{iso} and the entropy (eq. 2.48) an expression which links the entropy to the isokinetic temperature can be found [78]:

$$T_{iso} = \frac{\hbar\omega_{ph}}{\ln(\mathcal{N}_{x,i})} \cdot k_B = \frac{E_A}{\mathcal{S}}. \tag{2.52}$$

It becomes apparent, that this term governs the slope of eq. 2.51, therefore in an entropy free measurement the rate is no longer dependant on the activation energy. This implies for the application of the MN graphs that are shown in this work, that it is possible to give one thermal prefactor ξ_{00} for defects on the same MN-line, by simply taking the y-intersect of the linear fit. On the other hand this also implies, that while the electrical measurements show a MN-behaviour which can be relatively simply explained by multi-excitation entropy, this only affects the thermal prefactor of a given measurement. This is not an explanation for the huge spread in the measured activation energy of a single defect. It is possible however, that the explanation for this can be found in the pressure and volume. As previously stated the term $p\mathcal{V}$ is usually set to zero. But this is not necessary the case, the possibility of grid relaxations during the activation process could mean a difference in pressure and volume of a given defect distribution, this is particularly the case for deep defects. Which in turn could affect the effective barrier heights and therefore the number of needed excitations resulting in multi-excitation entropy and the observed behaviour. It is questionable however if these could account for the differences in the range of ≈ 100 meV. Unfortunately in the framework of this thesis it is not possible to measure or calculate the energy of grid relaxation processes, therefore no conclusive answer on the origin of the activation energy-spread can be given nor found in the literature.

2.3.6. Capacitance-voltage measurements

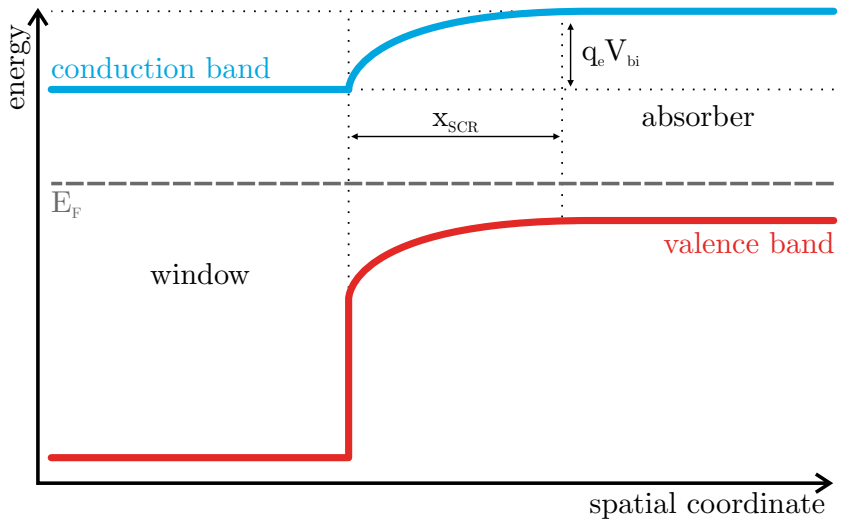

Figure 2.14.: ***Schematic of a one-sided np-junction.*** *- Under the assumption that the doping of the window layer is orders of magnitude higher than in the absorber, all the band-bending takes place on the p-side. (Simplified representation, without buffer layer.)*

With capacitance-voltage (CV) measurements it is possible to measure the free carrier concentration N_{CV} and built-in voltage V_{bi} of solar cells. From these other important properties, like the space-charge region capacitance C_{scr} and x_{SCR}, can be calculated. The capacitance density of a one-sided pn-junction under an external bias V_{app} can be written as [57]:

$$C = \sqrt{\frac{\epsilon_r \epsilon_0 q_e N_{CV}}{2(V_{bi} - V_{app} - \frac{k_B T}{q_e})}}. \tag{2.53}$$

The thermal term $\frac{k_B T}{q_e}$ can be neglected, as it is usually way smaller than the built-in voltage, which is defined as the sum of all band-bendings within the junction (depicted in figure 2.14). At zero applied bias this formula then results in the space-charge region capacitance:

$$C_{scr} = \sqrt{\frac{\epsilon_r \epsilon_0 q_e N_{CV}}{2V_{bi}}} \tag{2.54}$$

One can rewrite 2.53 as a function of C^{-2} to get a linear function of the applied voltage:

$$C^{-2} = \frac{2(V_{bi} - V_{app})}{\epsilon_r \epsilon_0 q_e N_{CV}}. \tag{2.55}$$

From this it becomes easily apparent that a plot of the inverse of the measured capacitance squared over the applied voltage yields a straight line with the slope proportional to N_{CV}^{-1} and intersect with the abscissa at V_{bi}. Under the right measurement conditions the value of N_{CV} can be equal to the shallow acceptor density N_a of the p-type absorber. But if there are deep traps within the absorber layer, one has to take care to exclude their effect on the measurement.
As previously covered (see sec. 2.3.3), deep defects can contribute to the capacitance, if they cross the Fermi level within the space-charge region and if the measurement frequency does not exceed their capture/emission rate (see eq. 2.35). If those two criteria are met,

the measured free carrier density is not the doping, but either at low frequencies the sum of the shallow and deep defects' densities $N_a + N_t$ or at higher frequencies a value higher then the doping, but lower then the sum [79]. The threshold in between high and low frequency is marked by the emission rate of the trap.
As shown in figure 2.15, this not only yields a wrong measurement of the doping, but also

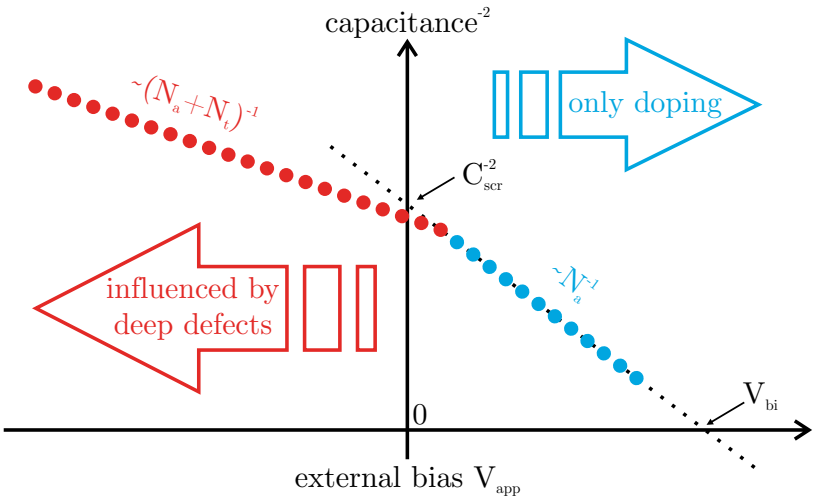

Figure 2.15.: ***Influence of deep defects on CV measurements*** *- Schematic depiction of a typical Mott-Schottky-plot. In reverse and small forward biases (visualized by red measurement points) the deep defects can be charged and contribute to the capacitance. Therefore the resulting carrier density N_{CV} as extracted from the slope is proportional to $N_t + N_a$. Under a sufficient forward bias (blue measurement points) they do not intersect the Fermi level and the measured density from the slope is equal to the number of shallow acceptors, therefore the doping density.*

leads to an non-physically high value of the built-in voltage. Now there is a possibility to alleviate the influence of deep defects on the measurement, it is possible to negate the trap influence through the right biasing conditions, as is depicted in figure 2.16.
Under reverse and no bias, there is a strong band-bending and the defect level always crosses the Fermi level within the space-charge region, the slope of the Mott-Schottky-plot is anti proportional to $N_{CV} = N_a + N_t$ and the intersect with the abscissa is higher than the true built-in voltage. By application of a forward bias the bands are flattened until the point where the defect is not crossed by the majority Fermi level E_{Fp} anymore. We can measure the true doping density and built-in voltage. In the evaluation this manifests as two linear behaviours that are visible within the Mott-Schottky-plot. First in reverse bias a rather low slope, associated with a high effective doping density, extrapolation yields a large voltage intercept. Going to zero and forward bias, there is a kink in the data towards a higher slope. Depending on both the position of the majority Fermi level and defect within the bandgap this can require a larger or smaller external bias, therefore the kink can occur at any bias position, not just for $V_{app} = 0$, even multiple kinks can be observed if different defect are crossed within the range of bias variation. Fitting the higher slope gives the correct doping and built-in voltage. In even further forward biases the curve deviates from a linear plot again. This is due to the conductivity of the sample, at sufficiently large biases the current will increase and overload the LCR meter. This is characterized by a sharp drop of the measured phase angle θ_m. Values of θ_m are deemed

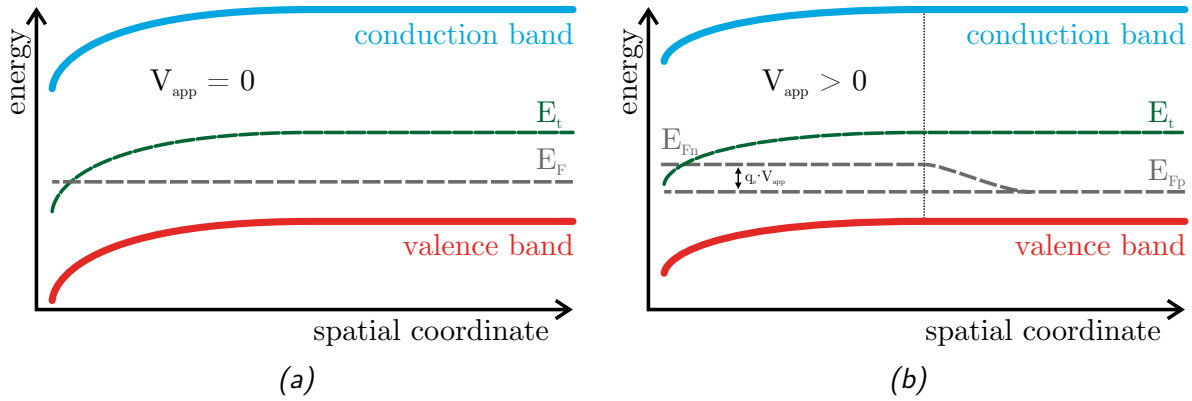

Figure 2.16.: ***Schematic drawings of p-type absorber in the dark with a deep hole trap.*** *- Depiction of the p-side absorber (a) with no bias (b) under an external bias in forward direction. Under a forward bias the bands are flattened, resulting in the trap level E_t not crossing E_{Fp} and therefore a reduction of N_{CV}.*

unreliable below 20° [68] and data points have to be disregarded.

CV measurement setup

Capacitance-voltage measurements are performed within the same setup as admittance measurements, utilizing the same LCR meter, usually at room temperature and with a small test voltage of 30 mV. The bias range if not stated differently is usually varied from −1.0 V to 1.5 V in 50 mV steps at frequencies of 10^1 Hz - 10^6 Hz in steps of one order of magnitude. To prevent hysteresis effects, the wait time after a DC bias change was set to at least 1 s. The utilized LCR-meter has a rather small current limitation, therefore cells were cut in smaller pieces to prevent overload through the combined AC and DC currents. Contacting of the front and back contacts was performed by glueing or if only measured at room temperature via press contacts.

CHAPTER
THREE

SAMPLE GROWTH AND PREPARATION

This chapter covers the fabrication process as performed to produce the $CuInSe_2$ samples studied in this work. Starting with a general description of the setup and procedures, which were employed to evaporate elemental copper, indium and selenium in order to form the absorber layers. A special attention is paid to describe this step in detail as the growth was part of the workload within the framework of this thesis and the electrical properties of the CIS material is the main focus of this study. Two different deposition approaches are described, the single stage process, during which all elements are evaporated at the same time, and the three stage process, which is distinguished by the successive deposition of In-Se and Cu-Se.
The section describes the preparation of these absorbers into solar cells and their final structure. Not only the structure itself, but also the deposition method of each layer can have an influence on solar cell performance and characterization. A short discussion of the chosen materials and methods is included here to give a complete description of the presented samples.
The final section describes a further treatment, that some of the studied samples were subjected to in order to improve their performance. Furthermore this treatment yields a special sample geometry, which can help to interpret some particular features of the electrical measurements, that are the main subject of this thesis.

3.1. Co-evaporation of $CuInSe_2$ absorbers

The Cu-rich samples were grown via a single stage co-evaporation process (see page 43), with a *Veeco Gen930* molecular beam epitaxy (MBE) system (See fig. 3.1 for a schematic description of the setup). However, since Mo-covered soda-lime glass was utilized as substrate the growth is non-epitaxial. Indeed all samples that were studied here are polycrystalline, hence in the following the process and setup will be referred to as physical vapour deposition (PVD) and not as MBE.
During each deposition process, four inch-by-inch substrates are mounted on a sample holder, which rotates in front of the sources to maximize homogeneity. The base pressure in the chamber during growth is usually between 10^{-8} and 10^{-9} Torr. Such low pressures are reached through a combination of turbo vacuum pumps and a liquid nitrogen cryopanel. The latter acts as a particle trap, to catch material that is not incorporated into the film and also extends in between the sources to thermally decouple them and prevent cross contamination.

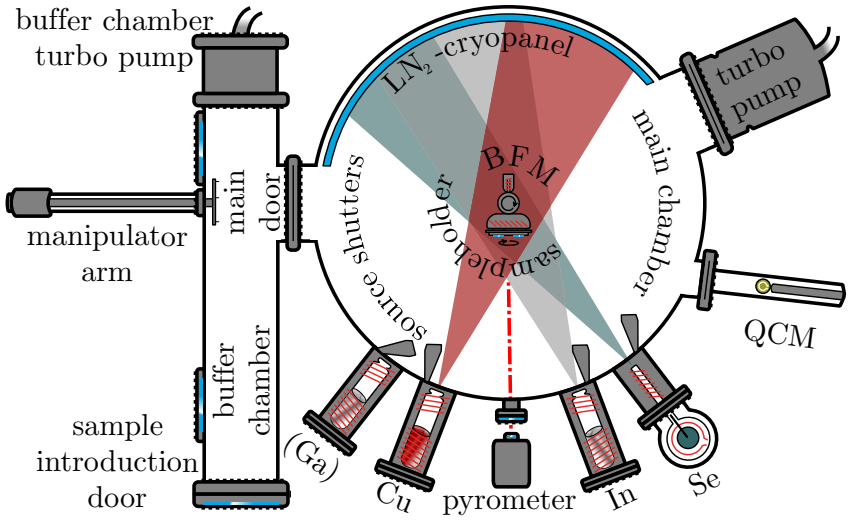

Figure 3.1.: ***Schematic drawing of the utilized PVD system*** *- (Description of drawing in the text below)*

The elemental sources are heated electrically above their contents respective melting points via two filaments, one at the top and one at the base. The flux of each metal (Cu & In) source is controlled by the temperature of the filament at the base. The one at the top is heating up the crucible tip in order to prevent material aggregation, which could obstruct the source. All effusion cells are covered by a shutter to switch the deposition of each element on and off. For the Se a valved source is used, whose flux can be controlled by the opening angle of said valve additionally to the temperature at the base. Furthermore it is equipped with a cracking tube, due to the trait of Se to form large ring molecules [80]. This cracker can be heated up to 1000 °C in order to split the Se molecules into smaller, more reactive species.
The growth chamber is equipped with different characterization tools for checking flux and growth rates, namely they are: quartz micro-balance (QCM), electron impact emission spectroscope (EIES), beam flux monitor (BFM) and a pyrometer.
The QCM is a piezoelectric crystal, whose natural frequency changes proportional to the mass that is deposited on top of it [81]. With known values of material constants for the deposits, namely the Z-ratio (also ratio of acoustic impedances, meaning the density $\times$ longitudinal velocity of sound of the deposit material compared to that of the crystal i.e. quartz) and density one can then calculate the growth rate and film thickness by measuring the oscillators' frequency. In principle this can be used to characterize any element, but in practice it is not possible to measure Se after having Cu deposited on the crystal. This is due to the formation of Cu_xSe that has a much lower density than Cu, leading to a rapid expansion of the deposit and subsequent destruction of the quartz crystal. Therefore this technique is only used before starting or in between processes after a delay, when the residual Se vapour has condensed to the walls.
The EIES tool consists of a filament, which emits electrons that excite the atoms, causing them to emit electromagnetic radiation specific to each element. This light passes through an optical filter and is then detected by photomultiplier tube (PMT) and converted to a flux rate. The filters are chosen that each of them only lets the radiation pass for one wavelength, specific to one element, therefore to detect different elements a multitude of filter and PMT assemblies are needed. While this also could be used for any element,

in the available setup this was only working for the Se, measured fluxes of all the other elements were influenced by each other and therefore are not significant.
The BFM is an ion gauge, which measures the pressure of the particle beam directed at it. It consists of a filament, that emits electrons towards a helical grid. A small fraction of these electrons collides with the atoms from the particle beam, thereby ionizing them. They are attracted to a negatively charged collector wire. The resulting current is measured and the pressure is calculated from that. The drawback of this method is, that it is highly dependent on system and process specific variables, for instance base pressure, angle between source and BFM and molecular species of incident particles. Therefore it can not by itself be translated into a growth rate.
The important thing to note is, that the evaporation rate of each cell is quite constant at a given temperature over a long time. In the case of the Se source, the valve opening also influences the flux rate, but under nominal operation the flux is stable here, too. This means flux rates are reproducible from one day to another, with only minor adjustments to the cells base temperature. Flux and cell temperature settings can be linked to final absorber composition by running a few calibration processes under variation of the cells temperature. Here, the temperature (and valve opening) is held constant for the In and Se source and the composition is adjusted by changing the copper source's base temperature. After deposition, the atomic ratios can be determined by EDX measurements and from this one is able to deduce the right cell settings that produce a specific composition.

Single stage process

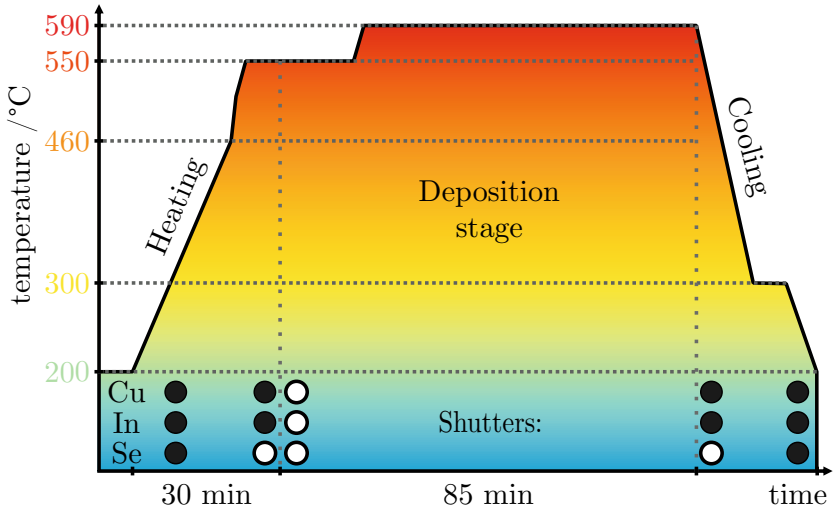

Figure 3.2.: ***Depiction of the single stage process*** *- The ordinate shows the substrate temperature setpoint, the abcissa the run-time of the process. The circles at the bottom of the graph indicate if the respective element is evaporating towards the sample (white) or closed (black).*

All Cu-rich samples studied within this thesis, namely the two different series to study the Se influence during growth on solar cell and defect properties (see chapter 4) and the bare absorbers before In-Se treatment (see chapter 5) were grown as described in the following. Before the beginning of the actual co-evaporation, the liquid nitrogen cooling is started in order to reduce the base pressure and the metal sources are heated up to their evaporation temperatures. Fluxes and deposition rates are recorded, utilizing the

BFM for all materials and the QCM only for Cu and In. Afterwards the samples are transferred from the buffer chamber onto the main chambers' substrate holder, which is facing away from the evaporation cells and the sample rotation is switched on.
The co-evaporation process itself then is automated after a user entered recipe, which will be described in the following. Fig. 3.2 shows a schematic drawing of a basic single stage process, as was used for the fabrication of the Cu-rich samples, studied within this thesis. The process starts out by heating the substrate holder to 460 °C with a ramp of 200 °C/min under vacuum (all temperatures that are given in the following, if not stated differently, refer to the the setpoint value of the heater, actual temperatures for example at the sample surface differ from this value and can be measured via the pyrometer). After supplying elemental Se from a valved evaporation source, the substrate holder is heated further to 510 °C in one minute and then with a lower ramp of 10 °C/min to the process starting temperature of 550 °C. As the Se flux needs a while to build up, it is beneficial to open the valve and shutter some time in advance of the actual deposition. Also, starting out with fast ramps and subsequently decreasing them once the substrate holders' temperature is close to its target value of 550 °C, is done in order to prevent drastic temperature overshoots, while still keeping the time required for heating up the substrate to a minimum.
Shortly after reaching process starting temperature, the sample holder is turned into growth position and the substrate is subjected to a Se atmosphere for 5 min. Exposure of the blank substrate to the Se atmosphere is done in order to promote the formation of a thin layer of $MoSe_2$ [82], which forms an ohmic contact [83]. Furthermore this step gives more time for the Se flux to stabilize before beginning of the deposition stage.
The co-evaporation commences with the opening of the shutters in front of the Cu and In sources. At the beginning the substrate holder is kept at 550 °C for 15 min before further heating to 590 °C, at which the process is held for 70 min. Afterwards the substrate holder is cooled-down to 300 °C, while still under a Se overpressure in order to prevent large Se losses from the absorber, due to the high vapour pressure of Se. Se valve and shutter are then closed and the substrate holder further cooled down to 200 °C, the temperature at which the samples can be extracted from the setup. As described previously, the Cu/In ratio was tuned by keeping the source parameters of In and Se constant, while only changing the Cu sources base temperature. Final Cu/In ratios as measured by EDX were around 1.2-1.5 for the low Cu-rich series and between 1.7 and 2.0 for the high Cu-excess and surface treatment series'. For the Se series, the Se flux was adjusted by changing the valve opening, while leaving all cell temperatures constant.

Three stage process

While it is possible to grow Cu-poor absorbers in a single stage process, Gabor *et al.* [84] found that an intermediate stage of Cu-excess during deposition of CIGS lead to consistent higher efficiencies and generally increased film quality and grain size. Therefore the Cu-poor series was grown in a modified three stage process, similar to that described in the cited work. All the samples from the Cu-poor series where grown as described in the following. In order to investigate the influence of the Se flux, the only difference in between the samples from this series is the amount of Se supplied during the whole process. This was varied by changing the opening of the Se valve, while keeping the evaporation and cracking temperature of the source constant.
The basic sequence as utilized for growing the Cu-poor samples, discussed in this thesis is shown in fig. 3.3. The steps up until after the samples have been introduced into the

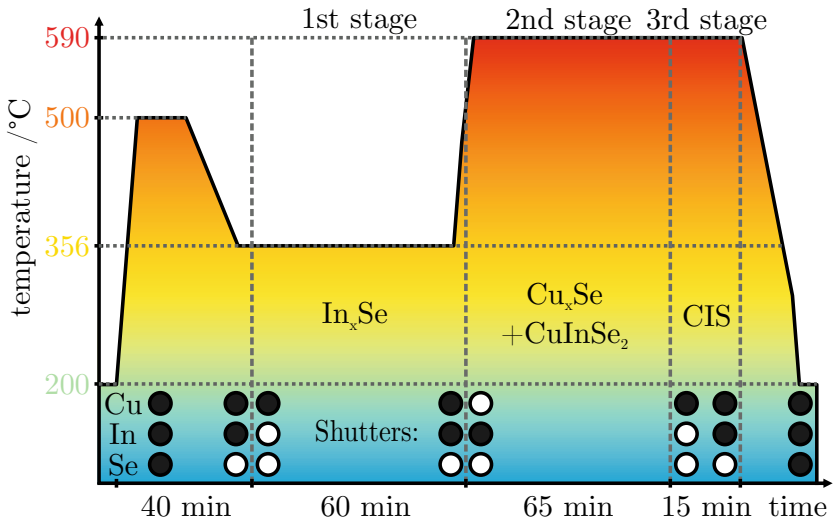

Figure 3.3.: ***Three stage process*** *- The ordinate shows the substrate temperature setpoint, the abcissa the duration of each stage. The circles at the bottom of the graph indicate if the respective element is evaporating towards the sample (white) or closed (black).*

chamber are the same as described in the previous section 3.1. The only difference here is a cleaning stage before the actual deposition begins. During this step, the substrate holder is heated up to 500 °C for about 20 min in order to remove oxygen or other surfactants from the Mo back contact. This is necessary in the case of the three stage process, since it starts out with a low temperature stage. This low temperature might not suffice to remove the aforementioned impurities, in contrast to the single stage process, which directly starts out at high temperatures.
After the cleaning stage the temperature is reduced to around 360 °C and the substrate is exposed to a Se atmosphere for 5 min, again similar to as described in section 3.1. The process is started by growing In_xSe for approximately an hour. The actual length of this stage depends on the fluxes and desired film thickness and is checked by using the pyrometer. Due to interference within the deposited layer, the histogram of the pyrometer displays maxima and minima, from which one can estimate the films thickness.
Once the desired value is reached, the In shutter is closed and the substrate heated up to around 470 °C. At this temperature the second stage commences with opening of the Cu shutter and simultaneously increasing the temperature further to 590 °C. The purpose of this stage is a recrystallization and enhanced growth of CIS grains due to the presence of Cu_xSe [84], therefore this stage continues well until after growth of this secondary phase has started.
The easiest way to detect the appearance of this secondary Cu_xSe phase is monitoring the output power P_{subs} of the substrate heating. After starting the Cu-Se supply until all the In_xSe has been transformed into CIS, the value of P_{subs} stays rather constant. But as mentioned before (see section 2.1), growth close to or above stoichiometry is characterized by an emerging secondary phase of Cu_xSe. Since this phase is metallic, it has a high emissivity, therefore the appearance of this phase is accompanied by enhanced heat dissipation from the substrate. This manifests itself as an increase in the value of P_{subs}, due to the temperature regulation counteracting the higher cooling rate by ramping up the heating.
Usually 10 min after the start of Cu_xSe growth the second stage is aborted by closing the

Cu and opening the In shutter at the same time. The length of the third stage depends on the In and Se fluxes, which determine how long it takes to transform all the Cu_xSe back into $CuInSe_2$ and the desired value of Cu deficiency is reached. To find the time needed in order to produce a certain Cu/In-ratio, a few calibration processes under variation of the third stages length need to be performed. Afterwards, EDX measurements can be utilized to measure the different Cu/In-ratio as a function of third stage duration. For the presented Cu-poor samples the Cu/In-ratio was set to be constant and the third stage ran for approximately 15 min, producing samples with a Cu/In-ratio between 0.92-0.98. The cooling procedure is carried out in the same way as before, by closing the In shutter, cooling of the substrate to 300 °C and subsequent disruption of the Se flux and finally extraction of the samples at 200 °C.

3.2. Solar cell preparation from $CuInSe_2$ absorbers

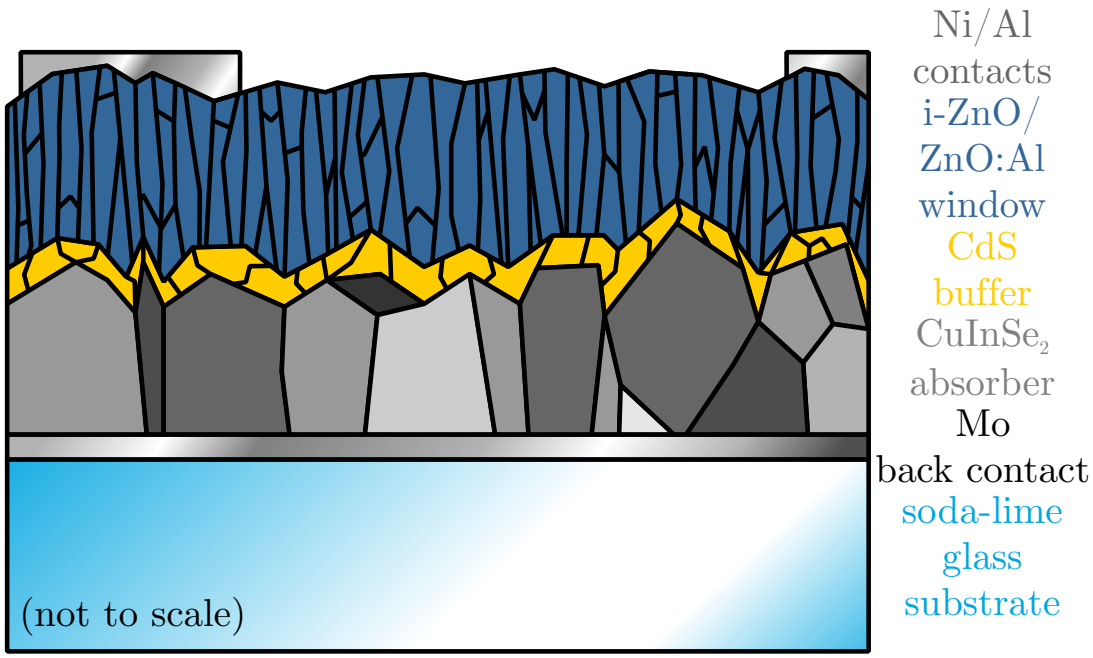

Figure 3.4.: ***Structure of a $CuInSe_2$ solar cell*** *- Schematic drawing of the structure of the solar cells, discussed within this thesis. A 2 mm thick soda-lime glass substrate is covered with 480 nm of molybdenum as the solar cell's back contact. The CIS absorber is about 3 μm thick and covered with a CdS buffer of 40-50 nm. On top of that is the window layer, which consits of 80 nm i-ZnO and 450 nm Al:ZnO. The front contacts are made of 10 nm Ni and finished by 2 μm Al.*

All samples discussed within this thesis are based on the same sequence of layers, which has first been published in 1986 by Potter *et al.* [85] and is shown as a schematic drawing in figure 3.4. More information about alternative structures, materials and methods can be found in reference [86]. This sample structure is more elaborate than the simple pn-junction, described in chapter 2.2.1, due to the unique challenges and properties of chalcopyrite thin-film solar cells.
One of the advantages of thin-film technology is the possibility to work with a multitude of different substrates. And even world-record efficiencies have been achieved on

flexible polymers [14]. In this work soda-lime glass with a thickness of 2 mm was used as substrate for a number of reasons. Not only is it a rather inexpensive material and with a good thermal stability allowing for high process temperatures. Moreover Stolt *et al.* [87] published results showing an improved grain growth and layer structure for $CuInSe_2$ grown on this type of substrate. They linked these improvements to the good match in thermal expansion of substrate and layer, however later studies looking deeper into the subject found advantages beyond just this. Ård *et al.* identified sodium diffusion from the substrate as not only being conductive for the improved crystal growth, but also first indicated its role as a beneficial dopant [88].
The back contact consists of about 480 nm of magnetron-sputtered molybdenum with a sheet resistance between $15 - 20\ \mu\Omega \cdot \mathrm{m}$. As already mentioned in section 3.1, exposure to Se during or before absorber growth might boost the formation of $MoSe_2$ at the absorber/Mo interface to produces an ohmic contact [83]. Even though early work by Russel *et al.* [89] suggested that the Mo/CIS heterocontact forms a Schottky barrier. Later measurements, performed directly on the Mo/CIS interface in a working solar cell contradict this and find an ohmic behaviour [90]. Either way Mo is a suitable and inert [91] back contact material. If sputtered under the right conditions it provides a low stress and pore-free foundation for CIS growth [92, 93], while still allowing for Na diffusion [94].
The p-type absorber layer is the here studied $CuInSe_2$ grown by PVD as described in the beginning of this chapter on top of the Mo. Due to its high conductivity, the Cu_xSe that forms for Cu-rich material has to be removed from the CIS surface before finishing of the solar cells. An etch of 10 wt% KCN in water for 5 min is usually enough in order to thoroughly clean away all Cu_xSe even at high Cu/In ratios (here up to 2.0). Additional this etch reverses sample degradation due to oxygen exposure before the buffer layer deposition fully halts this process [37]. Therefore also the Cu-poor samples are etched for 30 s in an aqueous solution with a decreased concentration of 5 wt% KCN in water.
To minimize air exposure the samples are carefully rinsed and then directly the chemical bath deposition (CBD) of the CdS buffer layer is started. For this, the samples are submerged into a bath of water, ammonium hydroxyde (NH_4OH), cadmium sulfate ($CdSO_4$) and thiourea ($(NH_2)_2CS$). To prevent formation of colloidal CdS the bath temperature is slowly raised from room temperature to 67 °C. The ammonia degradates the cadmium and sulphur-sources, $CdSO_4$ and $(NH_2)_2CS$, respectively, to allow the formation of CdS on top of the absorber. Final layer thickness is approximately $40 - 50$ nm, which is reached after about $8 - 9$ min depending on the reaction rate. Despite some optical losses in the short wavelength region due to partial absorption within this buffer layer, there are several benefits that far outweigh this factor. Some of these benefits are: a favourable band alignment [95], longer carrier lifetimes [96], an increase of depletion width, coating of the absorber surface to prevent local shunting, protection against sputter damage [97].
The high bandgap n-side of the junction is formed by the window layer, which consists of a transparent conductive oxide (TCO). In the present case this is a magnetron sputtered double layer structure of intrinsic and Al doped ZnO. Both CdS and i-ZnO are rather highly resistive and increase the series resistance of the solar cell device. This series resistance limits electronic losses, that otherwise occur due to areas with a lowered open-circuit voltage [98]. The thickness of the intrinsic layer is about 80 nm, bringing the total window thickness to 450 nm together with the Al:ZnO. The window features a high transparency to allow light to pass through to the absorber layer and high conductivities for charge extraction.
The final step for the here presented devices is the e-beam evaporation of the front con-

tacts. This has the drawback of increased shading losses, due to the opaque nature of the metal grid, but the advantages are a better current collection. Furthermore in the framework of this thesis, the ability to contact the cells into the different measurement setups via press contacts or conductive glue is essential. The rather stable grids offer mechanical protection from scratching of the press contacts, while also providing a barrier against in-diffusion of silver ions from the glue. For this purpose a thin layer of about 10 nm of Ni is deposited prior to 2 µm of Al, which results in good adhesion and stability of the grid. After all the layers have been deposited, the samples are divided into 8 distinct solar cells, by a mechanical scribing.

3.3. Indium-Selenium surface treatments

The advantages of Cu-rich grown $CuInSe_2$ have been described in section 2.1.1. However, this material features some unique challenges, which can largely be traced to either the interface itself or a region close to it, as will be described more thoroughly in chapter 5. Therefore, while most of the favourable properties of the Cu-rich material lie within the bulk, the Cu-poor CIS/CdS constitutes the better interface. To combine the best of both, a surface treatment has been developed previously [99, 100].
In the following section the procedure to perform this treatment will be described. The basic principle is to deposit a thin layer of In_xSe on top of the etched stoichiometric absorber. At sufficiently high temperatures Cu can diffuse from the bulk into this layer and thus transforming it to a Cu-poor $CuInSe_2$. The crucial point is to limit Cu diffusion, in order to prevent the whole absorber from turning Cu-poor, which corresponds to a layer temperature no higher than 300 °C [99].
Cu-rich absorbers are etched, to remove all Cu_xSe from the surface as described in section 3.2 and then re-introduced into the PVD setup. In contrast to the normal deposition process, in order to allow for low deposition temperatures the substrate holder is heated to no more than $150 - 220$ °C, which corresponds to layer temperatures (as measured by the pyrometer) of $200 - 300$ °C. With the substrate facing away from the cells, the Se valve and shutter are opened, in order to allow the flux to stabilize, while not subjecting to excessive amounts of Se. After the flux has settled, the sample is rotated in and the In shutter opened to start the deposition stage. This deposition stage lasts for $0.5 - 3$ min. Two different processes are distinguished, first a In-Se deposition-only process, that is performed at sample temperatures of either 275 °C or 300 °C, during which Cu diffusion from the stoichiometric bulk occurs and ideally there is a direct formation of the Cu-poor CIS surface. The second process is a deposition-annealing process, where the In-Se deposition is performed at 200 °C. Afterwards the In shutter is closed and the sample temperature is increased to 300 °C, while still under an Se overpressure. This stage then lasts to up to 15 min. In both cases the temperature of the sample holder is then decreased to 200 °C under a Se atmosphere. Before extraction the Se supply is cut-off and the sample holder is then cooled to 150 °C. Afterwards the cell are finished in the standard configuration, as described in section 3.2.

CHAPTER

FOUR

SELENIUM INFLUENCE STUDY

Chapter 2.1 discussed some properties of $CuInSe_2$ in general and in particular the advantages of material grown under Cu excess [101]. However so far, even though CIGS technology already reached maturity and is commercially available, world record efficiencies [14, 102] and modules [103–105] are all made from Cu-poor material. The problem is that the measurements, which show advantages of the Cu-rich material are mainly performed on etched, but otherwise bare absorbers. However already after deposition of the buffer layer the picture changes, with the disappearance of the advantage in Fermi level-splitting [37]. Measurements on the finished devices show the Cu-rich perform worse than the Cu-poor ones in all the metrics: lesser short-circuit current densities and open-circuit voltages, decreased fill factors, but high saturation current densities and diode quality factors [106].
This behaviour can be traced back in part to a too high doping density within the Cu-rich absorbers [106]. Due to this the absorbers suffer from a very short SCR, which means that the built-in voltage is applied over a very short distance leading to high electric fields in the absorber. This not only reduces the V_{OC} through a high recombination at the interface, which is reflected by the low activation energy of the main recombination pathway as measured by IVT [107], but also affects the current. Despite collection lengths in the range of the absorber thickness Cu-rich devices exhibit reduced quantum efficiencies over the whole wavelength range compared to Cu-poor devices. This behaviour has been attributed to tunneling enhanced recombination within the SCR due to the previously mentioned high electric fields [106].
Previous studies have shown that the Se supply during CIS growth can be crucial for the intrinsic doping density of the material and can even lead to type inversion under very low Se overpressures [108]. The Se flux during growth of the Cu-rich material was studied within this thesis and the influence on the doping could be confirmed [109, 110]. In the following results of electrical measurements on samples grown under different Se overpressures will be presented. The goal is to achieve a better understanding of the defects in Cu-rich grown CIS and especially get insights on the influence of the Se supply during deposition. Part of these results have been published [111], this chapter will discuss and elaborate on the findings.
Three series of 3 samples each were fabricated, as described in chapter 3 and finished into solar cells of the standard structure (see section 3.2). For each series the Cu/In flux ratio was kept constant, while the Se flux was varied in a way that for each series a low, medium and high Se flux sample was produced with comparable fluxes. Two Cu-rich

Table 4.1.: *Absorber performance as measured by IV at room temperature under AM 1.5 illumination.*

Cu/In	Se	η %	J_{SC} (IV) $mA \cdot cm^{-2}$	J_{SC} (QE) $mA \cdot cm^{-2}$	V_{OC} mV	$\mathcal{FF}$ %	A	R_S Ω	R_{Sh} Ω	J_0 $mA \cdot cm^{-2}$
high	low	7.2	37.8	39.6	361	52.9	2.3	0.4	1736	6.1E-05
	mid	6.0	39.7	39.1	311	48.3	2.3	0.5	629	8.3E-05
	high	6.5	40.3	39.1	325	49.7	2.2	0.3	238	4.4E-05
low	low	7.5	38.4	38.8	359	54.0	1.9	0.4	272	1.0E-05
	mid	6.1	37.3	38.2	327	50.3	2.0	0.5	471	2.6E-05
	high	6.2	36.5	38.0	330	51.7	2.0	0.4	319	2.0E-05
Cu-poor	low	12.4	39.8	40.7	454	68.6	1.5	0.5	1220	1.2E-07
	mid	12.1	41.4	40.8	438	66.6	1.5	0.5	2160	2.0E-07
	high	9.9	38.2	40.0	419	61.9	1.8	0.6	4950	2.4E-07

series at different Cu/In ratios were produced by a single stage process and one Cu-poor series, with a small Cu deficiency, by a three stage process(see section 3.1). All samples were characterized, utilizing the electrical measurement techniques discussed in chapter 2.3.

4.1. Solar cell performance

To assess the influence of Se overpressure on device performance, current-voltage characteristics at room temperature of the finished devices were recorded in the dark and under illumination, following the methodology described in chapter 2. The extracted parameters at room temperature are given in table 4.1, the measured IV curves for the different samples are shown in figure 4.1.

They all follow a trend regarding the power conversion efficiency - the sample with the lowest Se flux during growth is always the most efficient. This trend can mostly be attributed to the significant difference in open-circuit voltage, but also the fill factors of the low Se samples are slightly better. As discussed previously the Cu-rich cells exhibit a much lower voltage than the Cu-poor reference samples [106,107], the low Se environment alleviates this, but does not fully close the performance gap.

The short-circuit current densities do not display a similar trend over all series when measured in the IV setup. For the low Cu/In ratio series the trend follows the Se deficit, while for the high Cu/In series it seems to be the opposite trend and for the Cu-poor series there is no trend at all. This might have to do with methodological problems of the IV measurement itself, since the currents are highly dependent on the light source. A number of factors might play into this, for example different shadings and cell sizes or a fluctuation of the output power of the lamp, therefore the given values might not be exceedingly reliable.

Another method to evaluate the current of a solar cell device is from QE measurements, this has the added benefit that a standardized solar spectrum is used instead of a halogen lamp and therefore offers increased comparability to literature.

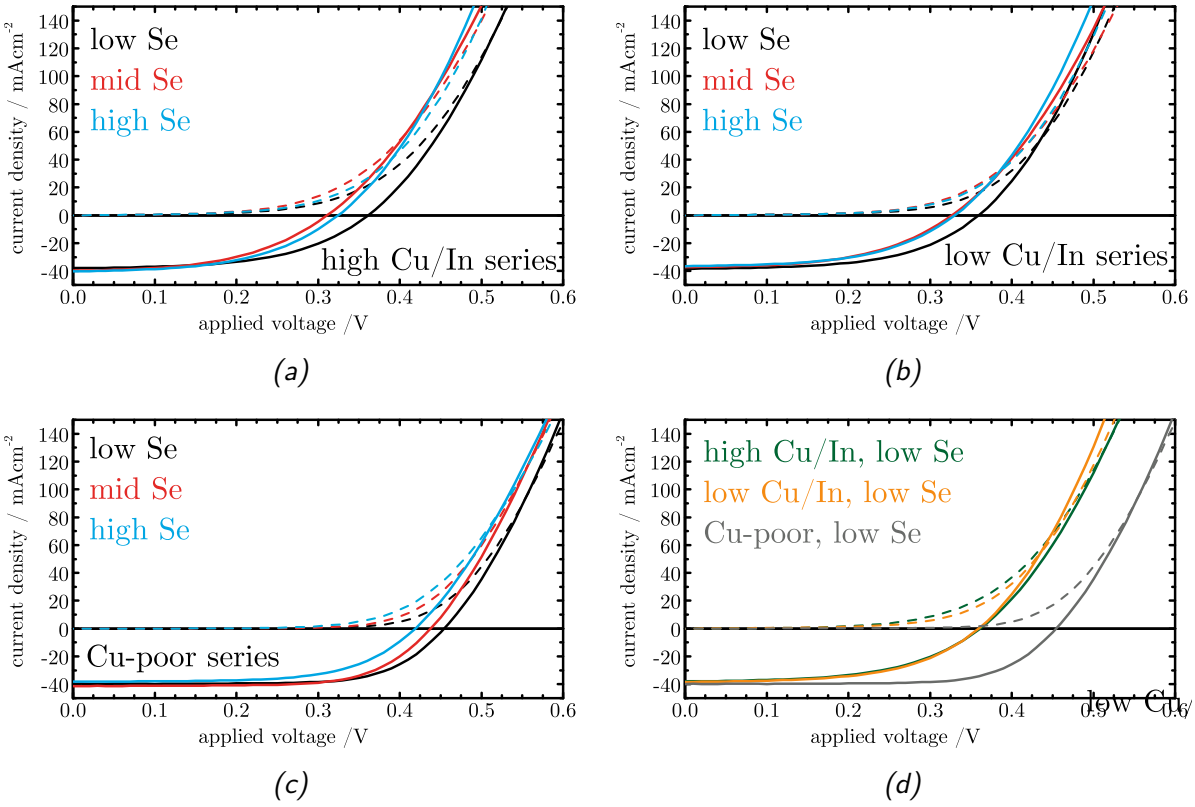

Figure 4.1.: ***Results of the IV measurements on the 3 series.*** *- a) IV of the series with a high Cu/In b) IV of the series with a low Cu/In c) IV of the Cu-poor comparison series d) Comparision of the sample with the highest power conversion efficiency of each series. The dashed lines are the IV curves recorded in the dark and the solid lines under illumination.*

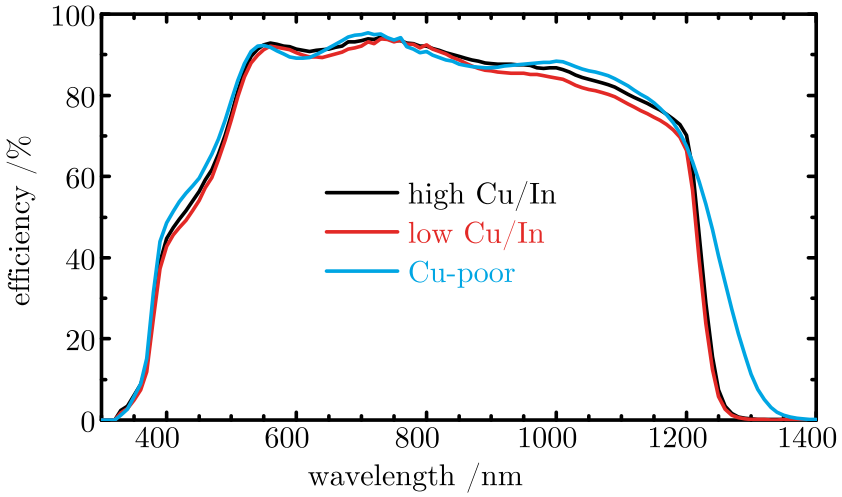

Figure 4.2.: ***QE series comparision*** *- Graph of the QE for the samples with the highest short-circuit current density of each series.*

Results of the QE measurements on the three series are shown in figure 4.3 and a comparison of the highest short-circuit current density samples is given in figure 4.2, the AM 1.5 spectrum [112] was utilized for current evaluation. The values of the integration are given in table 4.1 for comparison to the values from IV.
For this evaluation method the short-circuit current densities now follow the same trend,

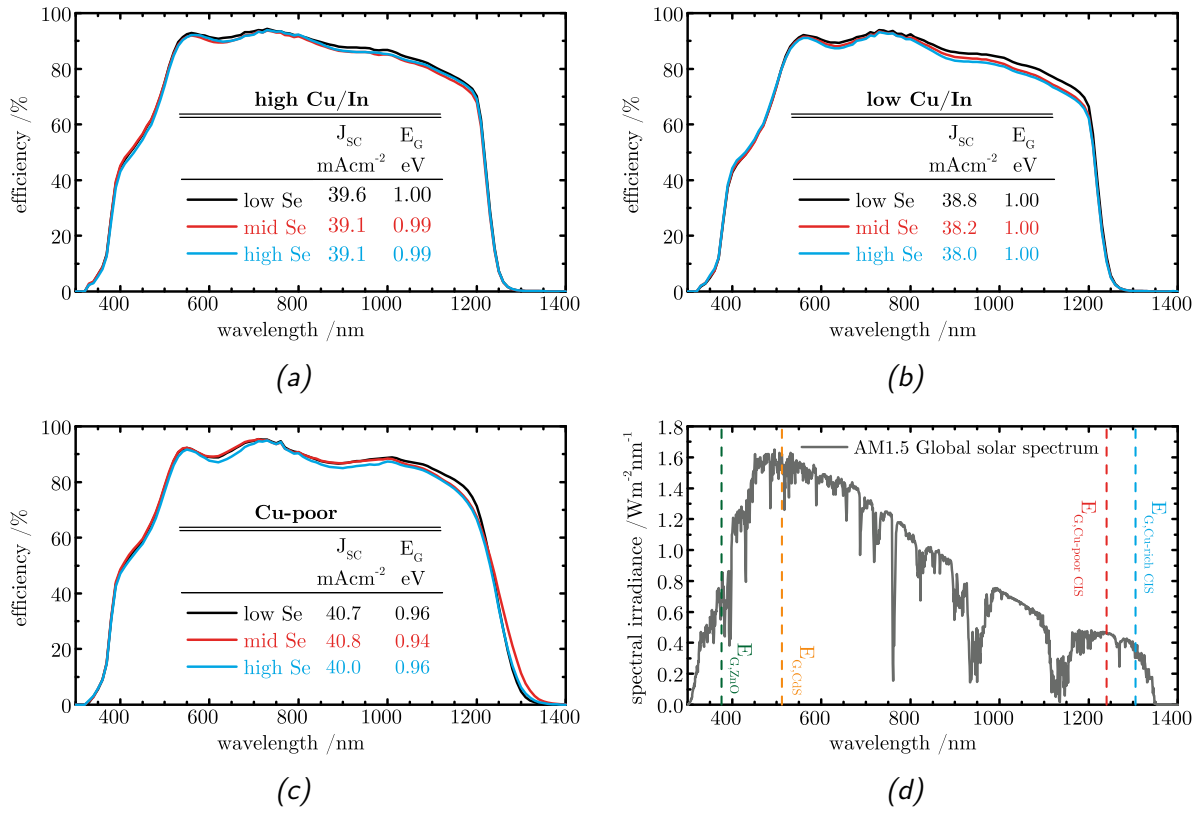

Figure 4.3.: ***Results of the QE measurements on the 3 series.*** *- a) QE of the series with a high Cu/In b) QE of the series with a low Cu/In c) QE of the Cu-poor comparison series d) AM 1.5 spectrum in the range with bandgaps of different materials (taken from [112])*

as the open-circuit voltages and the best cells are again those grown under low Se. Furthermore, while the Cu-poor samples still display the highest currents, the high Cu/In cells are only about 1 mA $\cdot$ cm^{-2} behind.
Interestingly this difference is mostly due to the slightly smaller bandgap of the poor material comapred to the rich, which is visible as the area between the long wavelength slopes of the Cu-poor and the Cu-rich samples (see figure 4.2). Evaluation by extrapolation of the QE as described in section 2.3.2, yields a difference of about 50 meV (Cu-rich: $E_g = 1$ eV, Cu-poor: $E_g \approx 0.95$ eV).
Integrating the product of QE difference and AM 1.5 spectrum yields slightly less than 1 mA $\cdot$ cm^{-2}. Therefore the first interesting result from this study is that the low Se, Cu-rich samples are on par with the Cu-poor ones in terms of collection, when the larger bandgap is taken into account. The slight short-circuit current density gain of around 0.5 mA $\cdot$ cm^{-2} for the samples with low Se can be attributed to a decreased doping, which will be shown in the following section. This increases the space-charge region width, leading to a slightly better collection of charge carriers and therefore J_{SC}.

Evaluation of series and shunt resistances, saturation currents and diode quality factors was performed via ECN's IVFit [53] on the dark IV measurements. While the Cu-poor devices exhibit diode quality factor values between 1 and 2 as expected for decent devices, the values of Cu-rich samples were all above or close to 2 as has been observed before [106] for Cu-rich material. In the cited work this was attributed to a high doping of the Cu-rich material, which leads to a high electric field within the SCR that facilitates tunnelling enhanced recombination at the interface and lowers the open-circuit voltage [107]. The slightly worse short-circuit current density of the Cu-rich cells compared to the Cu-poor ones is in part due to a slightly thicker CdS layer. This can be seen in the wavelength range between $400 - 500$ nm as a slight advantage for the Cu-poor material.
However, this does not explain the difference at longer wavelengths where the Cu-poor shows a larger QE at 1000 nm. It is possible that due to the still rather high doping of the absorbers the SCR width is reduced which decreases the collection in the long wavelengths for the Cu-rich. In the previous works on Cu-rich grown $CuInSe_2$ [106], this was not the case and their collection length was usually longer than the absorber thickness. Which would mean, that there is a new collection problem with the Cu-rich samples shown here.
To further investigate the temperature behaviour of the diode quality factors, IVT curves were recorded for all the 3 series. Figures A.1, A.2 and A.3 at the end of this section show all the temperature dependent IV curves for the two Cu-rich and the Cu-poor series, respectively.
Comparing the graphs the first thing noticeable is the comparatively low reverse diode breakdown voltage of the Cu-rich devices. While there is basically no current change in reverse bias for the Cu-poor device the Cu-rich ones exhibit a strong current increase already at low reverse voltages. This reverse voltage breakdown can be due to three effects [50]: thermal instability [113], avalanche multiplication [114] and Zener effect [115].
Thermal instability occurs due to a positive feedback between the temperature and the reverse current: the reverse current heats up the sample and the increase in temperature in turn increases the reverse current.
Avalanche multiplication is the effect that under high electric fields minority carriers generated within the space-charge region can accelerate until they can ionize an electron-hole pair that in turn gains kinetic energy from the field, resulting in current multiplication.
Both effects can potentially be destructive for the device due to heat dissipation from the high reverse currents. Since they should both only occur at high reverse biases [50] outside of the utilized voltage range and none of the measured devices was damaged during IV measurements they are probably not the cause for the observed breakdown.
Most likely the Zener effect, which describes the tunnelling of minority carriers over the forbidden zone is responsible for the low reverse breakdown of the Cu-rich devices. A voltage applied against the junction direction increases the band-bending, which leads to a situation where the conduction band of the window layer moves below the valence band of the absorber.
With a short space-charge region both bands are very close to each other, resulting in a high tunnelling probability for minority carriers. Due to the increase of E_g under decreasing temperature the temperature coefficient of the Zener effect is negative, meaning the breakdown voltage increases with decreasing temperature [50]. This is observed in the IVT measurements of the Cu-rich series as a flattening of the curves in third quadrant of the J-V diagrams going towards lower temperatures. The difference between Cu-rich and Cu-poor samples could be an indication of a higher electric field in the former due to a high doping density (as is confirmed by CV measurements, see section 4.2).

As illustrated in chapter 2, the activation energy of the dominant recombination pathway $E_{A,rec}$ can be extracted from the IVT measurements by extrapolation of the high temperature open-circuit voltage values towards 0 K.
Results of this are shown in figure 4.4. All y-intercepts for Cu-poor samples are greater

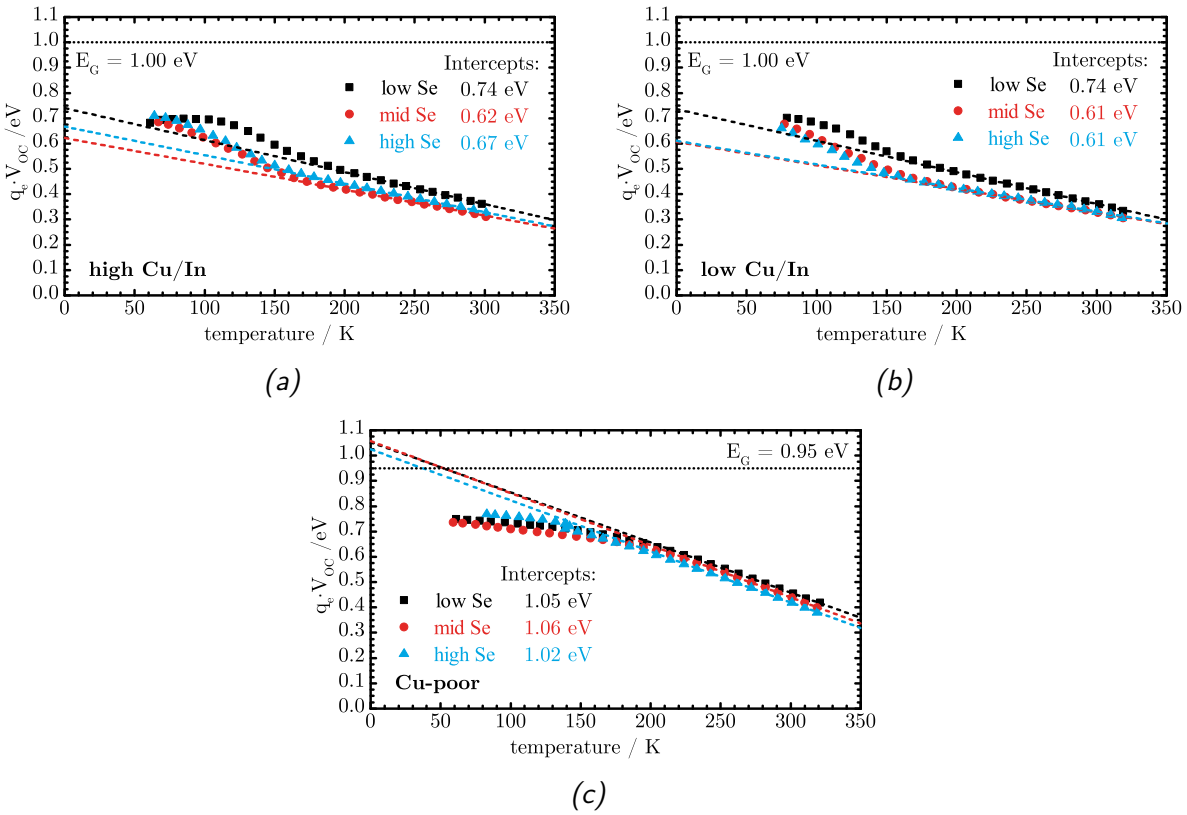

Figure 4.4.: ***Open-circuit voltage extrapolation of the IVT measurements on the 3 series.*** *- (a) high Cu/In (b) low Cu/In (c) Cu-poor. The Cu-poor series samples all extrapolate to E_g. While there seems to be a trend towards higher $E_{A,rec}$ values for lower Se flux samples, the Cu-rich devices are all still dominated by recombination close to the interface.*

than 1 V, while the Cu-rich samples all extrapolate to values in between $0.60 - 0.75$ V. Comparing these voltages (multiplied with the elemental charge q to transform them in an activation energy) to the bandgaps as extracted from the QE measurements it is directly visible that while all the Cu-poor samples extrapolate to a value close to that of their bandgap, the Cu-rich samples all lie $0.3 - 0.4$ eV below. There is a trend towards higher activation energies with less Se during growth for the Cu-rich samples, but still a significant deficit in respect to E_g is present even for the best sample indicating that these devices are still dominated by recombination close to the absorber/buffer interface. As expected, the Cu-poor samples do not show this, they all extrapolate to the bandgap and therefore the recombination mostly takes place within their bulk.

Summing up it becomes apparent, that a lowered Se supply enhances the performance of the Cu-rich devices in a number of ways. First overall efficiency is higher for the low Se flux devices, as can be seen in the improvement of the open-circuit voltage. QE measurements show that furthermore the short-circuit current density is increased and - taking into account the higher bandgap - on par with the Cu-poor material. There might

be a trend towards lowered impact of tunnelling recombination and a shift away from the interface.
To further investigate these, CV measurements can give an insight into the doping, which is the topic of the next section 4.2.

4.2. Doping

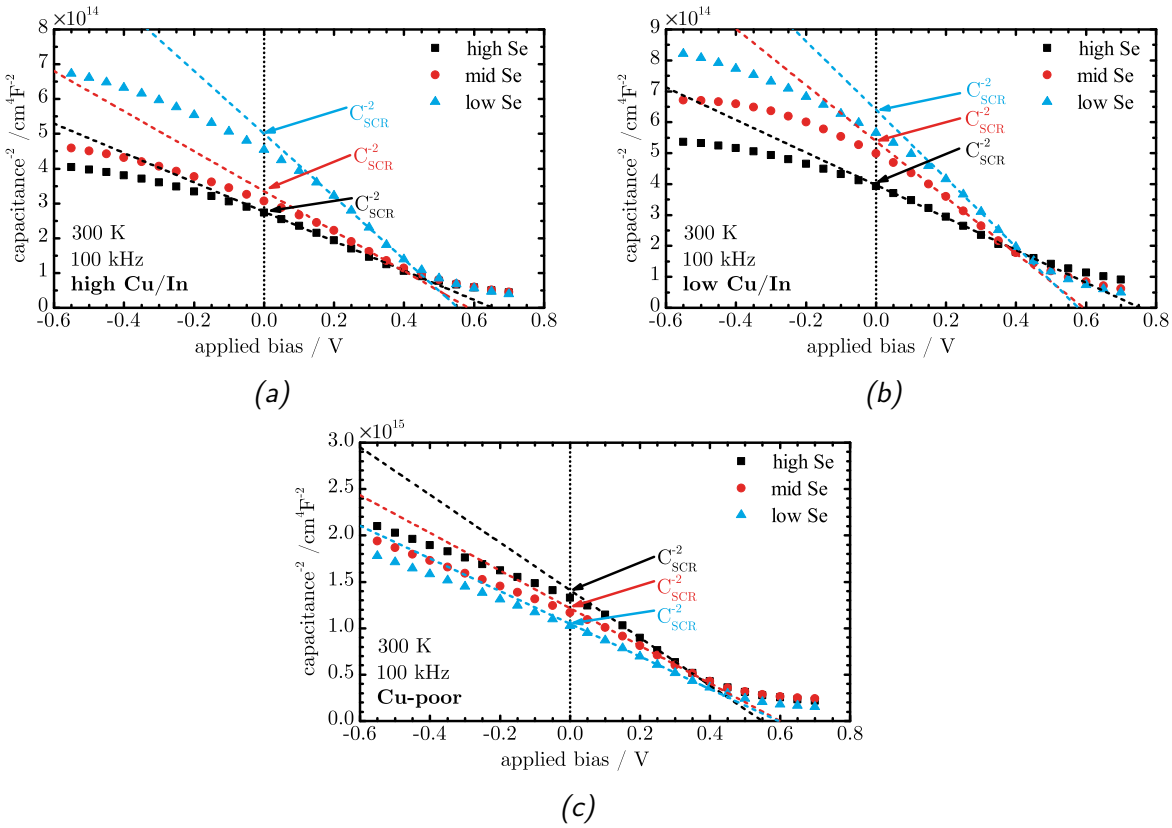

Figure 4.5.: ***Results of the CV measurements on the 3 series.*** *- (a) high Cu/In (b) low Cu/In (c) Cu-poor. The Cu-poor series samples are characterized by a low doping density with a slight increase at lower Se fluxes. The Cu-rich ones which have high N_{CV}s but show the opposite trend with decreased Se during growth.*

Capacitance-voltage measurements have been performed on small samples as described in section 2.3.6. Small samples in the present case means compared to the usual size of about 0.5 cm^2. They were scribed at approximately two thirds of their length, so that a total area of less than 0.2 cm^2 remains around the front contact pads.
The results of CV measurements on the three series are shown in figure 4.5 and summarized in table 4.2.
The doping densities are inversely proportional to the slope of the Mott-Schottky plot, therefore it is easily visible that there is a trend for both Cu-rich series towards lower doping densities with lower Se fluxes. For the Cu-poor series this trend is reversed and lower Se increases the absorber's doping. The same trends are found in the built-in voltage, which decreases with the Se flux in the Cu-rich devices, while it rises slightly in the Cu-poor series.
Another feature, which is displayed in all devices across all series is the flattening in

Table 4.2.: *Absorber parameters as extracted from capacitance-voltage measurements*

Cu/In	Se	N_{CV} cm^{-3}	V_{bi} mV	x_{SCR} nm	C_{scr} $F \cdot cm^{-2}$
high	low	$1.3 \cdot 10^{16}$	550	230	45
	mid	$2.1 \cdot 10^{16}$	580	190	55
	high	$2.9 \cdot 10^{16}$	650	170	60
low	low	$1.1 \cdot 10^{16}$	580	260	40
	mid	$1.3 \cdot 10^{16}$	590	240	43
	high	$2.3 \cdot 10^{16}$	750	210	50
Cu-poor	low	$6.9 \cdot 10^{15}$	600	340	31
	mid	$5.9 \cdot 10^{15}$	600	360	29
	high	$4.7 \cdot 10^{15}$	550	390	27

reverse bias around 0 V. This can be attributed to the presence of deep defects, which contribute to N_{CV}. The methodology of evaluation has been chosen to minimize their effect, as discussed in section 2.3.6.
The flattening at high forward biases is most probably an artefact of the measurement due to an overload (because of current limitation) of the LCR-meter, as discussed in section 2.3.6, it is also visible as a strong decrease of the phase angle.
Together with the results from the last section (4.1) it comes to light that the decrease of doping within the Cu-rich devices has a favourable effect on the performance of these solar cells. As mentioned previously the activation energy of the main recombination pathway of the V_{OC} is increased towards the bandgap value for lower Se fluxes. From the observation from CV measurements that doping and built-in voltage decrease with the Se flux the argument can be made that due to the flatter band-bending profile at the absorber/buffer interface the holes can only tunnel into interface states that are closer to the valence band and recombine from there. Due to this the activation energy of the open-circuit voltage increases but is still below the bandgap value.
The second effect might also be due to the lower doping the hole density close to the interface is reduced, decreasing the trapping rate. Less trapping in this case results in less recombination, leading to the observed increase in V_{OC} of around 50 mV for a reduction in the doping by approximately half.

The decrease in doping density has been explained in reference [109] by a possible increase in compensating defects. In the reference a mechanism was proposed, by which the doping density is reduced during lower Se supplies. The lack in Se atoms is resulting in vacancy type defects, which can form complexes together with the already abundant Cu vacancies, which can be found in both Cu-poor and Cu-rich material [30]. These Se-Cu double vacancies are donors (in equilibrium [116]) and might therefore compensate the p-type doping. Furthermore the In-on-Cu antisite defect might also increase compensation, it has been shown that formation of this defect is enhanced by Se-poor conditions [117].
The Cu-poor samples however, show a tendency towards higher efficiency with higher doping, especially comparing the low and high Se flux samples, there is a 2.5 % efficiency

advantage for the prior. Comparing the doping densities, there might be a trend towards higher doping levels with lower Se during growth, it is questionable that this change might explain the whole difference in efficiencies.
In any case, the results of the IVT measurements (figure 4.4c) suggest that there are probably different mechanisms at work in Cu-poor cells than the ones for the Cu-rich samples. It is directly apparent that all of the Cu-poor samples are dominated by bulk recombination, since all their open-circuit voltages extrapolate to E_g.
Therefore the simplest explanation for the difference in V_{OC} of the Cu-poor is just the lower built-in voltage of the sample with high Se during growth, since interface recombination is no issue for them the open-circuit voltage of the low Se samples can follow the increase in built-in potential.

Evaluation of the short-circuit current density, yields different behaviours in QE and IV. While the QE measurements show a slight trend towards higher values for lower Se during growth, the IV measurements show no trend. The different IV results are most probable an artefact do to inhomogeneous lighting of the samples during the measurement. Therefore the values from the QE measurement should be trusted. The increase in J_{SC} seem to indicate a slightly higher diffusion length for the low Se fluxes.

4.3. Defects in Cu-rich devices

Admittance spectra of the Cu-rich samples typically show up to four different signals, they are labelled 1 to 4, with decreasing temperature at which temperatures they appear. A typical capacitance spectrum is shown in figure 4.6.
In the figure different significant capacitance values have been marked. The two blue, dashed lines mark the space-charge region capacitance C_{scr} and the geometrical capacitance C_{geo}. The first one is calculated, using the doping density from CV measurements under the assumption of a one sided PN-junction (see formula 2.54), which is also equal to the y-intercept of the Mott-Schottky plot. It marks the line between shallow and deep defects in the TAS spectra, as deep traps should contribute an additional capacitance to C_{scr}, while shallow traps subtract from it.
The geometrical capacitance is calculated by assuming a plate capacitor, formed by the front window/buffer and back contact with the dielectric absorber ($\epsilon_r = 12$ [52]) in between. This situation occurs at low temperatures, after the carrier and mobility freeze out, when there are no more free carriers in the bands and no hopping conduction is possible. This marks the lower limit of the capacitance spectrum of all samples.
Therefore the last step, corresponding to either the freeze-out of the shallow doping defect or of the mobility should level at C_{geo}.
The Cu-poor samples exhibit one less step in the spectrum (see figure A.6). From looking at the temperature ranges in which each signal appears, the energies extracted from the Arrhenius plots (table 4.3) and lastly the Meyer-Neldel graph (shown in figure 4.7 will be discussed later), one can deduce, that the missing signal is step 2. Therefore the remaining signals are labelled accordingly 1, 3 and 4.
The signal that is already visible at room temperature (step 1) is usually very broad and more pronounced in the Cu-poor series. Since the measurement is limited to frequencies between $10^2 - 10^6$ Hz it is usually not possible to assign an energy to this signal. In all but one sample the signal appears below this range already at room temperature, therefore only an increase in capacitance at low frequencies is visible, not the inflection point.
It is assumed that this signal is either due to a very broad deep defect distribution or band

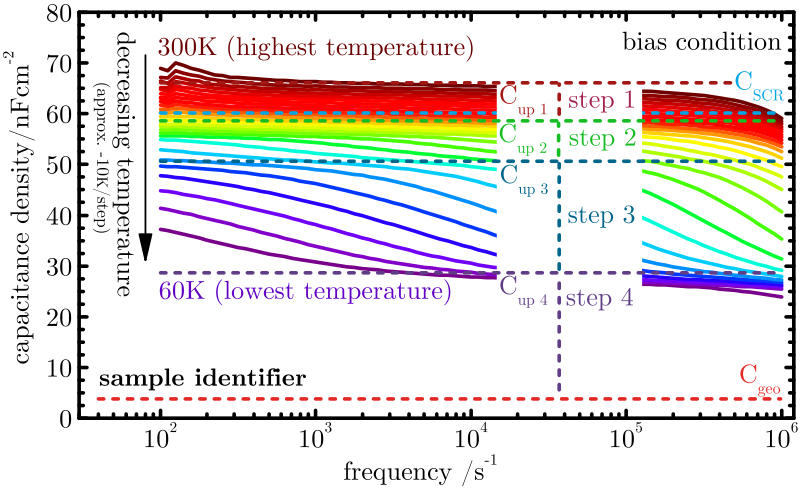

Figure 4.6.: ***Typical Cf spectrum*** *- Schematical admittance spectrum as measured by TAS, every capacitance spectrum shown within this thesis is plotted in the same way. The temperature decreases approximately by* 10 K *from one line to the next, only the low and high values are given (here* 300 K *and* 40 K*). The four different capacitance responses are labelled 1 to 4, from high to low temperature. Different distinguished capacitance values are marked by dashed lines. In blue the space-charge region-capacitance calculated from the doping density as measured by CV and at the bottom the geometrical capacitance, under assumption of a fully depleted absorber. The dashed lines mark upper and lower values before and after each capacitance response.*

tailing. Increasing the measurement temperature might increase the attempt-to-escape frequency of this signal enough to shift it in the frequency range that can be measured, but this is not possible with the utilized setup.
Other electrical measurement techniques like modulated photocurrent [118] and photoinduced current transient spectroscopy [119] have been employed to measure defects with such high activation energies. And could also be employed to further study this distribution.
Only for the Cu-poor sample with high Se a few inflection points could be extracted as shown in figure A.9a. The Arrhenius plot here gives an energy of 413 meV, this defect might be related to the 'N2' trap level, previously reported for CIGS and CIS solar cells. It is not shown in the Meyer-Neldel representation in figure 4.7, but it lies in the general area of the drawn 'N2' line.

Similar problems as for step 1 arise for step 4, the signal at very low temperatures, as this capacitance drop, too, is at the edge of the frequency range and at most one or two inflection points can be measured. Furthermore, since this step is only visible at low temperatures the series resistance becomes an important influence on the capacitance spectrum. Indeed evaluation of IVT measurements in the same temperature region reveal a strong increase in R_S. The modelling of the capacitance contribution of this series resistance as described in section 2.3.4 (after equation 2.42) shows a response in the same frequency range as step 4, which suggests that this signal can be due to either of three effects; a barrier, carrier or mobility freeze-out. At least in some of the samples, most notably the low Cu/In and low Se sample, this signal seems to level out towards the geometrical capacitance, indicating to the most likely explanation of this response being

indeed the carrier freeze-out of the shallow doping defect.
The more pronounced signals step 2 and 3 can be evaluated more closely than the aforementioned responses. The first observation from the admittance-spectra is that both steps are below the capacitance of the space-charge region, therefore they are probably not due to deep defects. This however is not a hard criterion, since the measured doping density from CV measurements might still contain traps at high temperatures, if the forward bias is not enough to suppress them, see section 2.3.6.
The differentiation between shallow and deep defects involves its position with regard to the Fermi level. Therefore the next step is to evaluate the responses' activation energies, which can be via Arrhenius-plots, as described in section 2.3.3. Results for each series are shown in figures A.7 (high Cu/In), A.8 (low Cu/In) and A.9 (Cu-poor).
Step 2 (red dots) is usually only visible in a limited temperature range, while step 3 (blue) can be detected in a broad range. Unfortunately for a lot of samples there is a pronounced curvature of the latter's plot.
As described previously (see section 2.3.3) one explanation of a curved Arrhenius plot can be a mobility freeze-out due to variable-range hopping. The described method of choosing a $T^{-1/4}$ temperature dependence however does not yield a straight plot either. Testing different exponents also did not yield a totally straight line. In order to be able to compare to literature in which the T^{-2} dependency is prevalent, evaluation is still performed utilizing this prefactor. Consequently the linear fit has always been performed at high temperatures, therefore yielding an upper limit of the defects' activation energy.
For the Cu-rich samples, activation energies range from 200 meV to 250 meV for step 2 and 50 meV to 130 meV for step 3. For the Cu-poor-samples only a response around 110 meV was detected, consequently it seems to be associated with the lower energy response in Cu-rich and will hitherto be referred to as step 3.
Even though this evaluation method strictly only applies for deep defects, the Walter analysis was performed on all the samples in order to enable literature comparison and to have a metric to compare the different defects' densities and widths, since this information can not be extracted from the Arrhenius plot. Comparison between the activation energies of the two different methods shows that they agree reasonably well for step 2, but not as much for step 3, as is shown in table 4.3. Furthermore it is not possible to find a frequency for which the different temperature curves all align for step 3 and the graphs show some strong deviations towards higher defect densities at lower temperatures. This further implies, that indeed the measured signal is not a deep defect, but rather a freeze-out or barrier.
In any case, there does not seem to be a dependency of either values of activation energy, thermal pre-factor, density or width on the Se pressure during growth. And as usual for electrical measurements, there is a strong variation of measured defect energies and thermal pre-factor, which is probably not due to a high number of different defects. Rather this is explained by a reduction of the defect ionization energy, due to difference in defect concentrations and local electric field, which can be rather pronounced even for similar samples [120]. This in turn can lead to a possibly huge variation in attempt-to-escape frequencies due to the Meyer-Neldel law [73].
To show the underlying behaviour and group responses together as defects a Meyer-Neldel plot is shown in figure 4.7. Furthermore, literature lines corresponding to two previously reported signatures, dubbed 'N1'(from [72]) and 'N2'(from [41]) have been added to the plot, to show correspondences. For the Cu-rich samples both defect signatures form two distinguished groups, with step 3 of the Cu-poor samples closely below step 3 of the Cu-

rich ones. The 'N1'-line crosses step 3 for the Cu-poor samples and step 2 for the Cu-rich. In their work from 2013, Krysztopa *et al.* [41] gathered studies of electrical measurements on different CIGS materials, including polycrystalline Cu-poor and Cu-rich CIS, the same material that is the subject of this thesis.
They state, that the two lines can stem from a multitude of effects which have been grouped into two signatures. This might also be the case in the present measurements. It seems likely that the Cu-poor response step 3 is related to some of the effects, which in the literature are described as 'N1' defect.
The question here is how this relates to the two steps (2 & 3) measured in the Cu-rich cells. Treating these as separate responses by fitting a Meyer-Neldel line through all the defect energies from step 2 and another one through all from those of step 3, results in the lines being parallel.
This indicates that the nature of the underlying activation process is the same and that the defects themselves are not, as discussed in section 2.3.5. Indeed, there should not be any reason, why the same defect appears at two different activation energies within the same measurement. But since the aforementioned similarity of activation processes it is probable that both signals are involving the same carrier type and phonon coupling.

In the following the previous chapter will be summarized and a conclusive picture of the electrical measurements on Cu-rich grown $CuInSe_2$ will be formed by adding up of the previous observations.
Starting with the findings for step 1, whose capacitance in most cases is clearly additional to C_{scr}. It is only visible in the admittance spectra at high temperatures and low frequencies and more pronounced in the Cu-poor samples. Only from the high Se, Cu-poor sample enough inflection points could be extracted to calculate an activation energy of about 400 meV. For the other samples there are some onsets of a step towards low frequencies, which indicates that in the other samples the activation energies are even higher than this. Either a deep and broad defect density or band tailing are the most probable cause for this capacitance drop.

The next signal, step 2, has a straight Arrhenius plot and extracted activation energies range between $200 - 250$ meV, which is close to the results from the Walter analysis. A barrier of this height is unlikely, as it would highly impede solar cell function, which is not reflected in the IV results. Both evaluation methods are founded on deep traps as the cause of the capacitance drop, their good agreement supports the conclusion that this is indeed the source of the signal step 2. However the low frequency capacitance C_{up} is very close but usually below the space-charge region capacitance, which points towards a barrier or shallow defect. But this is only a "soft" criterion, since the capacitance-voltage measurements were performed at room temperature and are themselves influenced by deep traps, therefore the value of C_{scr} might be already too high. Furthermore the step starts appearing only at low temperatures below 180 K. Depending on the position of the Fermi level, a defect can be shallow at high temperatures, but deep at reduced temperatures. Therefore the simplest explanation for step 2 is indeed a deep defect native to the Cu-rich material as it is not found in the Cu-poor samples. The question if this is a bulk or interface state remains at this point. Both are possible, since no shift in activation energy has been observed for externally biased admittance measurements. An interface defect however is less likely, due to the prerequisite of having to assume a pinning of the Fermi level.

The best explanation for step 3 in the Cu-rich samples is a carrier freeze-out, because

it lies below the space-charge region capacitance, it has a curved Arrhenius plot and its DOS also seems to shift. However the Arrhenius plot is curved, evaluation at the high temperature side yields activation energy between $50 - 130$ meV. Looking at the results from PL measurements on CIS with different compositions [40, 121], a number of shallow defects are found. The cited references find three acceptor states, 'A1' for near stoichiometry samples at 40 meV, 'A2' for more Cu-rich at 60 meV, 'A3' at 100 meV which appears in both. Photoluminescence measurements on the absorbers from the same process as those presented here (see reference [109]) show the donor-acceptor transitions 'DA2' & 'DA3' but not 'DA1'. All the Cu-rich samples are characterized by a rather high Cu-excess, therefore it is no surprise, that this defect transition is not observed.
Since we are dealing with probably two shallow acceptors that are close to the measured defect energy, the curvature of the plot that persists even after choosing the adequate temperature dependence, is best explained by the subsequent freezing-out of these two doping defects. Therefore we can conclude that the third signal is the carrier-freeze-out of 'A2', directly followed, by that of 'A3'.
The same arguments apply for the Cu-poor material, with the exception, that due to their high compensation, no distinguished DA transitions are reported. Most probably step 3 in those samples is also a carrier freeze-out of multiple shallow defects, this also would account for the fact, that the Meyer-Neldel lines of step 3 in Cu-rich and Cu-poor samples are parallel, since they both originate from the same process. The shift upwards is then possibly due to an enhancement of the emission rate due to an increased electric field, produced by the systematically higher doping of Cu-rich material [122].

The capacitance does not go down to C_{geo} in all the samples and in some a rather pronounced gap remains when step 3 is levelling off. This gap has been labelled as step 4, whose inflection points are not fully resolved, because the critical frequency lies above 1 MHz throughout the temperature range of the measurement. As described previously in section 2.3.3 after the carriers have frozen out, they can still be mobile through variable range hopping and by this contribute to the capacitance. Due to this, while decreasing the temperature further below the carrier freeze-out, there will be another step, when all mobility becomes suppressed. This mobility freeze-out might be more or less pronounced depending on the defect densities and their spatial distribution within the samples. Step 4 can therefore be attributed to a mobility freeze-out, however it is not possible to test for this, since this would require measurement of the temperature dependence of the critical frequencies in step 4.

Table 4.3.: *Defect parameters for the two capacitance responses in admittance measurements*

Cu/In	Se	Arrhenius plot		Walter Analysis				
		E_A	ξ_0	E_A	ξ_0	N_t	w_{FWHM}	C_{up}
		meV	$s^{-1}K^{-2}$	meV	$s^{-1}K^{-2}$	cm^{-3}	meV	$nFcm^{-2}$
high	low	253	$1.6 \cdot 10^9$	246	$2.0 \cdot 10^9$	$4.8 \cdot 10^{15}$	40	43
		128	$1.2 \cdot 10^6$	116	$8.0 \cdot 10^5$	$7.9 \cdot 10^{15}$	40	32
	mid	252	$7.0 \cdot 10^8$	247	$1.0 \cdot 10^9$	$3.8 \cdot 10^{15}$	32	56
		81	$9.9 \cdot 10^4$	78	$1.3 \cdot 10^5$	$1.7 \cdot 10^{16}$	26	46
	high	200	$2.6 \cdot 10^7$	207	$1.0 \cdot 10^8$	$3.8 \cdot 10^{15}$	38	60
		101	$4.8 \cdot 10^5$	58	$1.0 \cdot 10^4$	$2.7 \cdot 10^{16}$	34	51
low	low	201	$3.7 \cdot 10^7$	192	$4.0 \cdot 10^7$	$4.4 \cdot 10^{15}$	39	39
		101	$5.4 \cdot 10^5$	80	$1.2 \cdot 10^5$	$1.1 \cdot 10^{16}$	38	30
	mid	209	$5.4 \cdot 10^7$	213	$1.4 \cdot 10^8$	$3.0 \cdot 10^{15}$	35	41
		75	$8.8 \cdot 10^4$	60	$4.0 \cdot 10^4$	$1.4 \cdot 10^{16}$	35	34
	high	216	$1.5 \cdot 10^8$	195	$4.0 \cdot 10^7$	$2.4 \cdot 10^{15}$	35	44
		54	$1.4 \cdot 10^4$	46	$1.0 \cdot 10^4$	$1.9 \cdot 10^{16}$	30	39
Cu-poor	low	97	$1.9 \cdot 10^4$	115	$1.7 \cdot 10^5$	$4.4 \cdot 10^{15}$	27	23
	mid	119	$5.5 \cdot 10^4$	110	$6.5 \cdot 10^4$	$4.3 \cdot 10^{15}$	45	23
	high	413	$1.9 \cdot 10^7$	414	$5.0 \cdot 10^7$	$7.1 \cdot 10^{14}$	163	>30
		122	$1.1 \cdot 10^5$	124	$2.5 \cdot 10^5$	$1.4 \cdot 10^{15}$	28	20

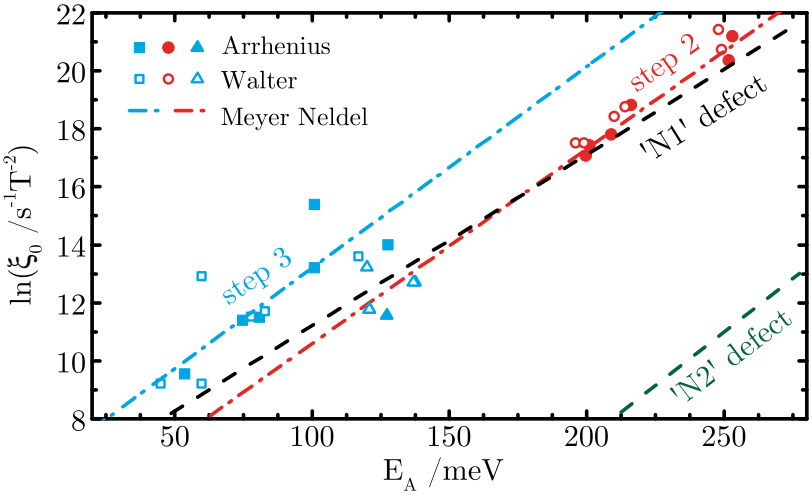

Figure 4.7.: ***Meyer-Neldel graph*** *- All measured defect energies of the three series together with added Meyer-Neldel lines for 'N1'(from [72]) and 'N2'(from [41]) from literature.*

CHAPTER

FIVE

INDIUM-SELENIUM SURFACE TREATMENT STUDY

From the previous investigations it is apparent that an important contribution to the lack in the performance of Cu-rich CIS solar cells originates from problems close to the absorber/buffer interface. Not all those impeding factors can be resolved by lowering the Se supply during growth. As shown in the previous chapter the lowered doping might contribute to a favourable reduction of the electric field at the interface, which manifests itself as an increased activation energy of the main recombination path of the V_{OC}. However the observation that the V_{OC} extrapolation still falls short of the bandgap value hints that some underlying cause of the high recombination rate at the interface is still present. As described in section 3.3 an In-Se surface treatment to form a Cu-poor surface layer on a Cu-rich bulk has been developed previously. The following chapter will showcase the result of utilizing this surface treatment on absorbers, which were grown under low Se. From this it is possible to take advantage of the superior Cu-poor CIS/CdS buffer-interface while keeping the excellent transport and absorption properties of low Se, Cu-rich CIS. Furthermore, the particular sample geometry that is achieved due to this type of surface treatment allows for additional insights into the defects of Cu-rich absorbers.

5.1. Influence of the In-Se surface treatment on device performance

Two series of In-Se surface treatments will be presented in this chapter, also an overview of sample identifiers and utilized treatments is shown in table 5.1. By the number at the beginning of each sample name the PVD process can be identified in which the bare Cu-rich absorber was grown. Some of the samples were treated first by depositing In-Se at lower temperature and then in-situ annealed under a Se overpressure. The letters and numbers after the process number indicate the subsequent treatment by its deposition and annealing times in minutes. For the first series all absorbers were grown within two days with the same growth parameters, therefore they should be very similar. The samples for the second series were grown much later, but also in close succession from one another and with very similar processes. Their untreated solar cells showed very similar properties. Therefore the treated samples in each series are very comparable, but the series with one another not as much.

Table 5.1.: *Overview of samples shown in this chapter, with their respective treatments. The temperatures are referring to the substrate temperature as measured by the PVDs pyrometer.*

	Sample Identifier	In-Se Deposition	Annealing
untreated	75u	-	-
	143u	-	-
	146u	-	-
treated	76D3	3 min at 275 °C	-
	76D1A5	1 min at 200 °C	5 min at 300 °C
	77D3A5	3 min at 200 °C	5 min at 300 °C
	77D3A15	3 min at 200 °C	15 min at 300 °C
	75D05bf	0.5 min at 275 °C	-
	143D1	1 min at 300 °C	-
	146D2A5	2 min at 200 °C	5 min at 300 °C

In the study of Se pressure during growth (see chapter4) indications that a high Cu-excess might be beneficial for solar cell performance were found. Therefore both series were supposed to be formed under this condition (Cu/In $>$ 1.7 before etching) and with low Se flux during growth. For the first series this was attempted by repeating the same PVD process multiple times in a row. These are the samples from process numbers 75 to 77. Processes 143 & 146 mark the second set of samples, they were not specifically made with surface treatments in mind, but taken from the stock. They were chosen because of their high QE yield and their composition and treated at a later time. All the measured samples were finished with the standard buffer/window/contact stack, with the exception of sample 75D05bf, which was finished without CdS buffer layer, hence the addition of 'bf' to the sample name for 'buffer-free'.
Current-voltage measurements show (see table 5.2 and figure 5.1a), that the untreated

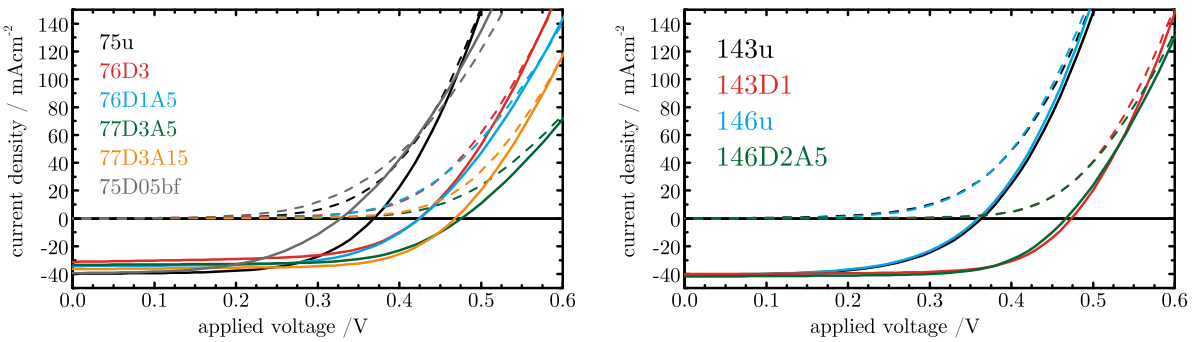

Figure 5.1.: ***Results of the IV measurements on InSe treated devices*** *- a) For the first and b) second treatments on Cu-rich absorbers grown under a low Se flux. The dashed lines are the IV curves recorded in the dark and the solid lines under illumination.*

reference sample (75u) exhibits a relatively high current and voltage leading to a decent efficiency of 8.8%. Unfortunately there is a strong discrepancy to the results of the QE

Table 5.2.: *Absorber performance as measured by IV at room temperature under A.M 1.5 illumination.*

Identifier	η	J_{SC} (IV)	J_{SC} (QE)	V_{OC}	$\mathcal{FF}$	A	R_S	R_{Sh}	J_0
	%	$mA \cdot cm^{-2}$	$mA \cdot cm^{-2}$	mV	%		Ω	Ω	$mA \cdot cm^{-2}$
75u	8.8	39.8	34.7	369	60.1	1.8	0.3	595	$9.6 \cdot 10^{-6}$
76D3	8.0	31.1	29.7	424	60.8	1.7	0.5	227	$1.2 \cdot 10^{-6}$
76D1A5	9.1	34.1	33.9	425	62.6	1.8	0.7	1059	$1.9 \cdot 10^{-6}$
77D3A5	10.2	33.4	32.6	476	64.4	1.6	1.1	855	$1.7 \cdot 10^{-7}$
77D3A15	11.3	36.2	32.6	468	66.8	1.6	0.6	769	$2.6 \cdot 10^{-7}$
75D05bf	6.7	39.2	40.2	328	52.2	2.2	0.5	2703	$6.1 \cdot 10^{-5}$
143u	8.3	41.1	39.3	363	55.4	2.1	0.3	236	$3.5 \cdot 10^{-5}$
146u	8.1	40.5	39.0	359	55.6	2.0	0.3	538	$2.9 \cdot 10^{-5}$
143D1	13.0	40.0	36.0	474	68.4	1.6	0.4	909	$2.9 \cdot 10^{-7}$
146D2A5	13.5	42.2	38.7	469	68.1	1.5	0.5	781	$1.3 \cdot 10^{-7}$
Cu-poor ref	13.5	39.7	41.1	488	70.0	1.4	0.6	5882	$3.6 \cdot 10^{-8}$

measurements, which reveal a rather poor collection of long wavelength photons. In principle a difference between the short-circuit current densities from IV and QE measurements can be explained by the different experimental setups (see chapter 2). The fact that the short-circuit current density in QE is calculated utilizing an AM 1.5 spectrum, but for IV measurements illumination is provided by a halogen lamp, already leads to some disparity. Furthermore, in the QE setup only a small circle of about 1 mm in diameter of the sample is illuminated during measurement, while in the IV setup the whole sample surface is excited. This is no concern for samples that are thoroughly homogeneous, but it might lead to discrepancies if the surface treatment leads to a formation of absorptive In_xSe patches of varying size and/or thickness. But despite these two errors, the incongruity in the present case seems rather large, possibly the calibration of the IV illumination had been off during the measurement. There is more room for error and external disturbance in the IV setup, the QE however is performed in a closed box and everything is controlled externally, which makes the results from this measurement more trustworthy.

As the main goal of the treatment is to reduce recombination close to the interface and thereby increasing V_{OC}, it is best performed on cells that already have a high J_{SC}. This should be the case for Cu-rich absorbers grown under low Se. However the first treatment series seems to have missed that goal, as the quantum efficiency of the untreated device is not as high as anticipated. It is likely that the Se flux during growth of series 75-77 was not sufficiently low and therefore the samples are too highly doped. This is confirmed by CV measurements and will be treated in the next section (see table 5.3).
Due to this, the treated devices do not show as high efficiencies as anticipated despite their high V_{OC}. The champion device (77D3A15) of the first series lies at 11.3%, mostly due to the voltage gain of about 100 mV. A reduction of recombination close to the interface can explain this improvement.
This is also in line with the results of the current-voltage measurements, fitting of the

room temperature curves with IVfit shows a reduction of diode quality factor and saturation current by the treatment (see table 5.2) and the temperature dependence of the open-circuit voltage extrapolates to the bandgap, as is shown in figure 5.4a. Even though the untreated absorbers were not the ideal samples to yield high efficiency devices, there is still a lot to be learned from these cells in order to improve further treatments. All treated samples except one (75D05bf) feature a reasonable improvement with regard to V_{OC}.
Quantum efficiency measurements show, that most deposition-annealing samples are char-

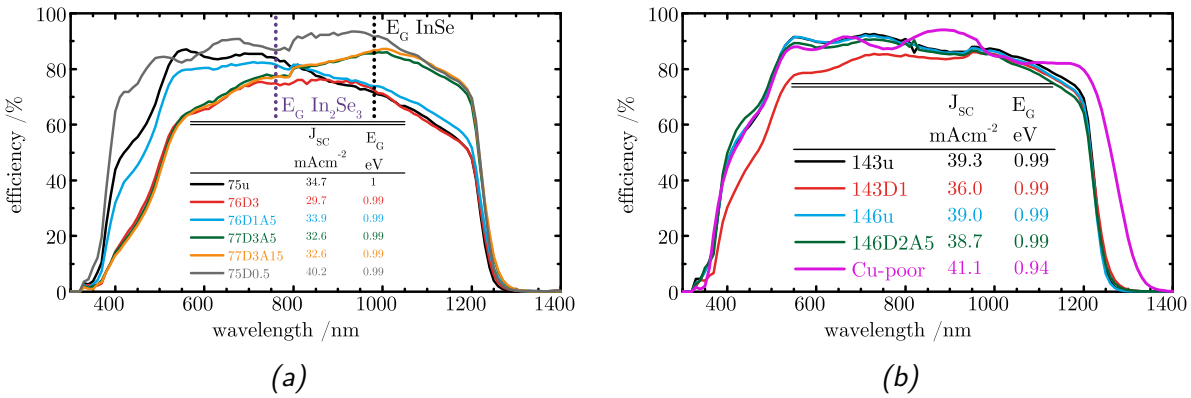

Figure 5.2.: ***Results of the QE measurements on InSe treated devices*** *- a) For the first and b) second treatments on Cu-rich absorbers grown under a low Se flux.*

acterized by an increased long and decreased short wavelength collection in comparison to the reference. Sample 75D05bf shows huge gain in QE over the whole spectrum compared to the reference. Overall the lowest quantum efficiency belongs to the long deposited sample (76D3) without annealing.

Looking into these features, with the specific treatments and sample characteristics in mind, already gives insight into what to consider for subsequent treatments. The observed differences in QE can rather easily be explained by a remaining layer or patches of In_xSe (InSe or In_2Se_3) on top of the absorbers, which absorb part of the incident photons.
Two features of the QE (see figure 5.2a) fit the respective bandgaps of the two modifications of In_xSe: the drop below about 1000 nm (visible for samples 77D3A5 & 77D3A15) fits the InSe bandgap(E_g = 1.26 eV, from [123]), while the reduction around 700 nm (visible especially for sample 76D1A5) fits to In_2Se_3(E_g = 1.68 eV, from [124]).
Auger electron spectroscopy (AES) measurements where performed on some of the samples to show that there is indeed a remainder of In_xSe on top of the treated absorbers. Results are shown in figure 5.3 for samples 75u and 77D3A15, the depth profile shows a clear influence of the treatment on the surface and also that after a certain depth the composition returns to stoichiometry. Taking the ratios of Cu/In and In/Se (5.3b) illustrates this more clearly, the In/Se value at the front might suggest that the prevalent phase in this sample is In_2Se_3, but there might be a mixture of different phases and the measurement is only limited to a small area of the sample, therefore this is not definitive. Previous studies [99] also find this phase in some samples. A possible explanation for the occurrence of the second phase (InSe) might be a lower Se supply during treatment. Samples 77D3A5 & 77D3A15 both had a long deposition phase with subsequent high temperature annealing and both exhibit a strong loss below 1000 nm. It is indicative that the formation of InSe was exacerbated by the long deposition in conjunction with possible

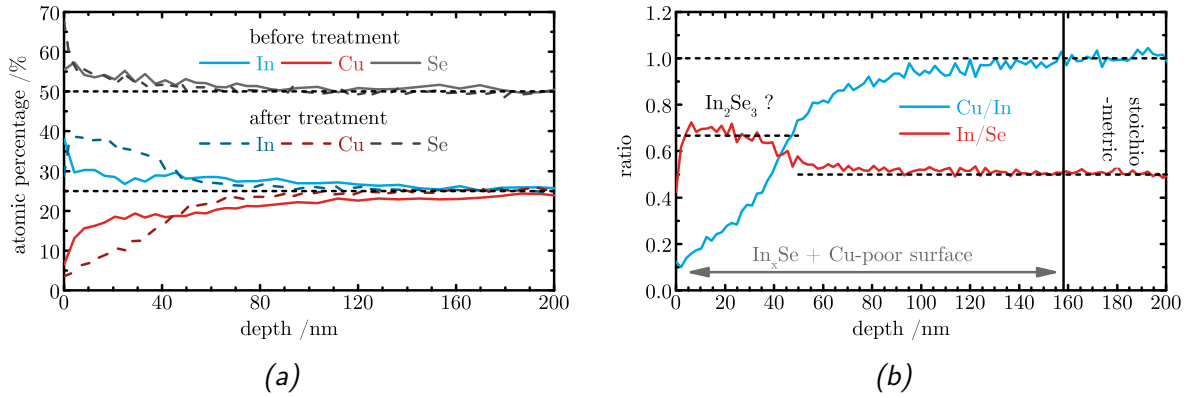

Figure 5.3.: ***AES measurements on a treated and an untreated sample.*** *- (a) Profile of untreated (75u) and treated (77D3A15) sample (b) ratios of treated sample 77D3A15.*

Se losses during the high temperature annealing.
For future treatments it is important to reduce both phases, but especially InSe should be avoided as its low bandgap results in losses over a wider part of the spectrum. To do so deposition time should be kept as short as possible, in order to prevent formation of a thick In_xSe layer.
Alternatively etching could be utilized in order to remove remaining In_xSe phases from the surface of the absorber. Therefore the complete picture for the deposition-annealed devices seems to show that the goal to form a Cu-poor surface was achieved, which increases the V_{OC} and even long wavelength collection, but they suffer from remainders of In_xSe overall decreasing their current. On the other hand the gain in long wavelength QE for the good two (77D3A5 & 77D3A15) deposition-annealing samples compared to the untreated one might be due to better collection of generated charge carriers.

The long deposited sample without annealing (76D3) also suffers from secondary phases at the top, but has the added disadvantage of a smaller increase in V_{OC} and a lower shunt resistance. This indicates that, while there might be a formation of a Cu-poor surface, its advantages are negated by a lot of In_xSe on the top due to long deposition time, but reduced Cu-diffusion on accord of the low deposition temperature.
The most peculiar sample seems to be 75D05bf, with a very short deposition time and without annealing step, which is characterized by a very high QE and therefore J_{SC} There is no remainder of In_xSe due to a short deposition and obviously a gain because there are no absorption losses in the CdS.
But the diode itself suffers of a high diode factor well above two, a low fill factor and ultimately a severely decreased voltage. This is explained by its special sample structure, namely the missing CdS buffer. As reported before the CdS buffer improves the device through increasing of depletion width and contact potential, also it protects against local shunts and sputter damage [97]. All factors together explain the lowered voltage and decreased shunt resistance of the device. This is also reflected in the activation energy of the main recombination pathway.
Not all devices could be characterized further, only three devices from the first treatment series and one from the second were chosen, additionally the untreated device from either series. It has to be mentioned, that the champion device was not further characterized, as it was selected to receive an anti-reflective coating and could not be contacted into the

admittance/IVT setup afterwards. IVT measurements on the treated absorbers generally shows an increase of the V_{OC} extrapolation compared to the untreated devices, indicating that the dominant recombination shifts to the bulk. However the exception is the short treated device, which is still dominated by interface recombination (see figure 5.4a).

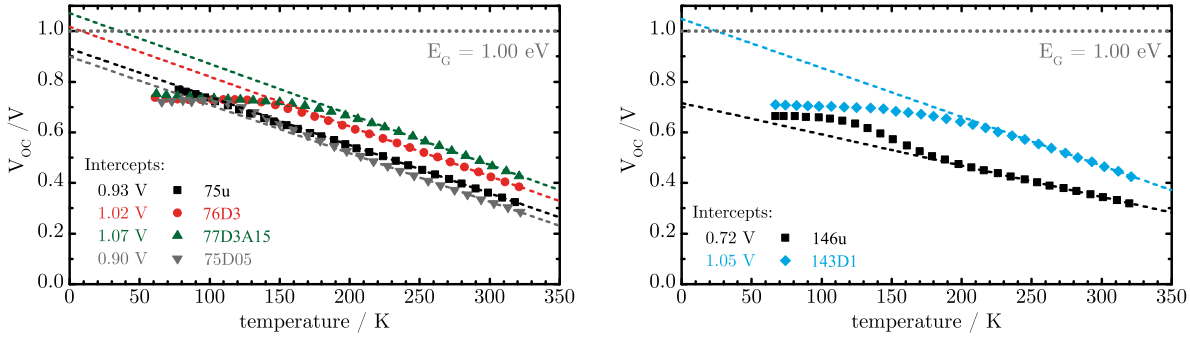

Figure 5.4.: ***Results of the V_{OC}-extrapolation on InSe treated devices*** *- a) For the first and b) second treatments on Cu-rich absorbers grown under a low Se flux.*

From the results of the two deposition-only devices a treatment at higher temperatures but shorter deposition time was derived and tested (sample 143D1), since it was deduced that already a short deposition is enough to form a Cu-poor surface, but higher temperatures might be necessary to improve Cu-diffusion. Due to problems with absorber deposition, it was unfortunately not possible to thoroughly investigate the influence of the Se flux on the In-Se surface treatment in the framework of this thesis.

To be able to do further treatments and at least have some results on a truly low Se device with a high QE already before the treatment a few processes with remaining bare absorbers (143 & 146) were selected that showed favourable properties and could be utilized for two treatments. According to the previous findings one sample was treated with a deposition-annealing process (146D2A5), featuring a deposition time in between the previously studied ones and a short annealing, since the annealing time does not seem to play an important role above 5 min. Another one was treated via a process without annealing, but under higher temperatures to facilitate Cu-diffusion(143D1).

Care was taken to achieve a higher Se flux for these treatments in order to inhibit growth of InSe, given that In_2Se_3 is less detrimental to solar cell performance. Current-voltage measurements on these devices are shown in figure 5.1b and their results summarized together with the rest of the treated samples in table 5.2. Again the increase in V_{OC} is about 100 mV after treatment and a sizeable gain in fill factor leads to an overall efficiency increase of more than 5%.
The deposition-annealing device shows a very good overall QE yield, but the deposition-only device shows losses in the short wavelengths, probably again due to formation of InSe. For the champion device there seems to be a small loss below 800 nm, which might be due to patches of In_2Se_3. But diode quality, fill factors, saturation current and ultimately V_{OC} are all very good. For comparison a Cu-poor device from our lab with the highest published efficiency is shown [100]. Efficiency-wise the champion treated Cu-rich device is on-par with this.

5.2. Influence on doping

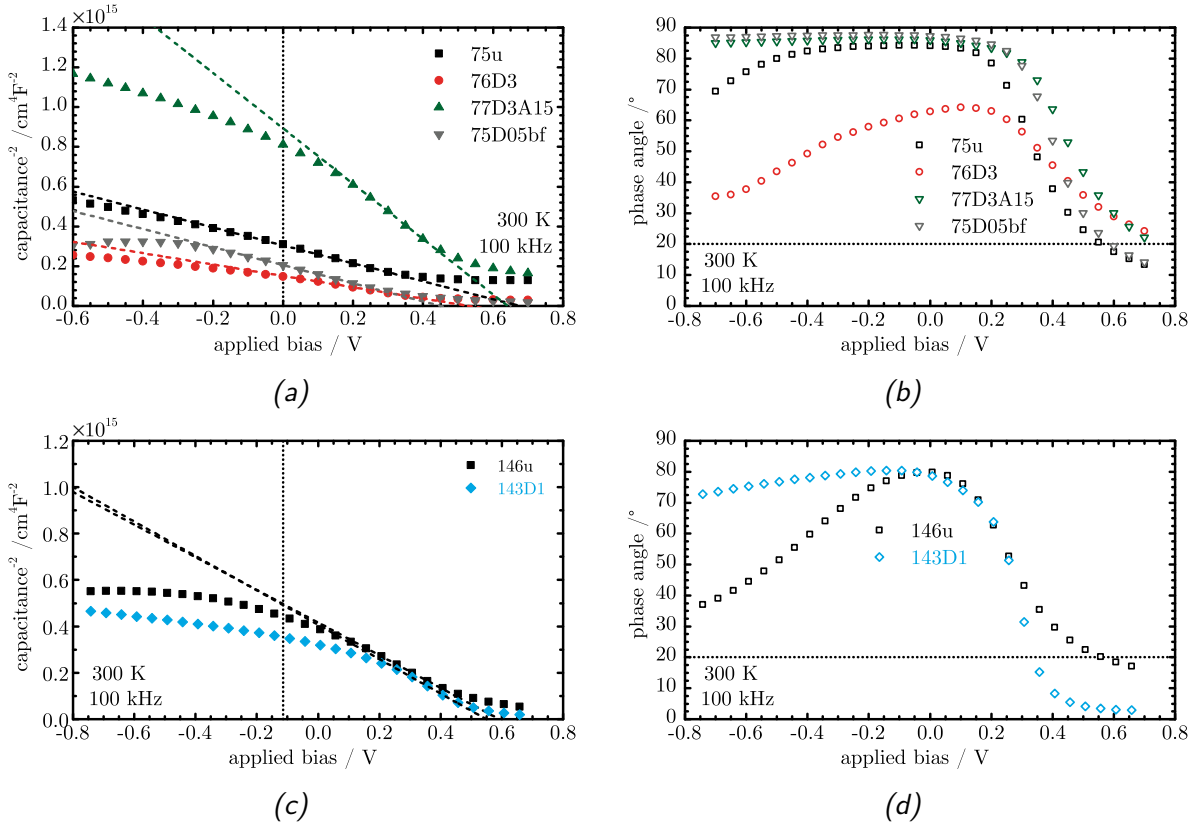

Figure 5.5.: ***Results of the CV measurements on InSe treated device*** *- These are the Mott-Schottky plots for the for a) new and c) old treated absorbers at room temperature and under* 10^6 *Hz. the left column shows the respective phase angles for eacht measurement.*

Capacitance-voltage measurements have been performed on a selection of the previously presented devices, the results are shown in figure 5.5 and summarized in table 5.3. The first series shows a mixed influence of the treatments on N_{CV}. As mentioned before the reference device is not as lowly doped as anticipated and it has a similar carrier density and built-in voltage as the devices with a high Se during growth.
The long deposition device without annealing shows a slight increase of the doping density and also a reduced built-in voltage. Probably this does not have anything to do with the treatment itself, but rather there was a slightly higher Se supply during process 76 compared to 75, which resulted in that increase. The treatment then resulted in a remainder of In_xSe at the interface, which leads to a poorer junction quality, reducing V_{bi}. This is also confirmed by its low shunt resistance.
For the device without CdS buffer there is no significant change in N_{CV}.
The best device (77D3A15) is also characterized by a decrease in doping density.
The devices for the second round of treatments were already characterized by a low doping density, they show characteristic values of a low Se absorber. The investigated treated device yielded good results without a change in overall doping density, due to the fact that it already started out low.

Table 5.3.: *Absorber parameters as extracted from capacitance-voltage measurements*

Identifier	N_{CV}	V_{bi}	x_{SCR}	C_{scr}
	cm^{-3}	V	nm	$nF \cdot cm^{-2}$
75u	$2.7 \cdot 10^{16}$	0.7	181	57
76D3	$4.2 \cdot 10^{16}$	0.5	127	81
77D3A15	$8.7 \cdot 10^{15}$	0.6	310	33
75D05	$2.7 \cdot 10^{16}$	0.5	148	70
146u	$1.7 \cdot 10^{16}$	0.6	211	49
143D1	$1.6 \cdot 10^{16}$	0.5	209	50

5.3. Defects in treated devices

Some of the samples were chosen to be further investigated by TAS measurements. Figures are shown in the appendix, A.15 shows the admittance-spectra of four samples from the first series and figure A.16 those of the chosen two from the second series.
The reference sample from the first series (75u) and the short treated sample (75D05bf) both show the four signals that have been previously discussed (see chapter 4) for the Cu-rich samples. The findings from the previous chapter generally apply to these samples, only discrepancies from the established picture will be discussed explicitly. Also the nomenclature as set there will be kept throughout this section. The high temperature signal (step 1), attributed to a very broad and deep defect distribution or band tails in the previous chapter, is very pronounced in these two particular samples. Especially for sample 75D05bf the space-charge region capacitance lies directly in this step, which might indicate that the measured value is too high due to this signal contributing to the measurement. Therefore it is probable, that the doping density of this sample is overestimated. The defect-related signal (step 2) and the carrier freeze-out (step 3) are both also visible in both samples, and evaluation of their activation energies are in the same range as measured for typical Cu-rich samples, see tables 5.4 and 4.3. The low temperature signature (step 4) is not directly visible, but the difference to the geometrical capacitance below the high frequency capacitance of step 3 leaves room for a mobility freeze-out.

On the other hand, the reference sample of the second series (146u) is somewhat atypical. The first feature that is prominent in the admittance spectra (see figure A.16a) is the noise at low frequencies, which seems to peak around 100 Hz, and disappears above 1 kHz. Most probably there were some minor issues with the contacting of the sample. Maybe the glue was not holding the wires perfectly in place and due to vibrations produced by the cryogenerator there were some differences of the conductivity of the sample. Once the measurement frequency exceeds this vibrations by an order of magnitude, they become negligible.

The second difference in this sample is that the whole spectrum is dominated by one step in the mid temperature range, instead of two narrower ones. From the temperature range, in which the signal appears and defect parameters extracted from the Arrhenius-plot, it is apparent that this step is related to step 2, the high temperature signal only found in the Cu-rich samples. This is at first counter-intuitive, since in any case there has

Table 5.4.: *Defect parameters for the admittance measurements of the two treated series*

Sample identifier	Arrhenius plot		Walter Analysis				
	E_A	ξ_0	E_A	ξ_0	N_t	w_{FWHM}	C_{up}
	meV	$s^{-1}K^{-2}$	meV	$s^{-1}K^{-2}$	cm^{-3}	meV	$nFcm^{-2}$
75u	205	$1.4 \cdot 10^8$	200	$2.0 \cdot 10^8$	$1.4 \cdot 10^{16}$	38	66
	97	$1.6 \cdot 10^6$	86	$8.0 \cdot 10^5$	$3.1 \cdot 10^{16}$	25	48
75D05bf	95	$1.1 \cdot 10^6$	94	$1.4 \cdot 10^6$	$2.2 \cdot 10^{16}$	39	38
76D3	102	$5.9 \cdot 10^4$	97	$9.0 \cdot 10^4$	$3.9 \cdot 10^{16}$	29	89
77D3A15	105	$5.3 \cdot 10^4$	92	$4.0 \cdot 10^4$	$8.2 \cdot 10^{15}$	31	38
146u	199	$1.3 \cdot 10^8$	187	$1.0 \cdot 10^8$	$1.8 \cdot 10^{16}$	61	45
143D1	145	$2.2 \cdot 10^5$	138	$3.0 \cdot 10^5$	$1.3 \cdot 10^{16}$	38	55

to be a carrier freeze-out, meaning for the present evaluation a signal related to step 3 has to be visible in the spectra, which was attributed to the doping defects, measured in PL. Otherwise this would imply that the shallow doping defects suddenly have vanished in this sample and the absorber is only doped by the 200 meV defect, which is highly unlikely.
The argument that those defects are still freezing out at lower temperatures, as there is still a gap below the high frequency capacitance of step 3 and C_{geo} is also implausible. The doping density is comparable to that of other samples, therefore the capacitance difference should also be of a similar value, which is not the case as it is much smaller. From the temperature and magnitude this gap probably stems from a mobility freeze-out, as observed for the other samples (step 4).
Taking those arguments into account, the likeliest explanation is that in the measurements step 2 & 3 are not separated and only the critical frequencies of the high energy are distinguishable. This is reflected in the measurement by the large width of this step. Comparing the points were each step in the different temperature curves settles on the high and low frequency capacitance limit it seems to extend nearly over the whole frequency range. For the other Cu-rich samples this usually happens within one order of magnitude in the log plot. Therefore the measured step is probably a double step and the inflection points of step 3 are hidden within the flank of step 2. In the spectra towards higher frequencies there is a very faint change of slope, but no inflection points can be found there to evaluate. From the Walter analysis (see 2.3.3, equation 2.39) also a very broad defect distribution is calculated, which supports this explanation.

All the remaining admittance spectra of the treated samples have in common that they only show one response in the low temperature range, not the double step structure as observed in the untreated ones. Step 1 is not very pronounced in either of the remaining samples, if there is a deep defect distribution or band tails in the samples their densities should be rather low. Step 4 is detected in all the samples as the gap between the bottom of the middle step and C_{geo}, which is also attributed to mobility freeze-out as previously.

To characterize the response in the middle defect energies are evaluated by the Arrhenius-

plot. They are all in the range of the low temperature and low energy response step 3, which is not surprising, since they also appear in that temperature range. Furthermore as mentioned before there should not be a huge difference in the doping defects of the samples and therefore it is to be expected that the carrier freeze-out appears here. The Walter analysis however seems to show a strong increase in peak height at lower temperatures, which makes it especially hard to find a suitable thermal pre-factor. Even when only focussing on the high temperature range, where the Arrhenius-plot is straighter this effect is still very pronounced. However the defect parameters that are of interest seem to be rather robust to that variation, with exception of the peak width. This is illustrated in figure 5.6, where three Gaussians were fitted at different temperatures. Overall peak position and defect density seem to be stable in the range where the Arrhenius evaluation was made. Because the peak narrows while it amplitude increases, overall area and therefore defect density is constant within the error of the fit. Therefore at least some estimate of these values can be taken from the Walter analysis and compared to the previously measured samples.

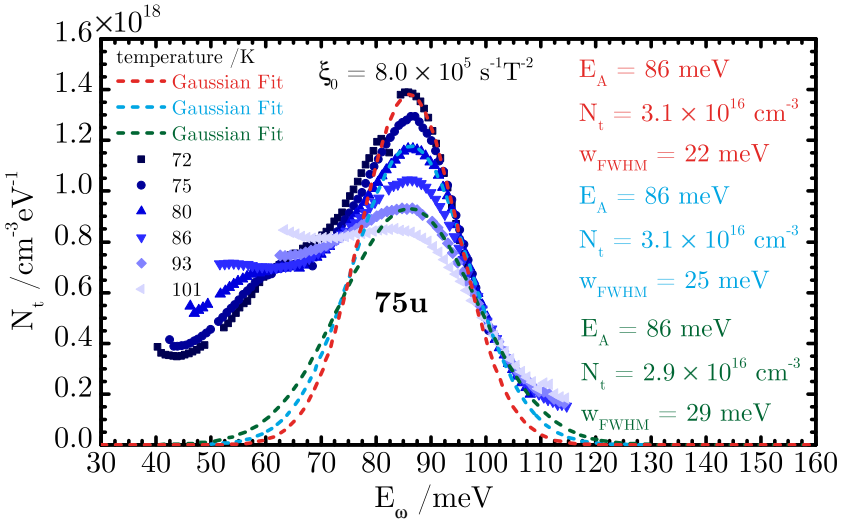

Figure 5.6.: ***Comparison of different Gaussians*** *- Walter method on a sample, that exhibits a shift towards higher defect densities with a decrease in temperature. The parameter that changes the most is w_{FWHM}, however the area under the curve N_t and peak position E_A are stable.*

In order to allow comparing the treated samples to the findings for the standard Cu-rich material, again a Meyer-Neldel plot was drawn (see figure 5.7). Additionally to the results of the last chapter the newly measured responses were added to the graph.
It is directly visible that all new responses fall on the same lines that have been found before. The untreated samples show the same two responses as the Cu-rich samples as expected, while the signal from the treated cells fall into the region of the carrier freeze-out of the doping defect as found in the Cu-poor absorbers. A behaviour that can be explained by the way admittance measurements work and the new sample structure. First, as stated previously, only defects that cross the Fermi level within the space-charge region width can be charged and uncharged and therefore contribute to the capacitance of the cell, also defects with higher activation energies are crossed closer to the interface with the buffer. Secondly, the treatment results in a Cu-poor surface that extends less than 150 nm (See figure 5.3) into the absorber. From the CV results it can be estimated that

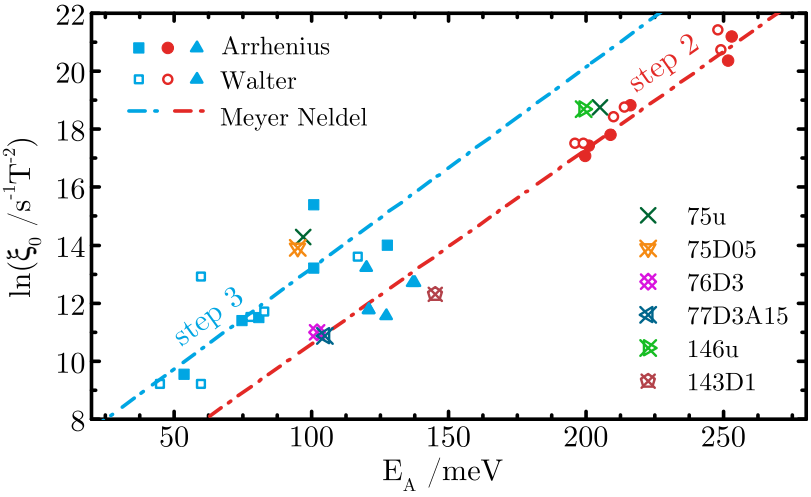

Figure 5.7.: ***Meyer-Neldel graph*** *- The results from the previous chapter together with the measured defect signatures in treated samples.*

the SCR is about $140 - 310$ nm wide. Therefore it is concluded that the measurements after treatment mainly probe the Cu-poor surface. This surface only has a slight Cu deficiency, comparable to the cells measured in the last chapter, as a result of its growth process. This explains why only the low energy response is measured and why it falls on the same line as in the Cu-poor samples and not on that of the Cu-rich ones. This explanation is illustrated in figure 5.8a.

Sample 75D05bf is the only exception here. In that case treatment was very short and therefore there is only a very thin Cu-poor layer on the top, therefore the low energy defect is still crossed within the Cu-rich bulk. Furthermore in the last chapter, the shift of the Meyer-Neldel line of step 3 was attributed to higher doping density in the Cu-rich absorbers, which increases the local field and thus enhances emission from the doping defects.

In principle this can be seen again in the treated cells. Sample 75D05bf has still the high doping of the Cu-rich bulk and its defect response falls on the Cu-rich MN line, the doping of the treated samples 77D3A15 and 143D1 is decreased and their responses is on the Cu-poor MN line.

However, the deposition-only sample 76D3 does not follow this trend, its doping is the same as the untreated sample, but still the defect response falls close to the Cu-poor MN line. Possibly due to the low built-in voltage of this cell (see section 5.2), the local electric field at the interface is small compared to the untreated absorber despite of the high doping. Therefore the trap is subjected to lower fields and emission is not enhanced as in the Cu-rich case.

An interesting result is that there is now more information on the nature of step 2, due to the special sample structure. In the last chapter it was concluded that step 2 is rather due to a defect, but it was not possible to exclude the possibility that a back contact barrier produces this signal. However, since a Cu-rich bulk is still present in the treated samples, the band alignment between absorber and back contact should still be the same. Therefore a barrier in the Cu-rich samples would still be present after treatment and it can be concluded that indeed the observed signal is due to a deep defect in the Cu-rich material.

It is unfortunately still not possible to distinguish between an interface and a bulk defect. Figure 5.8 shows a model of the possible measurement conditions, which would lead to a defect related signal, which is present in untreated absorbers, but disappears for treated ones.
Depicted on the left side (5.8a) is the situation for the untreated Cu-rich samples at two

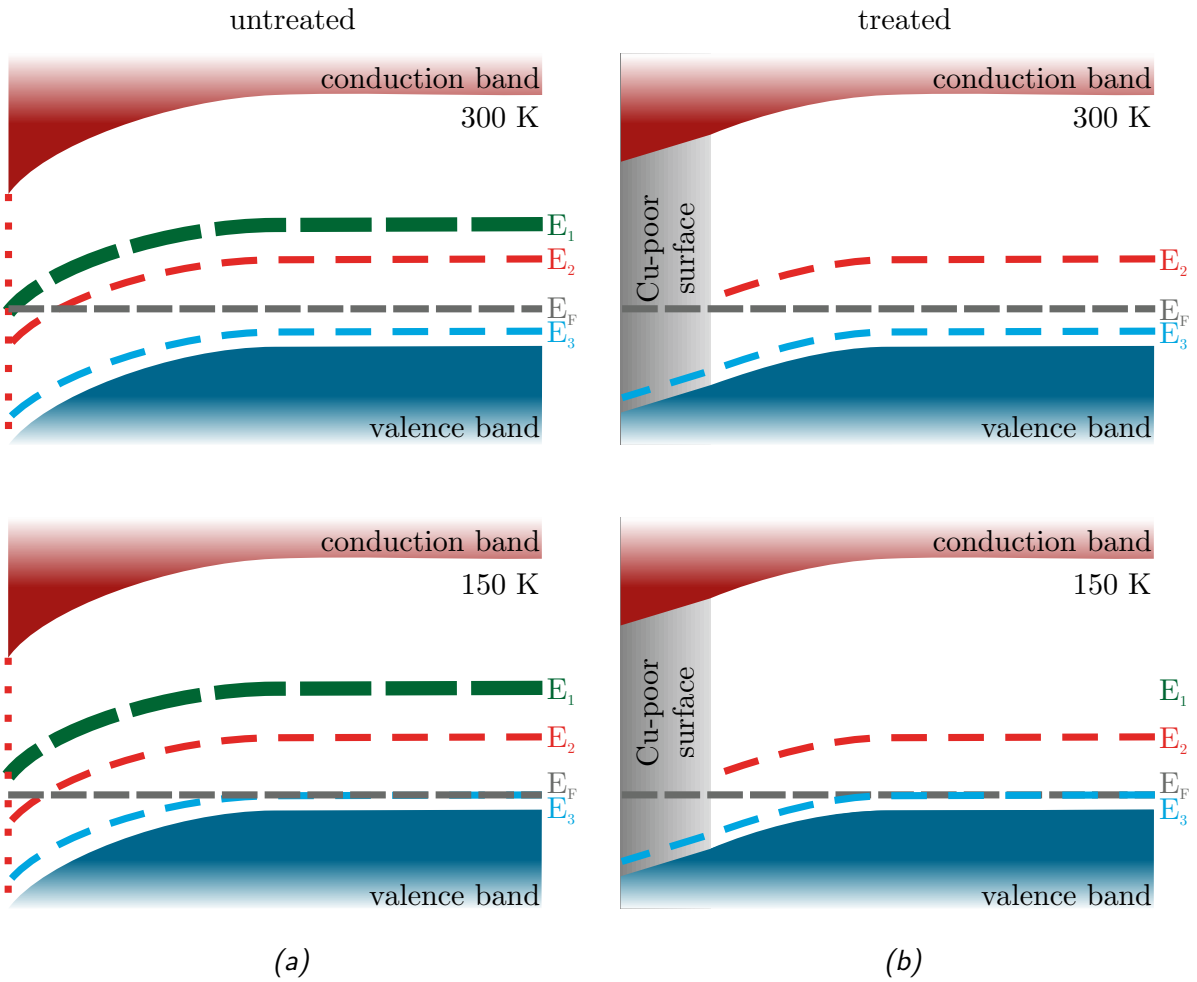

Figure 5.8.: ***Model for high energy defect in Cu-rich CIS*** *- Visual representation of the two possible defect locations of step 2 at different temperatures. a) for the untreated Cu-rich samples b) for the treated samples, featuring a lower doped, Cu-poor surface.*

different temperatures. The different energies are related to the various features of the Admittance spectra, 'E1' is related to step 1, a deep and broad defect distribution that is measured in some of the samples. It was not drawn in the picture of the treated samples on the right side, since for those cells it was usually not detectable (except for the short treated sample 75D05bf). The second step 'E2' is the defect response, which vanishes in the treated absorbers. And at the bottom 'E3' is a stand-in for the freeze-out of all the different doping defects possibly related to the signals 3 & 4. The dots at the interface in the left-hand graphs are representing interface defects, which are native to the Cu-rich/CdS junction and therefore are not present in the right-hand side. This would explain the vanishing of the signal, but biased admittance measurements contradict this explanation, since the signal does not shift with external bias. On the other hand, under the assumption of a pinned Fermi level an interface defect does not shift with bias, so one

might still be the cause of step 2.
But there is a second explanation that does not rely on other secondary prerequisites. Step 2 is depicted as 'E2' in the left hand graph, but it is not going through the whole absorber in the right side pictures and stops at the Cu-poor surface. If step 2 stems from a Cu-rich defect, naturally it would not be there in the Cu-poor part of the SCR. Even if the Cu-poor region does not extend over the whole SCR there might be no crossing of this defect in the remaining Cu-rich part, since deeper traps are crossed closer to the interface. Therefore it can be assumed, that step 2 is probably due to a bulk defect of the Cu-rich material.

To summarize the findings for the measured admittance responses, first there is a very deep and broad defect density or band tails in Cu-poor material, which is either less pronounced or even missing in Cu-rich solar cells. This might be an advantage for the latter, as very deep traps can act as strong recombination centres. Secondly a defect ('E2') in the Cu-rich bulk material was found, which is not present in Cu-poor. It seems to contribute to the high doping at room temperature, but a surface treatment removes this from the surface, where it might have detrimental effects. The remaining capacitance responses can then be attributed to carrier and mobility freeze-out.

Together with the results from the capacitance- and current-voltage measurements it is possible to comment on the mechanisms by which the treatments affect device efficiency. The increase in efficiency is mainly due to improvement of the open-circuit voltage, which also increases the fill factor.
From the QE measurements we know, that the current is mostly unaffected or even reduced due to remaining In_xSe. The treatment can reduce the effective doping, therefore decreasing the band-bending at the interface. Since absorbers grown under low Se were used during the treatment are already quite lowly doped, the additional reduction in effective doping does not change anything additionally.
This small change still might help to increase the V_{OC}, as there is a trend of higher gains for the samples with the lowest doping (see table 5.2 & 5.3). However this is not the only mechanism how the treatment influences the voltage, as not all treated samples show a decreased doping compared to the reference, but all have a higher V_{OC} nonetheless.
Alone the disappearance of the deep defect (step 2) already improves the voltage. It is probable that this defect acts as a recombination centre and reduces the open-circuit voltage. Since the diode quality factor of the treated devices also decreases, it is possible that this defect is promoting tunnelling recombination found in Cu-rich devices. The surface treatment moves it from close the interface to the bulk. This decreases the recombination rate on accord of the lower minority carrier density in the absorber bulk. This is also supported by the increase in activation energy of the domination recombination path. Without surface treatment, the activation energy is lowered, due to carriers tunnelling into the defect and recombining from there.

CHAPTER

SIX

SUMMARY AND OUTLOOK

This work was focussed on the electrical characterization of Cu-rich grown CIS solar cells, which is a very versatile material, whose unique properties make it worthwhile for PV applications. However it has some challenges, that can largely be attributed to a high doping and interface recombination, which impedes its performance in solar cell devices.

A study was presented here, addressing the effect of differing Se fluxes during growth of Cu-rich CIS. For this, three series of samples at different Cu/In ratios (above 1.7, 1.3-1.5 and slightly Cu-poor) have been produced, each with a sample of low, medium and high Se overpressure during growth. All series showed an improvement of solar cell parameters (determined by IV and EQE measurements) with less Se during growth and had a reproducibly increased short-circuit current. Also the open-circuit voltage increased with decreasing Se and its temperature extrapolation showed higher values at 0 K, which was however still less then the absorbers' respective bandgaps. This Se-dependent behaviour could be explained by CV measurements and attributed to a decrease of the free-carrier density N_{CV} with less Se flux, possibly due to a larger compensating effect of either increased concentration of the Cu-Se double vacancy or the In-on-Cu antisite defect, or both. Admittance measurements showed four responses in the Cu-rich and three in the Cu-poor series. Following their subsequent appearance while cooling down from room temperature, they have been labelled 1-4, with the second step being missing in the Cu-poor series. The first step is more pronounced in the Cu-poor series and has been attributed to either a very broad defect distribution close to midgap or bandtails. The second step has been attributed to a defect native to the Cu-rich either in the bulk material or at the interface. Step 3 is most probably the carrier freeze-out, maybe associated with two shallow defects that have been measured by PL at 60 meV and 100 meV. There is a difference of the Meyer-Neldel lines of the Cu-rich and Cu-poor samples, which has been explained by enhancement of the emission rate by the electric field due to the higher doping in the Cu-rich cells. The last step, if at all visible is probably caused by a mobility freeze-out at very low temperatures, but could not be resolved due to constraints of the measurement setup.
The second part of this thesis focussed on solar cells from Cu-rich grown, low Se overpressure CIS absorbers, which had been etched and subsequently coated with In and Se at elevated temperatures. This In-Se surface treatment resulted in the formation of a Cu-poor surface on top of a stoichiometric bulk, the structure has been confirmed by AES measurements. Depending on the treatment process a remaining layer of In_xSe caused

some absorption losses in the QE, but it could be shown that Cu-rich In-Se surface treated devices can be as good as Cu-poor ones. CV measurements found in some cases a reduction of the effective doping density, however this could not explain all the gains in open-circuit voltage. The activation energy of the main recombination path from IVT measurements showed that for most devices, interface recombination was now fully suppressed. Furthermore TAS measurements showed, that the deep defect (step 2) which was first discovered for the Cu-rich samples, is not appearing in the treated devices any more, even though measurable in the untreated reference. From this it was hypothesized that this defect acts as a recombination centre and is pushed out of the SCR and away from the interface, reducing its recombination rate due to the decreased minority carrier density in the bulk.

Where to proceed to from here?

These results show already a great improvement of the Cu-rich grown CIS material, especially a consistent high short-circuit current, by simply growing with a decreased Se overpressure. And with more optimization surely a surface treatment could be found suitable for these absorbers, which show the same increase in open-circuit voltage as found in previous works while still keeping the short-circuit current at the high level of the low Se grown absorbers. The problem of current loss due to In_xSe patches remaining on absorber is probably an optimization issue, but possible selective etching methods might be available, for example an aqueous solution of Na_2S has been tested and might be promising. A different approach might be applying the surface treatment to alternatively etched cells. Previous works from my colleagues on an etching by an aqueous bromine solution, resulted in highly efficient absorbers, which suffered from reflection losses due to the resulting highly specular surfaces [125]. A treatment on these could result in small grains of Cu-poor material growing on the absorber surface and ideally increase the surface roughness to alleviate this problem.
Furthermore the next step would be the transition of the findings for CIS to the quaternary CIGS alloy, which is not a trivial task, however first results from colleagues look promising and are about to be published [126].

APPENDIX

A

SUPPLEMENTARY FIGURES

A.1. Supplementary graphs from the Selenium Influence Study

A.1.1. IVT measurement results

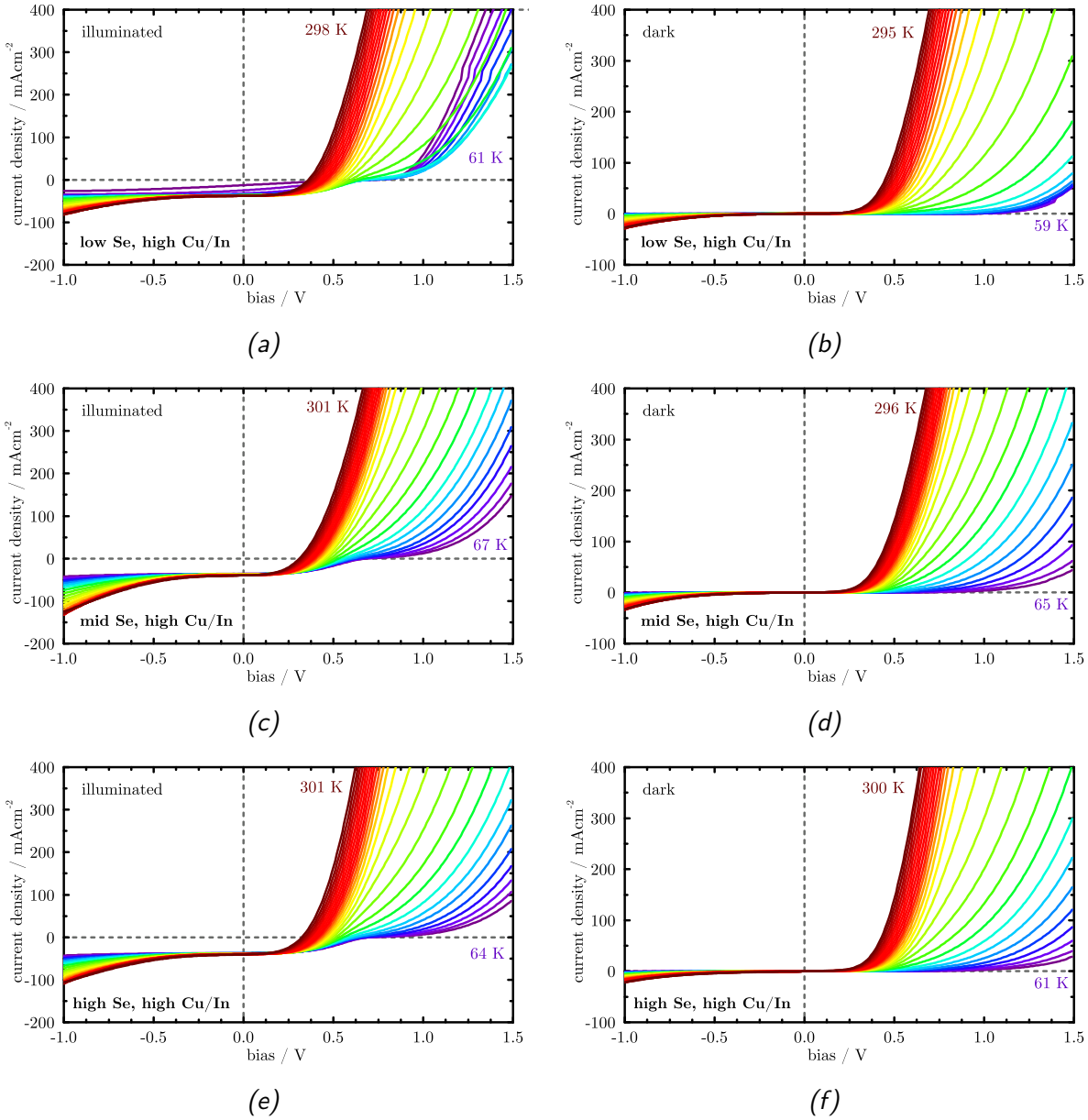

Figure A.1.: ***IVT Results of the high Cu/In ratio Se flux series*** *- a) & b) illuminated and dark curves of low Se sample, c) & d) illuminated and dark curves of mid Se sample, e) & f) illuminated and dark curves of high Se sample*

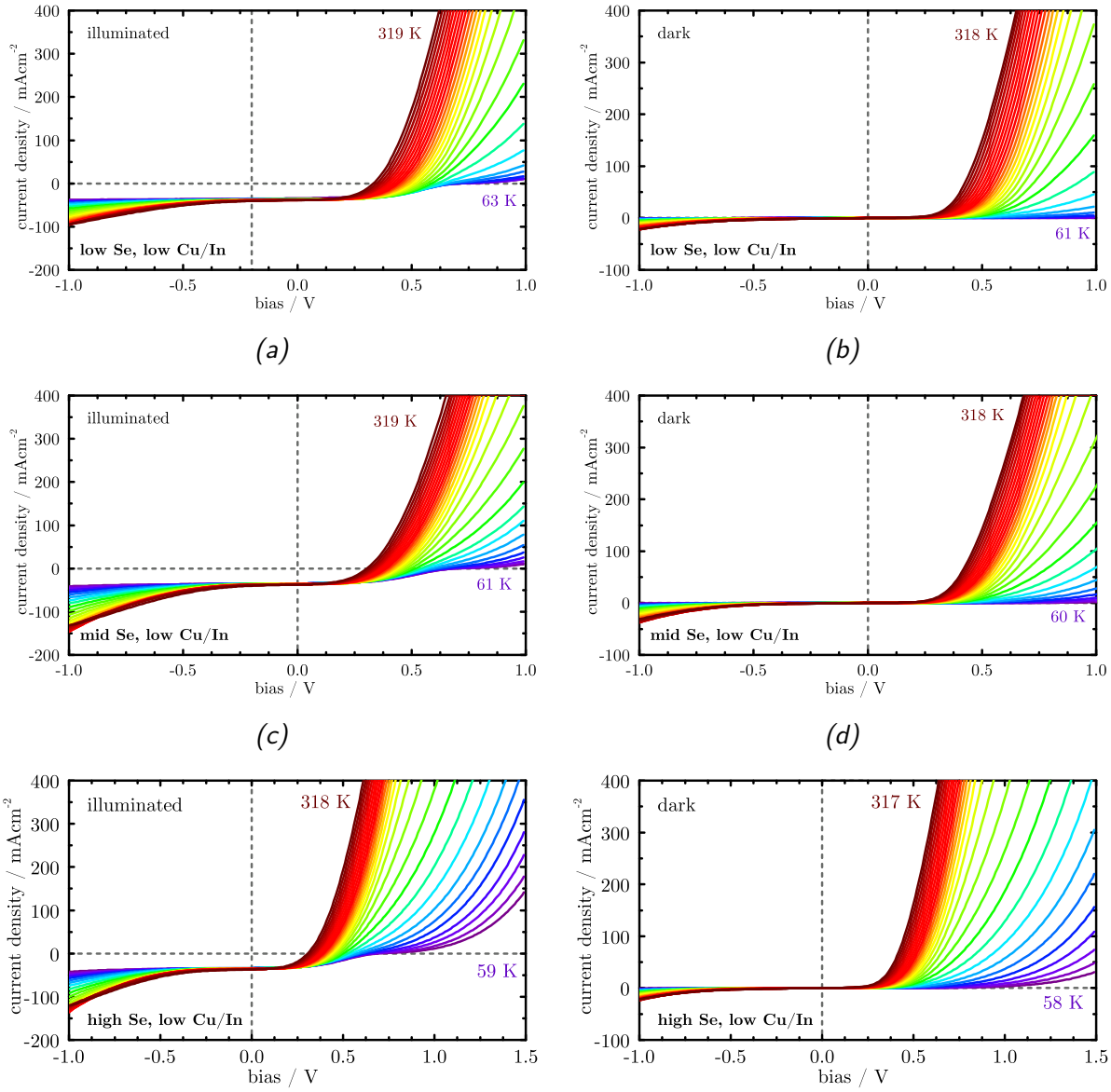

Figure A.2.: ***IVT Results of the low Cu/In ratio Se flux series*** *- a) & b) illuminated and dark curves of low Se sample, c) & d) illuminated and dark curves of mid Se sample, e) & f) illuminated and dark curves of high Se sample*

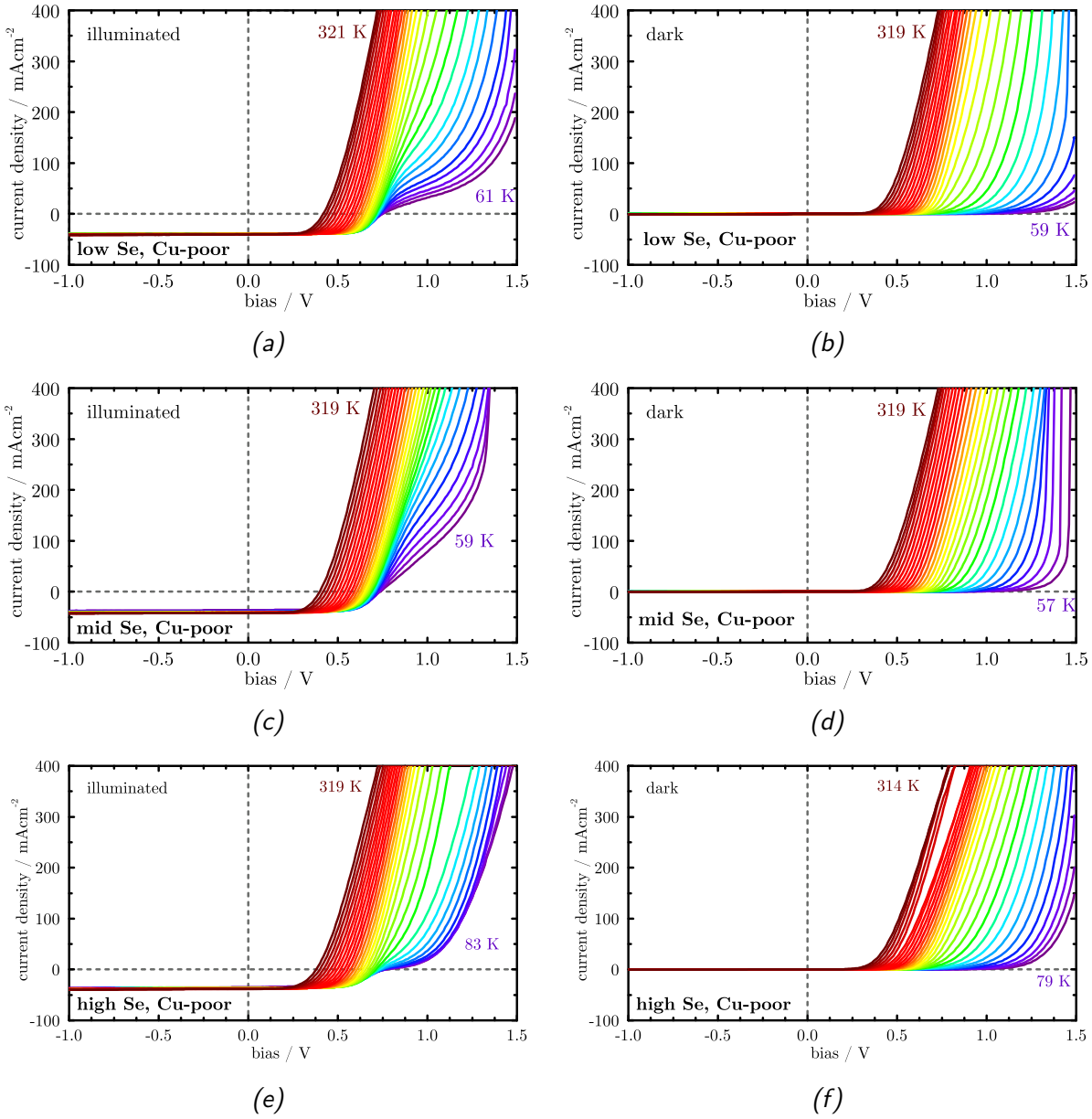

Figure A.3.: ***IVT Results of the Cu-poor Se flux series*** *- a) & b) illuminated and dark curves of low Se sample, c) & d) illuminated and dark curves of mid Se sample, e) & f) illuminated and dark curves of high Se sample*

A.1.2. Thermal admittance spectra

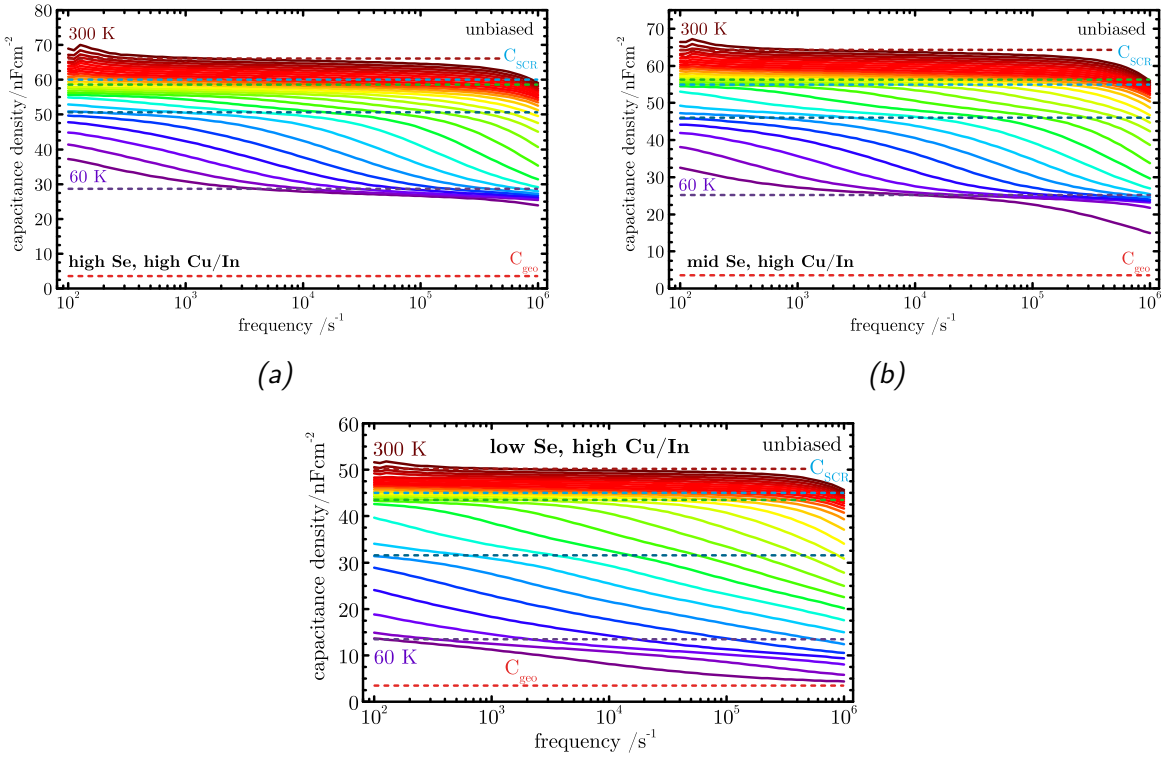

Figure A.4.: ***Results of the Cf measurements on the Se-series with a high Cu/In ratio.*** *- (a) high Se (b) mid Se (c) low Se.*

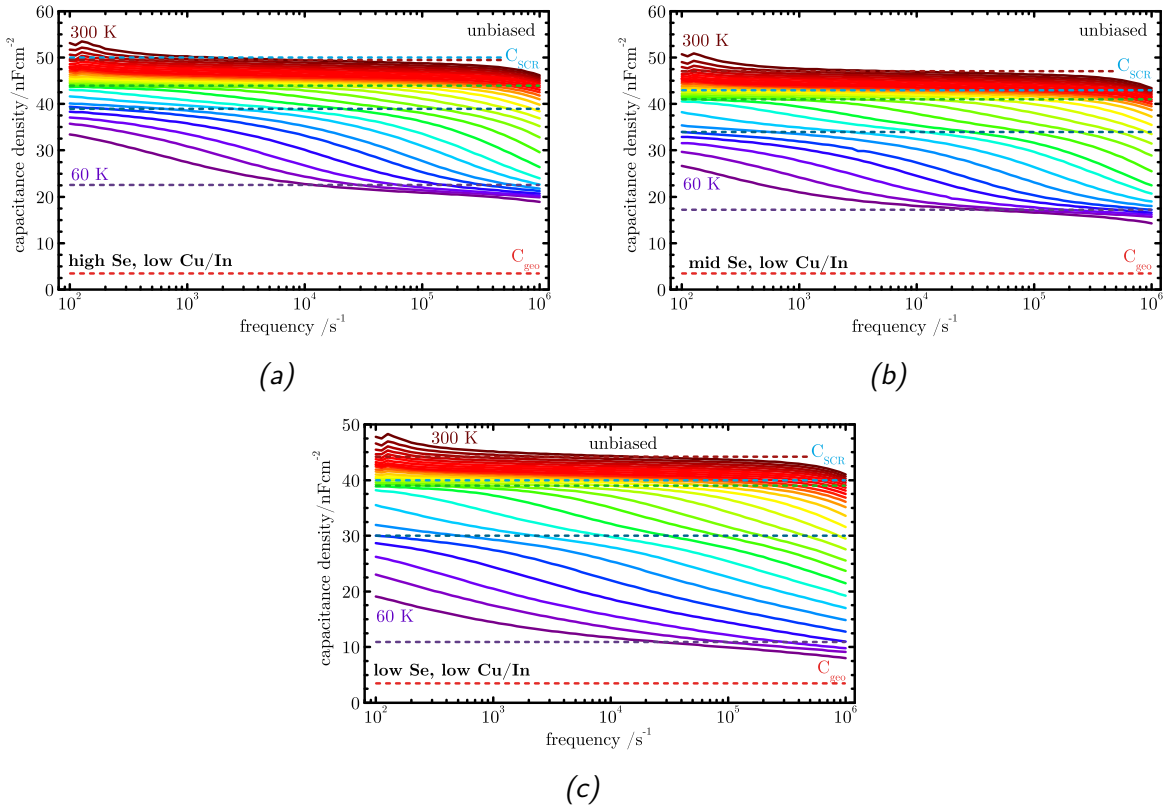

Figure A.5.: ***Results of the Cf measurements on the Se-series with a low Cu/In ratio.*** *- (a) high Se (b) mid Se (c) low Se.*

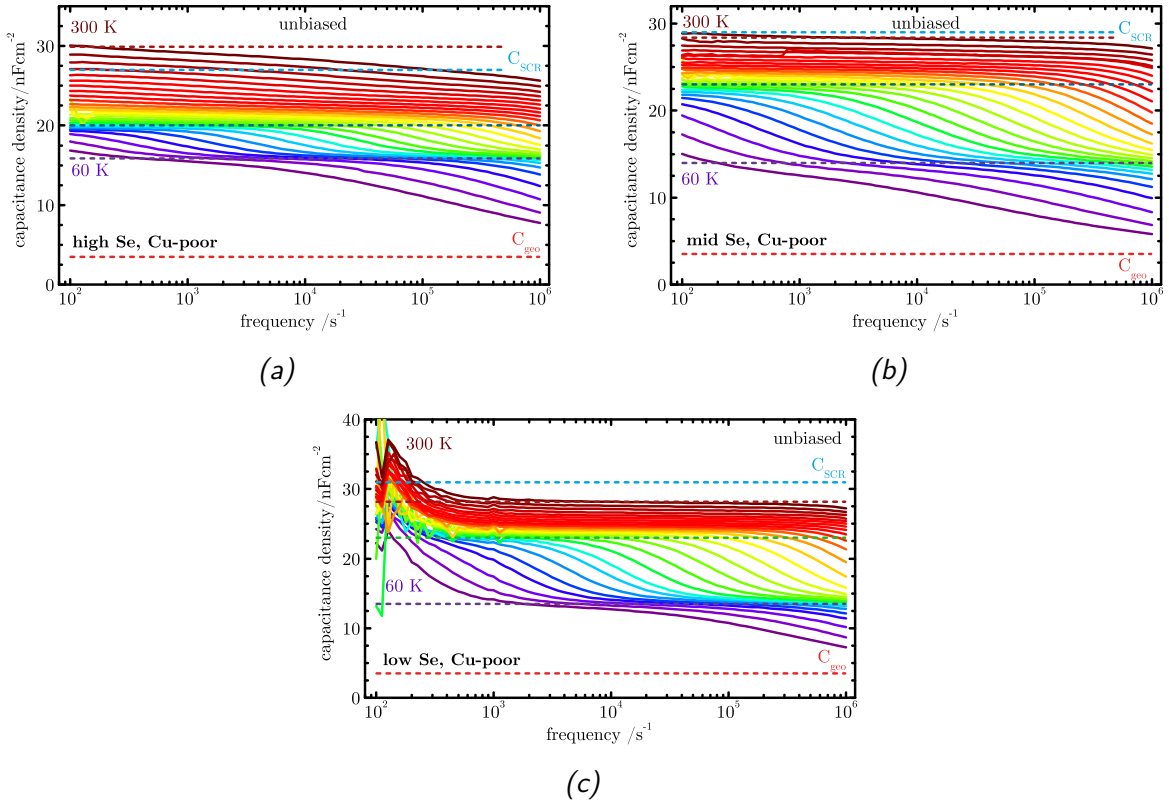

Figure A.6.: ***Results of the Cf measurements on the Cu-poor Se-series.*** *- (a) high Se (b) mid Se (c) low Se.*

A.1.3. Arrhenius analysis

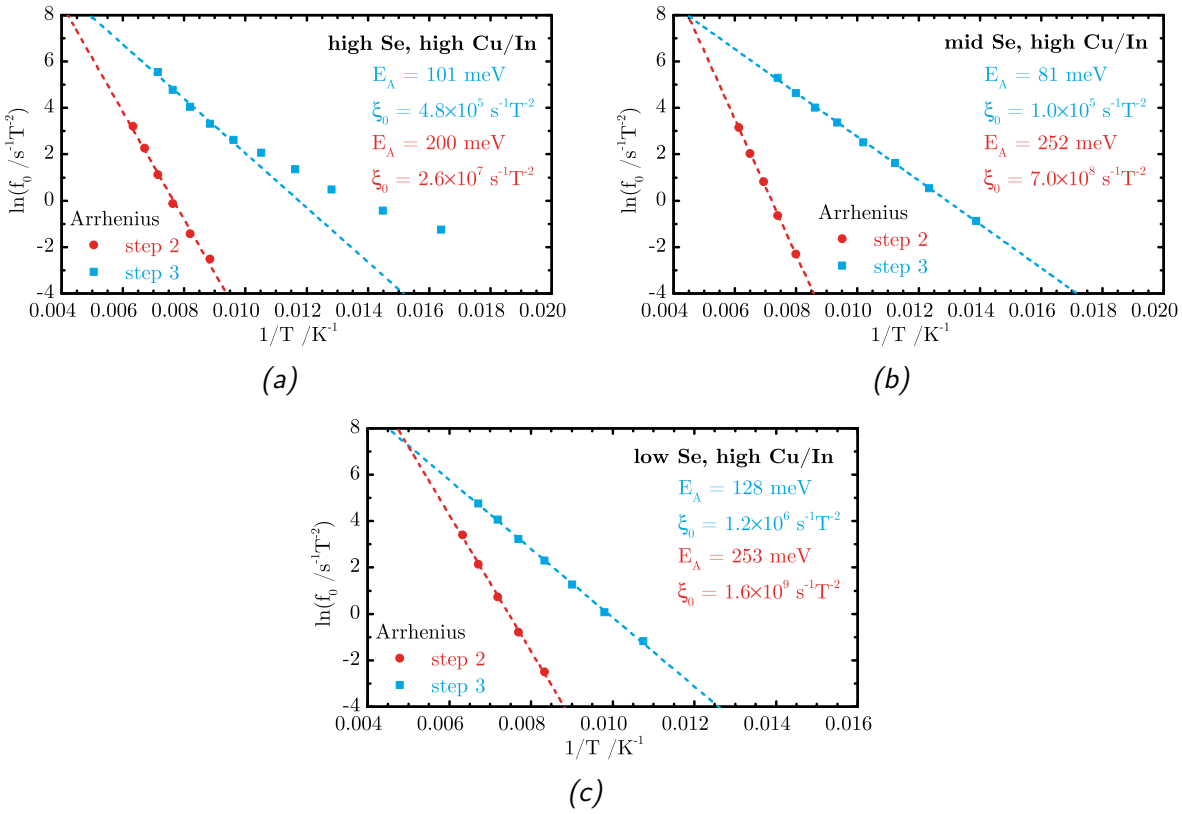

Figure A.7.: ***Arrhenius-plot of the Cf measurements on the Se-series with a high Cu/In ratio.*** *- (a) high Se (b) mid Se (c) low Se. Results of the evaluation from conductance and from the derivative of the capacitance.*

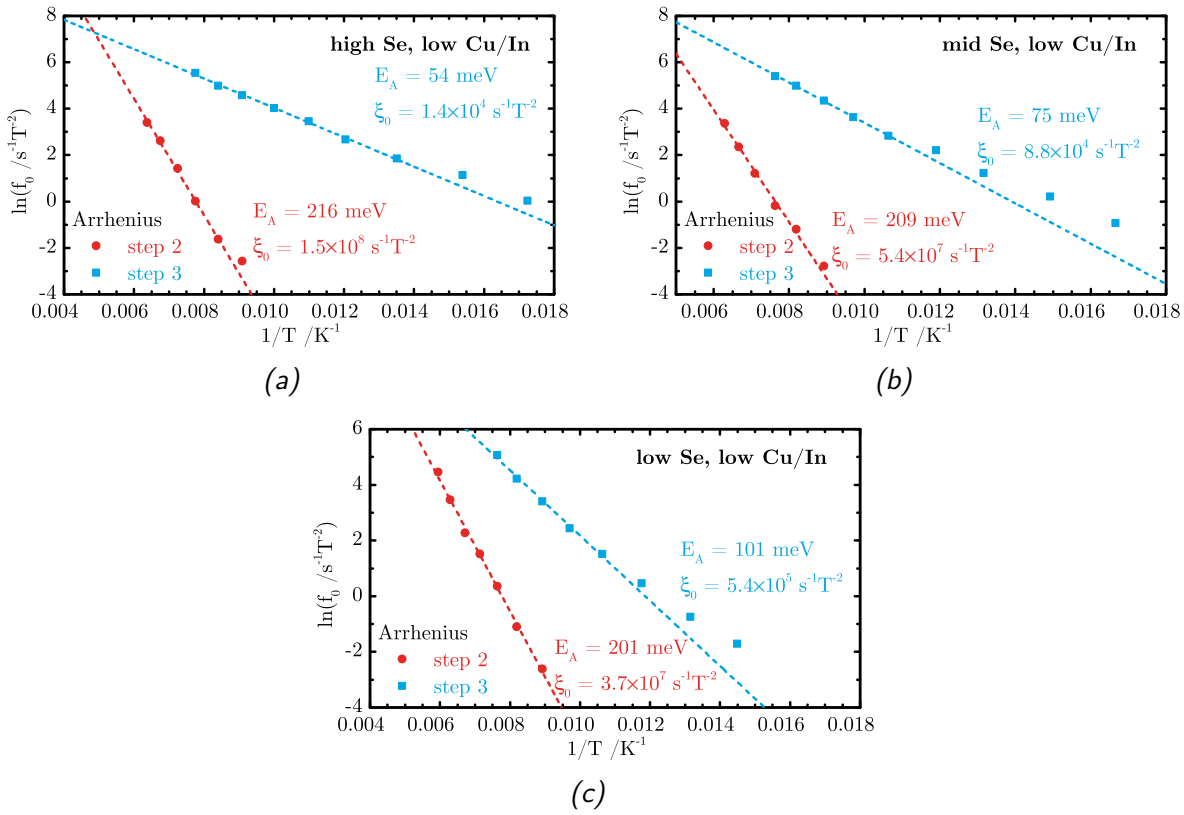

Figure A.8.: ***Arrhenius-plot of the Cf measurements on the Se-series with a low Cu/In ratio.*** *- (a) high Se (b) mid Se (c) low Se. Results of the evaluation from conductance and from the derivative of the capacitance.*

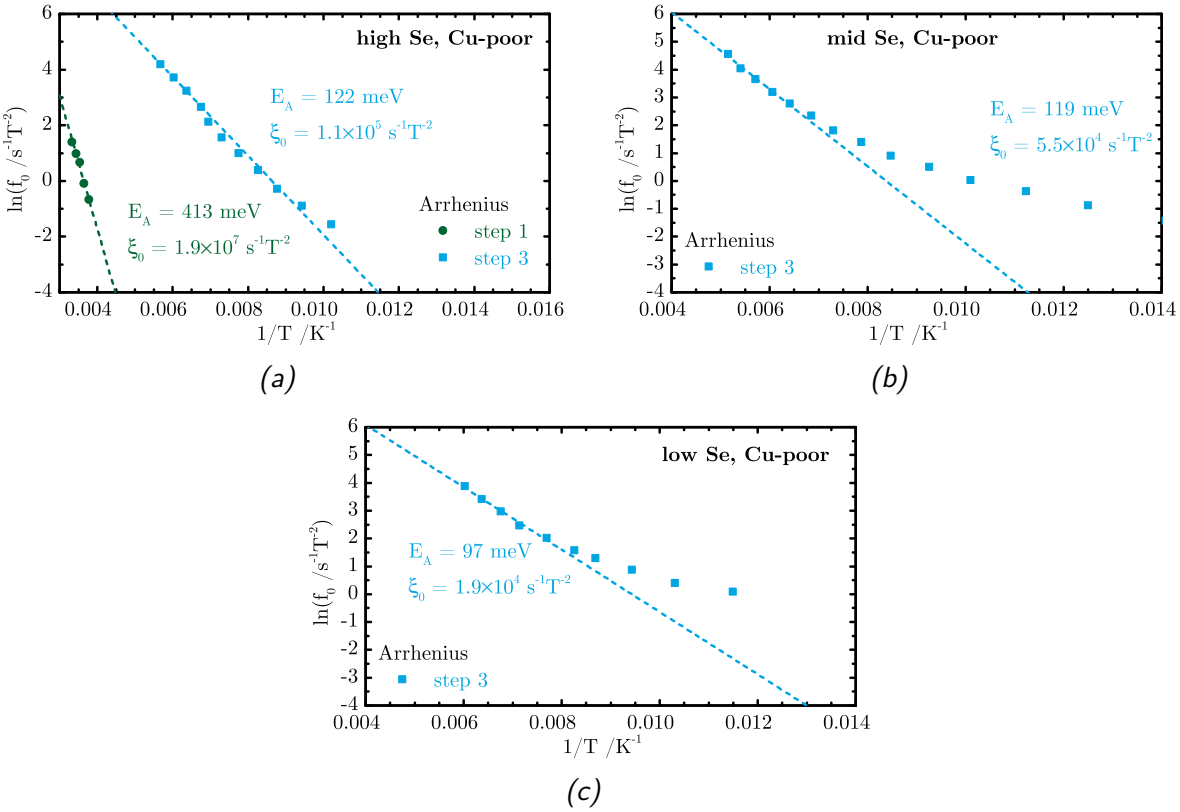

Figure A.9.: ***Arrhenius-plot of the Cf measurements on the Cu-poor Se-series.*** *- (a) high Se (b) mid Se (c) low Se. Results of the evaluation from the derivative of the capacitance.*

A.1.4. DOS after Walter

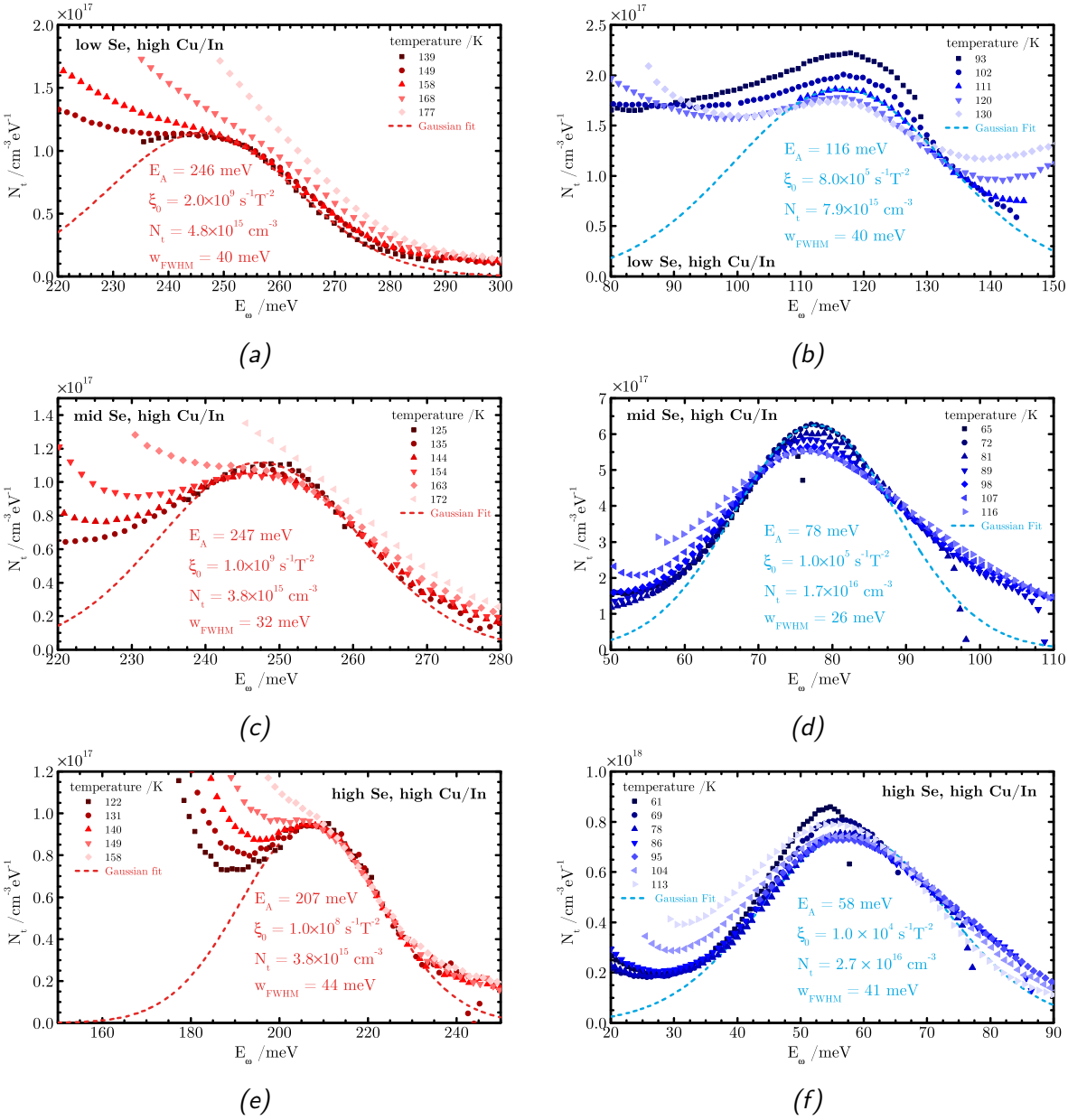

Figure A.10.: ***Fitting of the DOS after Walter et al. on the high Cu/In ratio series*** *- Fitting for:*
low Se during growth: a) high (step2) & b) low (step3) temperature response ;
mid Se during growth: c) high (step2) & d) low (step3) temperature response;
high Se during growth: e) high (step2) & f) low (step3) temperature response.

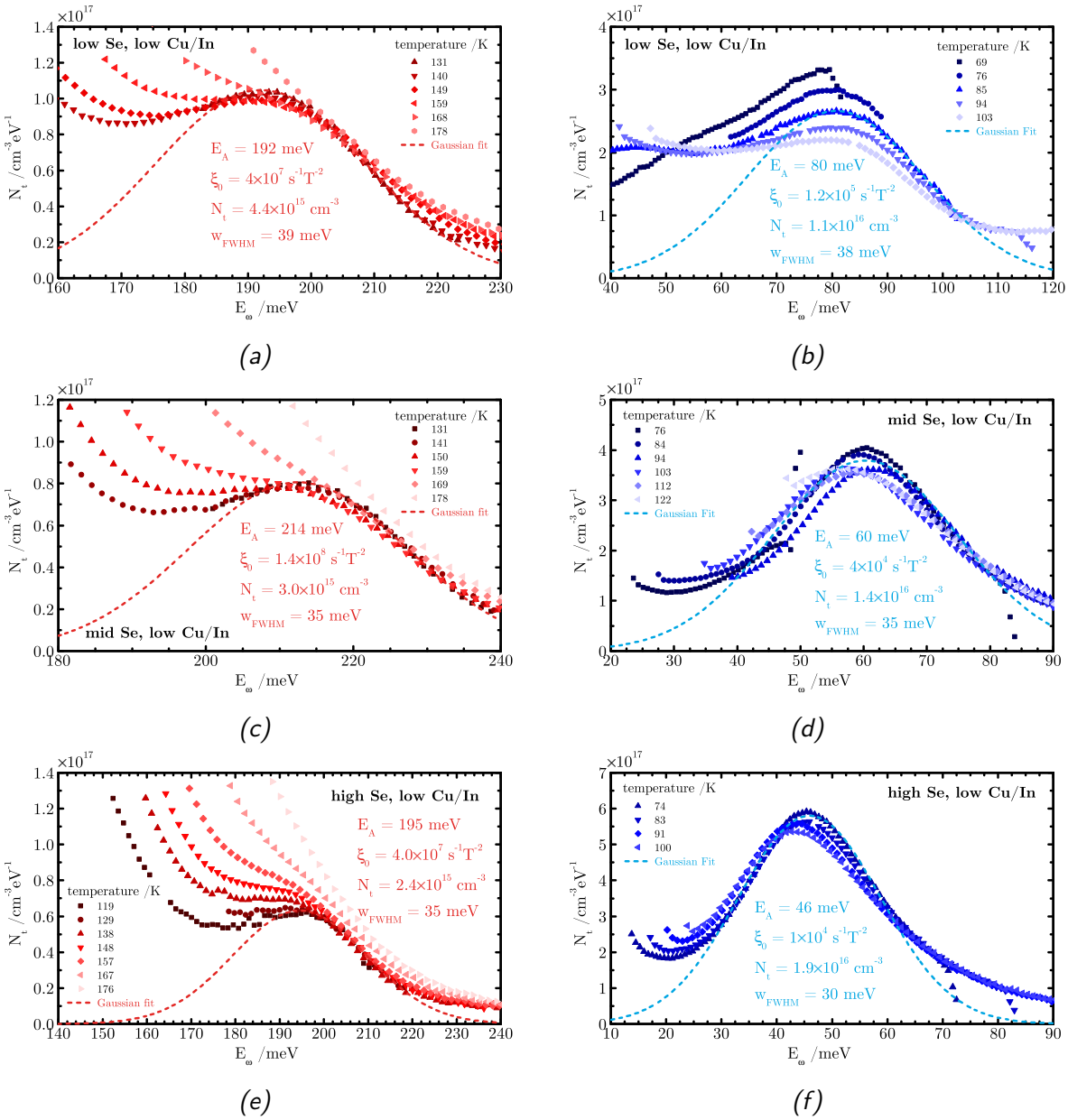

Figure A.11.: ***Fitting of the DOS after Walter et al. on the low Cu/In ratio series*** - *Fitting for:*
low Se during growth: a) high (step2) & b) low (step3) temperature response;
mid Se during growth: c) high (step2) & d) low (step3) temperature response;
high Se during growth: e) high (step2) & f) low (step3) temperature response.

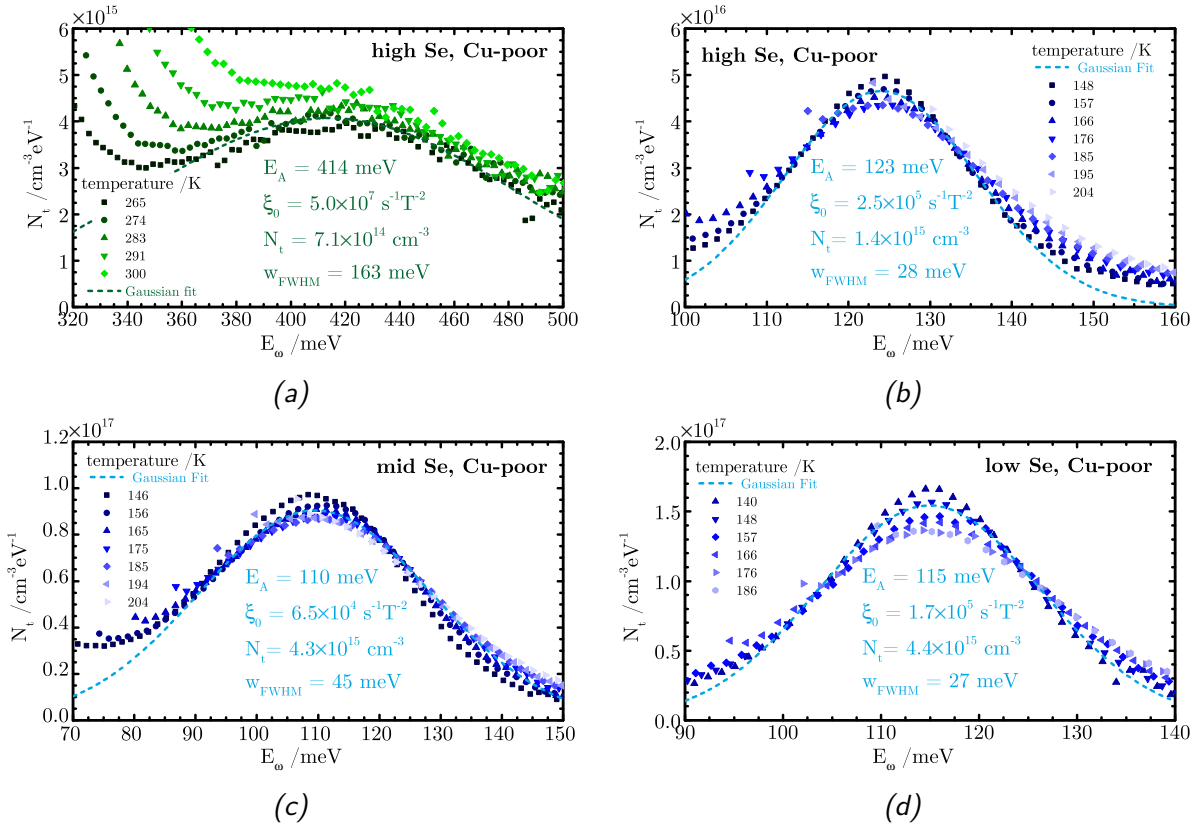

Figure A.12.: ***Fitting of the DOS after Walter et al. on the Cu-poor series.*** *- a) High temperature response (step 1) of the high Se sample b) Medium temperature response (step 3) of the high Se sample c) Medium temperature response (step 3) of the mid Se sample d) Medium temperature response (step 3) of the low Se sample.*

A.2. Supplementary graphs from the Indium-Selenium Treatment Study

A.2.1. IVT measurement results

First series

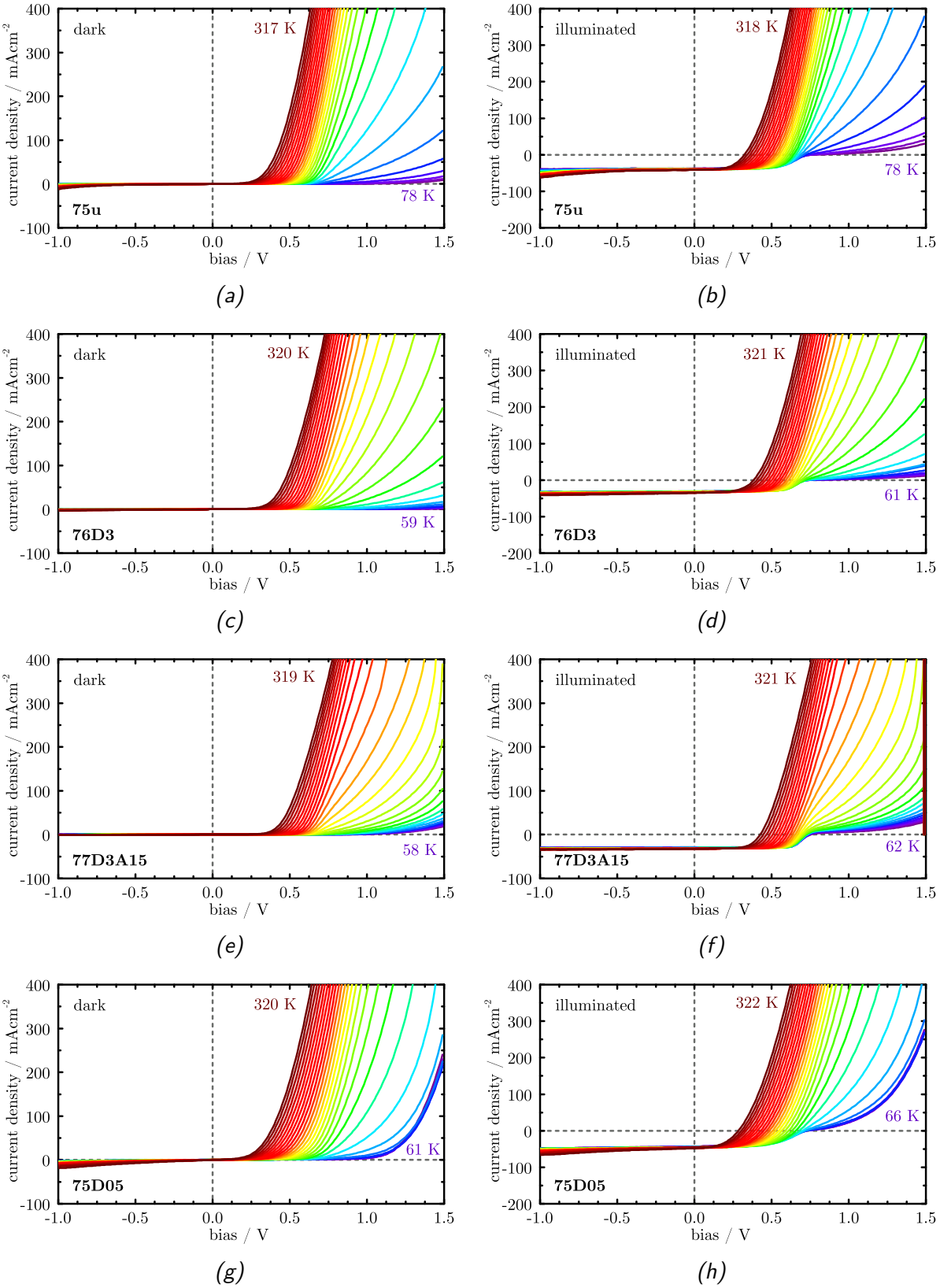

Figure A.13.: ***IVT results for the first treated samples*** *- left column dark, right column illuminated curves*

Second series

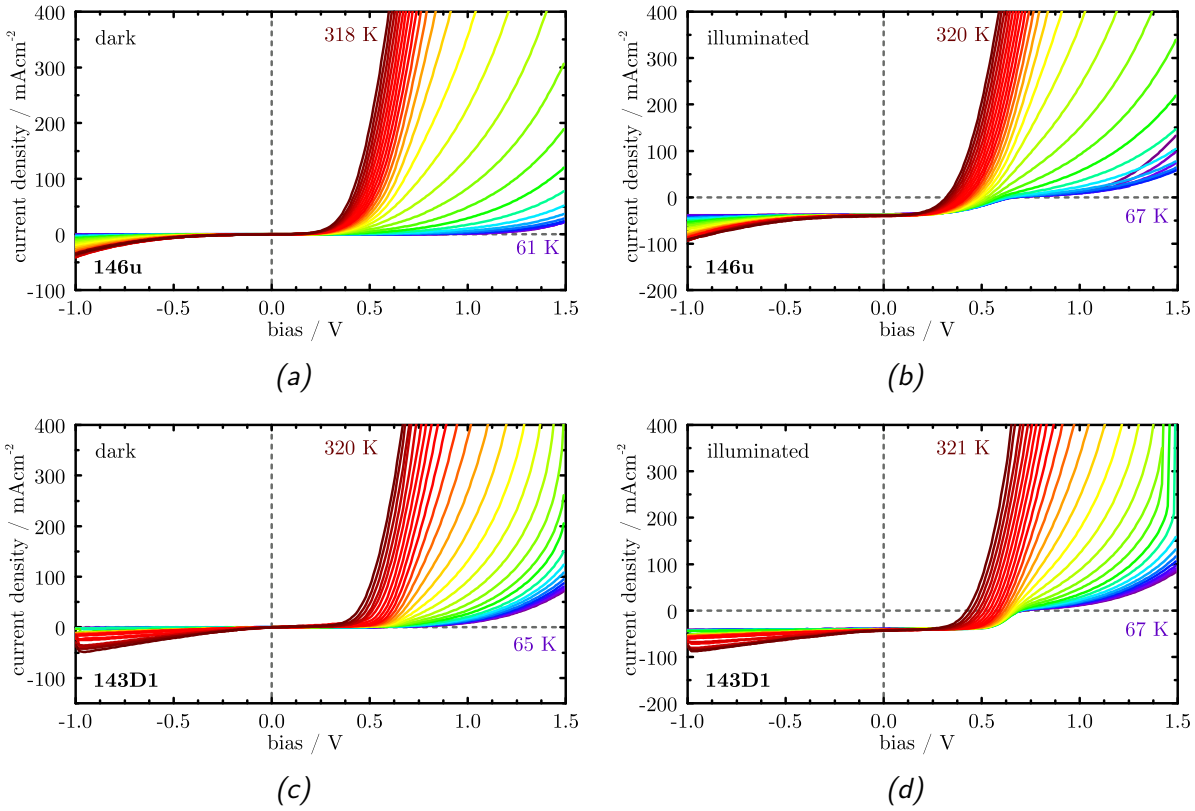

Figure A.14.: ***IVT results for the second treated samples*** *- left column dark, right column illuminated curves*

A.2.2. Thermal admittance spectra

First series

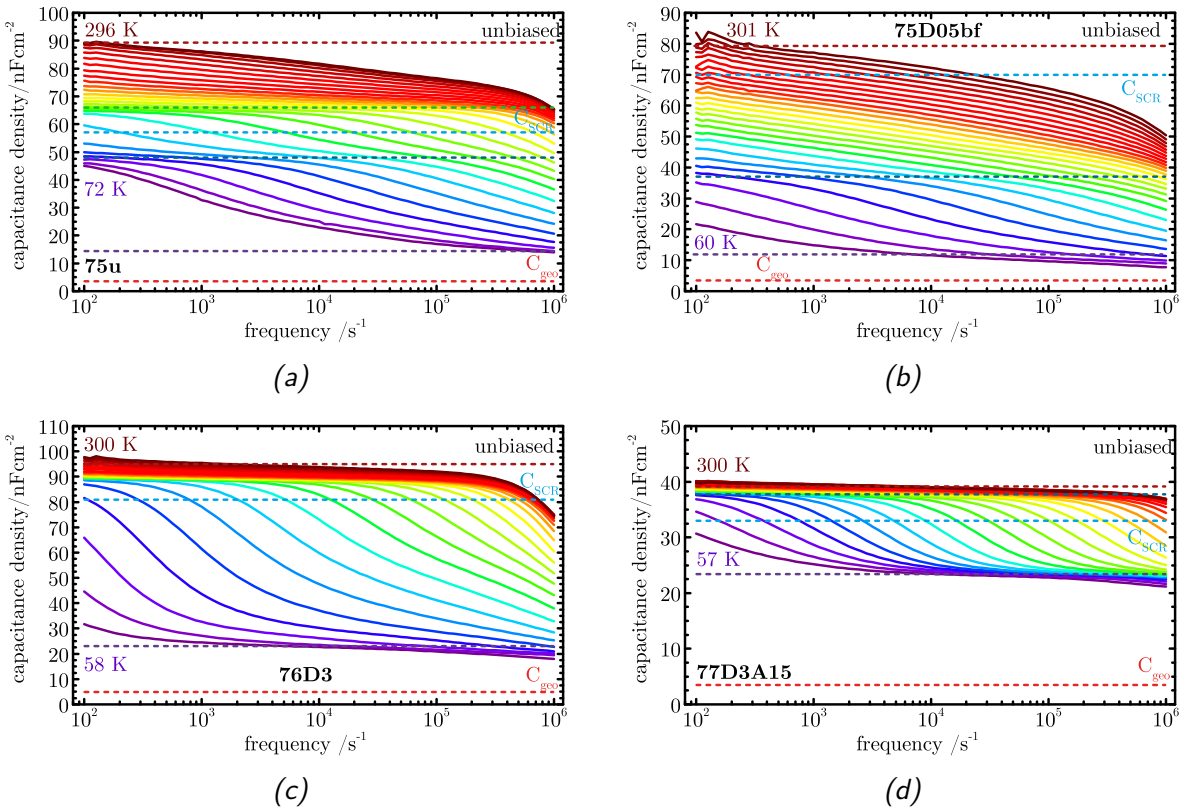

Figure A.15.: ***Admittance-measurements of the first treated series.*** *- a) Untreated Cu-rich, low Se sample (75u) b) Short treated sample (without CdS-buffer) (75D05bf) c) Deposition-only sample (76D3) d) Deposition-Annealing sample (77D3A15)*

Second series

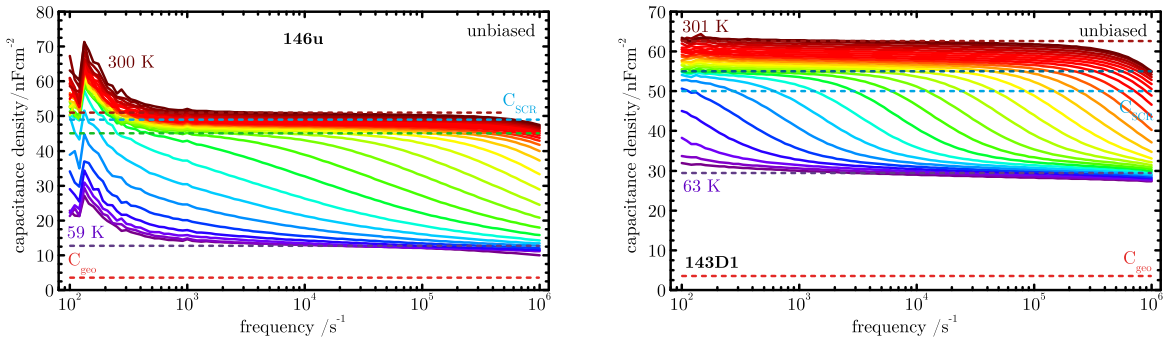

(a) (b)

Figure A.16.: ***Admittance-measurements of the second treated series.*** *- a) Of untreated (146u) and b) treated (143D1) sample.*

A.2.3. Arrhenius analysis

First series

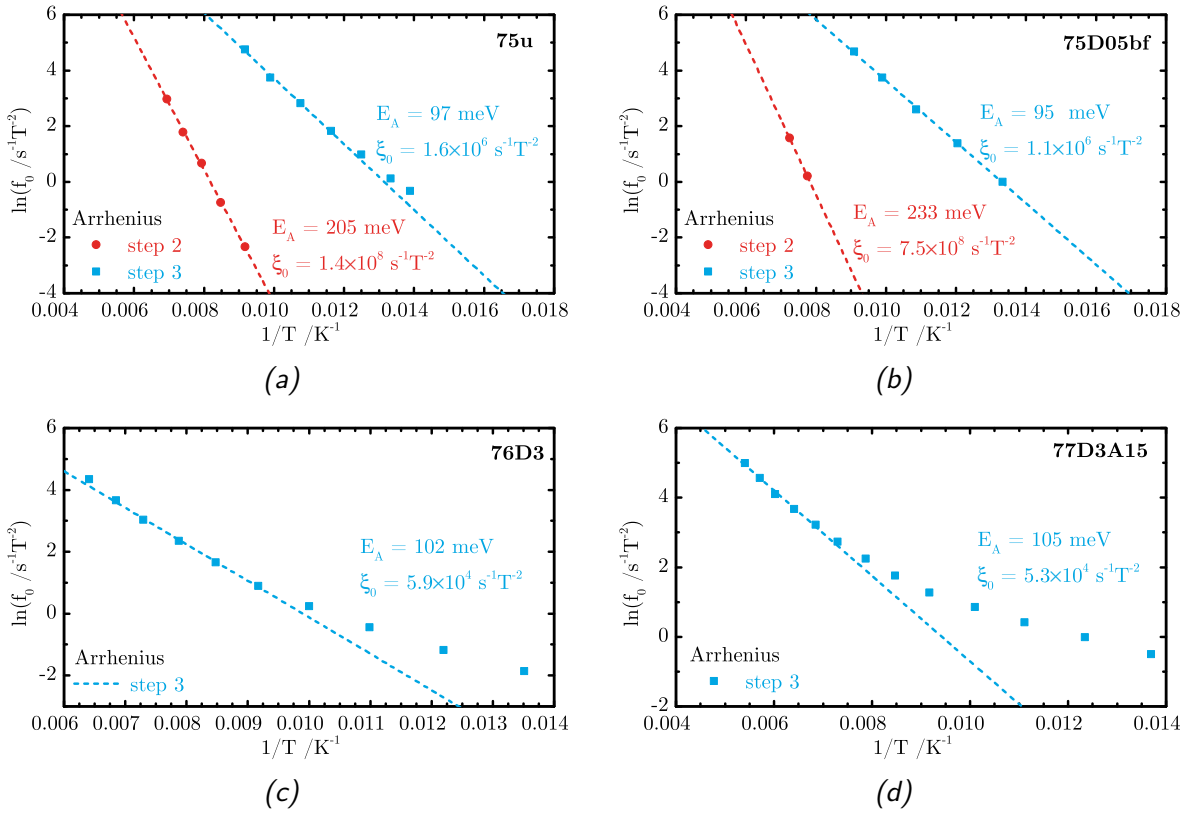

Figure A.17.: ***Arrhenius-plot of the Cf measurements on the first treatment samples.*** *- a) Untreated Cu-rich, low Se samlple (75u) b) Short treated sample (without CdS-buffer) (75D05bf) c) Deposition-only sample (76D3) d) Deposition-Annealing sample (77D3A15)*

Second series

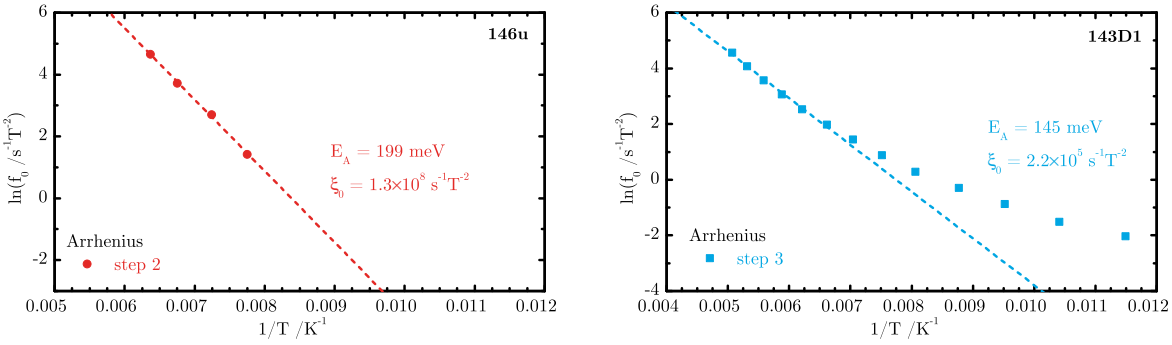

(a) (b)

Figure A.18.: ***Arrhenius-plot of the Cf measurements on the second treatment samples.*** *- a) Of untreated (146u) and b) treated (143D1) sample.*

A.2.4. DOS after Walter

First series

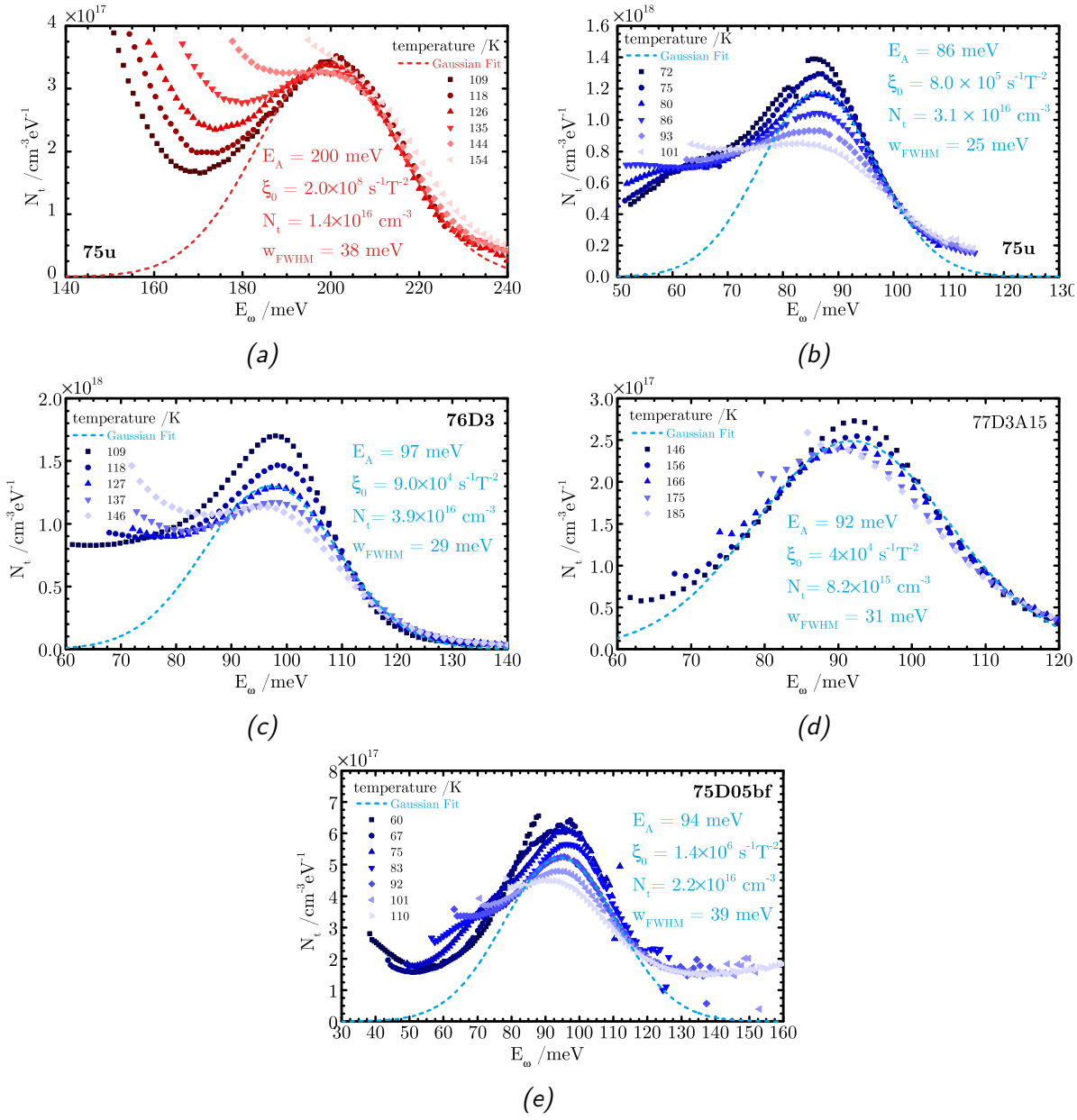

Figure A.19.: ***Walter analysis of all the defects in the first treated series*** *- Defect fitting after Walter et al. [58] for: a) high and b) low temperature response of untreated reference sample 75u. Responses of the treated samples: c) 76D3, d) 77D3A15 and d) 75D05bf are all from a response at low temperatures.*

Second series

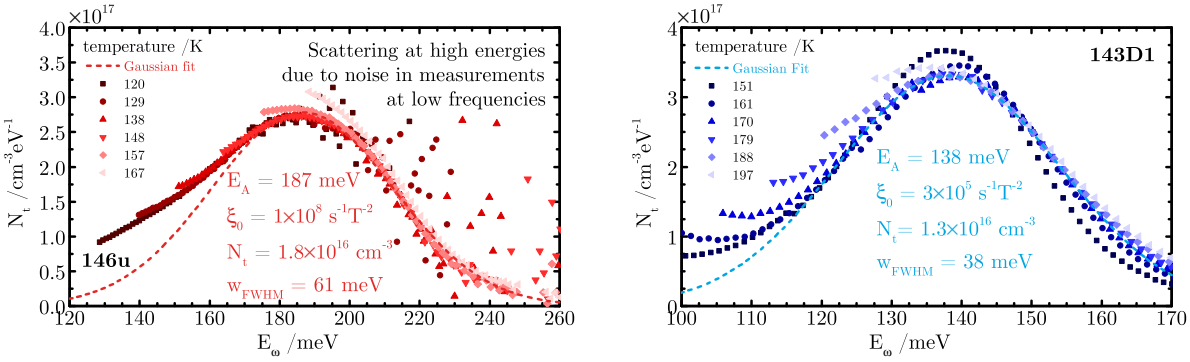

Figure A.20.: ***Walter analysis of all the defects in the second treated series*** *- Defect fitting after Walter et al. [58] for: a) untreated reference sample 146u b) treated sample 143D1.*

APPENDIX

B

ACKNOWLEDGEMENTS

There are many people to whom I owe a huge amount of gratitude - teachers, friends and family who supported me along this journey to the finalization of this very thesis. Thank you for all the shared experiences and great times.

First I want to thank Prof. Dr. Susanne Siebentritt, for the chance to work at the Laboratory for Photovoltaics and the opportunity to do research in the field of renewable energies, which was not only scientifically interesting, but also made me feel a sense of purpose within my work. Thank you for you guidance and helpful advice.
Dr. Valérie Deprédurand, who taught me everything I needed to know to get started on CIS, co-evaporation and the basic characterization techniques. And also for being a pleasant office neighbour.
Prof. Dr. Wolfram Heimbrodt, who took me into his workgroup during my diploma studies, who introduced me to semiconductor physics and then also kindly agreed to take part in my dissertation committee. On that note, I am also very grateful to the remaining members of my committee, Prof. Dr. Johan Lauwaert and Prof. Dr. Thomas Schmidt.
Thanks to all my colleagues from LPV and LEM, the time I spent in Luxembourg was a great experience and I will leave with many fond memories. Patricia Ramoa for ordering and organization and who solely keeps both teams from being buried in paperwork. Thomas Schuler for technical support, i.e. fixing the machines faster than me or the rest of the team could break them. Maxime Thevenin and Michele Melchiorre, without whom I would not have any finished solar cells or SEM of my samples and who handled all the chemicals that I am too chicken to go close to.
All my current and former colleagues: Alex, Alexandre, Anastasia, Conrad, Diego, Erika, Finn, Germain, Hiroki, Hossam, Jan, Jessica, Leo, Mads, Sara, Yukari.
David for the template of his thesis, all the talks and help. Thommy, for Shake Shack, Pumpen, Clashn etc. generally all the great fun that comes from starting a new job at the same time. Moniczka for your support and steady believe in me. Phil and Nico, for being crazy and brave enough, twice. Pete for Tuesdays with gin and always being less than a call away.
And all the other friends and colleagues I met along the way, throughout school and university, up to now and hopefully beyond and with them the discussions both on-and off topic, the wine fridays and kitchen meetings. Who are to many to name all.
And finally I very much want to thank my family: my parents and my two brothers for all their support and encouragement.

APPENDIX

C

GLOSSARY

Table C.1.: *Abbreviations*

AM	air mass
BFM	beam flux monitor
CBD	chemical bath deposition
CGS	$CuGaSe_2$
CIS	$CuInSe_2$
CIGS	$Cu(In,Ga)Se_2$
CV	capacitance-voltage
DFT	density functional theory
DOS	density of states
EDX	energy dispersive X-ray diffraction
EIES	electron impact spectroscope
EPT	energy payback time
EQE	external quantum efficiency
HF	Hartree-Fock
HSE	Heyd, Scuseria and Ernzerhof, [42]
IQE	internal quantum efficiency
IV	current-voltage
IVT	temperature-dependant current-voltage
MBE	molecular beam epitaxy
MEE	multi-excitation entropy
MN	Meyer-Neldel, [73]
PL	photoluminescence
PMT	photomultiplier tube
PV	photovoltaics
PVD	physical vapour deposition
QCM	quartz micro-balance
QE	quantum efficiency
SCR	space-charge region
SEM	scanning electron microscope
TAS	thermal admittance measurements
TCO	transparent conductive oxide
XRD	X-ray diffraction

Table C.2.: *Acronyms and Symbols*

Symbol	Unit	Description
A		diode quality factor
$\mathcal{A}_b$		absorbance of buffer layer
$\mathcal{A}_w$		absorbance of window layer
α	nm^{-1}	absorption coefficient
c_h	s^{-1}	hole capture rate
$\tilde{c}_h$	$cm^3 \cdot s^{-1}$	hole capture coefficient
C	$F \cdot cm^{-2}$	capacitance
C_{geo}	$nF \cdot cm^{-2}$	geometrical capacitance
C_{hf}	$nF \cdot cm^{-2}$	high frequency capacitance response
C_{lf}	$nF \cdot cm^{-2}$	low frequency capacitance response
C_m	$nF \cdot cm^{-2}$	measured capacitance value
C_p	$nF \cdot cm^{-2}$	capacitance measured in parallel
C_{scr}	$nF \cdot cm^{-2}$	space-charge region capacitance
$C_{scr,bc}$	$nF \cdot cm^{-2}$	space-charge region capacitance of the primary junction
$C_{scr,pn}$	$nF \cdot cm^{-2}$	space-charge region capacitance of the back-contact
C_{up}	$F \cdot cm^{-2}$	low frequency capacitance, before defect step
d_{abs}	μm	thickness of the absorber layer
D	$m^2 s^{-1}$	diffusion coefficient
e_h	s^{-1}	hole emission rate
E	eV	energy
E_A	eV	defect activation energy
$E_{A,rec}$	eV	activation energy of main recombination pathway
E_F	eV	Fermi level
E_{Fn}	eV	bulk quasi-Fermi level in n-side of junction
E_{Fp}	eV	bulk quasi-Fermi level in p-side of junction
E_g	eV	bandgap energy
E_ω	eV	Walter energy axis [58]
E_{ph}	eV	phonon energy
E_t	eV	position of a deep trap within bandgap
E_{vac}	eV	vacuum level
$\mathcal{E}$	Vm^{-1}	electric field
η	%	power conversion efficiency
f	s^{-1}	measurement frequency
f_0	s^{-1}	trap response frequency
f_{crit}	s^{-1}	critical frequency in admittance spectrum
$\mathcal{FF}$		fill factor
g_t	S	conductance due to deep defects
G	S	conductance
$\mathcal{G}$	$kJ \cdot mol^{-1}$	Gibbs free energy
Γ		external collection efficiency
J	$mA \cdot cm^{-2}$	current density
J_0	$mA \cdot cm^{-2}$	saturation current density
J_{00}	$mA \cdot cm^{-2}$	reference current density
J_{diode}	$mA \cdot cm^{-2}$	diode current density
J_{light}	$mA \cdot cm^{-2}$	total current density

J_Q	$mA \cdot cm^{-2}$	charge current density
J_{SC}	$mA \cdot cm^{-2}$	short-circuit current density
κ	$S \cdot m^{-1}$	conductivity
κ_n	$S \cdot m^{-1}$	conductivity of electrons
κ_h	$S \cdot m^{-1}$	conductivity of holes
L_{di}	μm	diffusion length
L_{dr}	μm	drift length
L_{eff}	µm	effective collection length
λ	nm	wavelength
μ	eV	electrochemical potential
μ_n	eV	electrochemical potential of electrons
μ_p	eV	electrochemical potential of holes
N	cm^{-3}	density of free carriers
N_0	cm^{-3}	density of free carriers in steady state
N_a	cm^{-3}	density of shallow acceptors
N_{CV}	cm^{-3}	free carrier density from CV
N_d	cm^{-3}	density of shallow donators
N_i	cm^{-3}	intrinsic carrier density
N_p	cm^{-3}	density of trapped holes
$N_{p,\,0}$	cm^{-3}	density of trapped holes in steady state
N_t	cm^{-3}	density of deep traps
N_V	cm^{-3}	density of thermalized holes from the valence band
$\mathcal{N}_{x,i}$		number of excitations in interaction volume
$\mathcal{N}_{x,n}$		number of necessary excitations
ν_0	s^{-1}	attempt-to-escape frequency
ω	s^{-1}	angular frequency
ω_{ph}	s^{-1}	phonon frequency
p	Pa	pressure
P_{in}	W	input power
P_{max}	W	maximum power point
P_{subs}	%	power of the substrate heater (as % of maximum output)
$\mathcal{P}_H$		hopping probability
φ	V	electrical potential
φ_n	V	electrical potential on n-side
φ_p	V	electrical potential on p-side
q	$C \cdot cm^{-2}$	charge density
q_a	$C \cdot cm^{-2}$	charge stored in shallow acceptors
q_t	$C \cdot cm^{-2}$	charge stored in deep traps
r	s^{-1}	temperature activated observable
r_0	s^{-1}	activation prefactor
r_{00}	s^{-1}	constant of activation prefactor
R_S	Ω	series resistance
R_{Sh}	Ω	shunt resistance
$R_{Sh,bc}$	Ω	shunt resistance of the primary junction
$R_{Sh,pn}$	Ω	shunt resistance of the back-contact
$\mathcal{R}_f$		reflectance of front layers
ρ	$C \cdot cm^{-3}$	distribution of charge density
$\mathcal{S}$	$J \cdot kg^{-1}$	entropy

S	S	susceptance
σ_n	m^{-1}	electron capture crosssection
σ_p	m^{-1}	hole capture crosssection
t	s	temporal coordinate
T	K	temperature
T_{iso}	K or °C	isokinetic temperature
$\mathcal{T}_g$		transmittance through grid
τ_h	s	mean time of hole in VB prior to capture event
τ_{di}	s	diffusion time
τ_{dr}	s	drift time
θ_m	°	phase angle
$\mathcal{U}$	J	inner energy
v_{th}	$cm \cdot s^{-1}$	thermal velocity
V	V	voltage
V_0	V	voltage amplitude
V_{AC}	V	small AC bias voltage
V_{app}	V	applied voltage
V_{bi}	V	built-in voltage
V_{OC}	mV	open-circuit voltage
V_t	V	potential difference due to charged traps
$\mathcal{V}$	m^3	volume
w_{FWHM}	eV	full width at half maximum of Gaussian fit
$\mathcal{W}$		number of microscopic states
x	m	spatial coordinate
x_H	nm	hopping range
x_n	nm	space-charge region on n-side
x_p	nm	space-charge region on p-side
x_{SCR}	nm	space-charge region width
$\tilde{x}_t$	nm	location of intersect between deep defect and Fermi level
ξ_0	$s^{-1} \cdot T^{-2}$	thermal pre-factor of a measured defect
ξ_{00}	$s^{-1} \cdot T^{-2}$	thermal pre-factor of a defect group
Y	S	admittance

Table C.3.: *Constants*

Symbol	Value	Description
k_B	$8.617 \cdot 10^{-5}$ eV $\cdot$ K^{-1}	Boltzmann constant
ϵ_0	$8.854 \cdot 10^{-12}$ F $\cdot$ m^{-1}	absolute dielectric permittivity
ϵ_r	12	relative dielectric permittivity of $CuInSe_2$ [52]
h	$4.135 \cdot 10^{-15}$ eV $\cdot$ s	Planck constant
$\hbar$	$6.582 \cdot 10^{-16}$ eV $\cdot$ s	reduced Planck constant
i	$\sqrt{-1}$	imaginary unit
q_e	$1.602 \cdot 10^{-19}$ C	elementary charge

APPENDIX

D

LIST OF PUBLICATIONS AND CONFERENCES

Publications

First author

T. Bertram, V. Deprédurand, S. Siebentritt. Electrical Characterization of Defects in Cu-rich Grown $CuInSe_2$ Solar Cells. *IEEE Journal of Photovoltaics*, 6:546 - 551, 2016.

T. Bertram, V. Deprédurand, S. Siebentritt. In-Se surface treatment of Cu-rich grown $CuInSe_2$. *Proceedings of the IEEE Photovoltaic Specialist Conference 2014*:3633 - 3636, 2014.

Co-author

L. Choubrac, **T. Bertram**, H. ElAnzeery, S. Siebentritt. Better $Cu(In,Ga)Se_2$ solar cells based on surface treated stoichiometric absorbers, *submitted to Applied Physics Letters*, 2016.
Own contribution: PVD growth of $Cu(In,Ga)Se_2$ absorbers

M. Hála, S. Fujii, A. Redinger, Y. Inoue, G. Rey, M. Thévenin, V. Deprédurand, T.P. Weiss, **T. Bertram**, S. Siebentritt. Highly conductive ZnO films with high NIR transparency, *Prog. Photovolt: Res. Appl.*, 23:1630-1641, 2015.
Own contribution: PVD growth of $CuInSe_2$ absorbers

S. Siebentritt, G. Rey, A. Finger, D. Regesch, J. Sendler, T. P. Weiss, **T. Bertram**. What is the Bandgap of Kesterite?, *Solar Energy Materials and Solar Cells*, (Available online 31 October 2015).
Own contribution: PVD growth of $CuInSe_2$ absorbers, QE measurements

D. Colombara, **T. Bertram**, V. Deprédurand, T. Fouquet, J. Bour, C. Broussillou, P.-P. Grand, P. Dale. Prediction of Photovoltaic $Cu(In,Ga)Se_2$ p-n Device Performance by forward Bias Electrochemical Analysis of Only the p-Type $Cu(In,Ga)Se_2$ Films. *Electrochemical Society Transactions*, 66:19-25, 2015.
Own contribution: PVD growth of $CuInSe_2$ absorbers

V. Deprédurand, **T. Bertram**, M. Thévenin, N. Valle, J.N. Audinot, S. Siebentritt. Alternative Etching for Improved Cu-rich $CuInSe_2$ Solar Cells. *MRS Proceedings*,

1771:163-138, 2015.
Own contribution: PVD growth of $CuInSe_2$ absorbers, IV measurements

U. Berner, D. Colombara, **T. Bertram**, J.C.B. Malaquias, H. Meadows, N. Valle, M. Widenmeyer, P. Dale. Vapour phase alkali species for $Cu(In,Ga)Se_2$ solar cells. *31st European Photovoltaic Solar Energy and Conversion*, 2015.
Own contribution: CV measurements

J. Luckas, C. Longeaud, **T. Bertram**, S. Siebentritt. Metastable defect in $CuInSe_2$ probed by modulated photo current experiments above 390 K. *Applied Physics Letters*, 104:153905, 2014.
Own contribution: PVD growth of $CuInSe_2$ absorbers

V. Deprédurand, **T. Bertram**, D. Regesch, B. Henx, S. Siebentritt. The influence of Se pressure on the electronic properties of $CuInSe_2$ grown under Cu-excess. *Applied Physics Letters*, 105:172104, 2014.
Own contribution: PVD growth of $CuInSe_2$ absorbers, IV, CV, XRD measurements

V. Deprédurand, **T. Bertram**, S. Siebentritt. Influence of the Se environment on Cu-rich CIS devices. *Physica B: Condensed Matter*, 439:101-104, 2014.
Own contribution: PVD growth of $CuInSe_2$ absorbers, IV, CV, QE, XRD measurements

Conference contributions

Oral Presentation

T. Bertram, V. Deprédurand, S. Siebentritt. In-Se surface treatment of Cu-rich grown $CuInSe_2$. *40th IEEE Photovoltaic Specialist Conference*, Denver, 2014.

T. Bertram, V. Deprédurand, J. Luckas, S. Siebentritt. Defect study of Cu-rich grown $CuInSe_2$ solar cells. *27th International Conference on Defects in Semiconductors*, Bologna, 2013.

Poster

T. Bertram, V. Deprédurand, J. Guillot, S. Siebentritt. Defect investigation of In-Se surface treated, Cu-rich grown $CuInSe_2$ solar cells. *MRS Spring Meeting and Exhibit*, San Francisco, 2015.

LIST OF FIGURES

LIST OF TABLES

BIBLIOGRAPHY

[1] IEA. Solar Energy Perspectives 2011, downloaded from: http://www.iea.org/publications/freepublications/publication/solar-energy-perspectives.html, 2011. 7

[2] IEA. 2015 Snapshot Of Global Photovoltaic Markets, downloaded from http://www.iea-pvps.org/index.php?id=92&eID=dam_frontend_push&docID=2797, Accessed on: 2015-05-30. 7

[3] Greenpeace, Revolution A Sustainable World Energy Outlook 2015, downloaded from: http://www.greenpeace.org/international/en/publications/Campaign-reports/Climate-Reports/Energy-Revolution-2015/, accessed on: 30-05-2016. 7

[4] The Energy Report, downloaded from: http://www.ecofys.com/en/publication/the-energy-report, accessed on: 04.06.2016. 7

[5] IRENA, Renewable Energy and Jobs - Annual Review 2016, downloaded from: http://www.irena.org/DocumentDownloads/Publications/IRENA_RE_Jobs_Annual_Review_2016.pdf, accessed on 02.06.2016, 2016. 7

[6] Fraunhofer ISE, Photovoltaics Report 2015, downloaded from: https://www.ise.fraunhofer.de/de/downloads/pdf-files/aktuelles/photovoltaics-report-in-englischer-sprache.pdf, accessed on: 31.03.2016. 7, 8

[7] M. Kaelin, D. Rudmann, and A.N. Tiwari. Low cost processing of CIGS thin film solar cells. *Solar Energy*, 77(6):749–756, 2004. 7

[8] S. Wagner, J.L. Shay, P. Migliorato, and H.M. Kasper. $CuInSe_2$/CdS heterojunction photovoltaic detectors. *Applied Physics Letters*, 25(8):434, 1974. 7

[9] J.L. Shay, S. Wagner, and H.M. Kasper. Efficient $CuInSe_2$/CdS solar cells. *Applied Physics Letters*, 27(2):89, 1975. 7

[10] NREL, Solar Efficiency Chart, downloaded from: http://www.nrel.gov/ncpv/images/efficiency_chart.jpg, accessed on: 30.05.2016. 8

[11] S. Chichibu, T. Mizutani, K. Murakami, T. Shioda, T. Kurafuji, H. Nakanishi, S. Niki, P.J. Fons, and A. Yamada. Band gap energies of bulk, thin-film, and epitaxial layers of $CuInSe_2$ and $CuGaSe_2$. *Journal of Applied Physics*, 83(7):3678, 1998. 8

[12] M.I. Alonso, K. Wakita, J. Pascual, M. Garriga, and N. Yamamoto. Optical functions and electronic structure of $CuInSe_2$, $CuGaSe_2$, $CuInS_2$, and $CuGaS_2$. *Phys. Rev. B*, 63(7):75203, 2001. 8

[13] P.D. Paulson, R.W. Birkmire, and W.N. Shafarman. Optical characterization of $CuIn_{1-x}Ga_xSe_2$ alloy thin films by spectroscopic ellipsometry. *Journal of Applied Physics*, 94(2):879, 2003. 8

[14] A. Chirilă, P. Reinhard, F. Pianezzi, P. Bloesch, A.R. Uhl, C. Fella, L. Kranz, D. Keller, C. Gretener, H. Hagendorfer, D. Jaeger, R. Erni, S. Nishiwaki, S. Buecheler, and A.N. Tiwari. Potassium-induced surface modification of $Cu(In,Ga)Se_2$ thin films for high-efficiency solar cells. *Nature Materials*, 12(12):1107–1111, 2013. 8, 47, 49

[15] V.K. Kapur, A. Bansal, P. Le, and O.I. Asensio. Non-vacuum processing of $CuIn_{1-x}Ga_xSe_2$ solar cells on rigid and flexible substrates using nanoparticle precursor inks. *Thin Solid Films*, 431-432:53–57, 2003. 8

[16] V. Fthenakis and H.C. Kim. Land use and electricity generation: A life-cycle analysis. *Renewable and Sustainable Energy Reviews*, 13(6-7):1465–1474, aug 2009. 8

[17] A. Jasenek, U. Rau, T. Hahn, G. Hanna, M. Schmidt, M. Hartmann, H.W. Schock, J.H. Werner, B. Schattat, S. Kraft, K.H. Schmid, and W. Bolse. Defect generation in polycrystalline $Cu(In,Ga)Se_2$ by high-energy electron irradiation. *Applied Physics A*, 70(6):677–680, 2000. 8

[18] J.F. Guillemoles. Stability of $Cu(In,Ga)Se_2$ solar cells: a thermodynamic approach. *Thin Solid Films*, 361-362:338–345, 2000. 8

[19] J.F. Guillemoles. The puzzle of $Cu(In,Ga)Se_2$ (CIGS) solar cells stability. *Thin Solid Films*, 403-404:405–409, feb 2002. 8

[20] H.S. Ullal, K. Zwelbel, and B. Roedern. Current status of polycrystalline thin-film PV technologies. In *Photovoltaic Specialists Conference, 1997., Conference Record of the Twenty-Sixth IEEE*, pages 301–305, sep 1997. 8

[21] D.L. Losee. Admittance spectroscopy of impurity levels in Schottky barriers. *Journal of Applied Physics*, 46(5):2204, 1975. 9

[22] T. Eisenbarth. *Identifikation von Defekten und Metastabilitäten in Cu(In,Ga)Se_2-Dünnschichtsolarzellen.* PhD thesis, Freie Universität Berlin, HZB, 2010. 11

[23] H. Hahn, G. Frank, W. Klingler, A.D. Meyer, and G. Störger. Untersuchungen über ternäre Chalkogenide. V. Über einige ternäre Chalkogenide mit Chalkopyritstruktur. *Zeitschrift für anorganische und allgemeine Chemie*, 271(3-4):153–170, 1953. 12

[24] H.W. Spiess, U. Haeberlen, G. Brandt, A. Räuber, and J. Schneider. Nuclear Magnetic Resonance in I_B-III-VI_2 Semiconductors. *physica status solidi (b)*, 62(1):183–192, 1974. 12

[25] C.H. Chang, S.H. Wei, W. Johnson, R. Bhattacharya, B.J. Stanbery, T.J. Anderson, and R. Duran. Long and Short Range Ordering of $CuInSe_2$. *Japanese Journal of Applied Physics*, 39(S1):411, 2000. 12

[26] S.B. Zhang, S.H. Wei, and A. Zunger. Stabilization of Ternary Compounds via Ordered Arrays of Defect Pairs. *Phys. Rev. Lett.*, 78(21):4059–4062, may 1997. 12

[27] B.J. Stanbery. Copper Indium Selenides and Related Materials for Photovoltaic Devices. *Critical Reviews in Solid State and Materials Sciences*, 27(2):73–117, 2002. 12

[28] D. Schmid, M. Ruckh, and H.W. Schock. Photoemission studies on Cu(In, Ga)Se_2 thin films and related binary selenides. *Applied Surface Science*, 103(4):409–429, 1996. 12

[29] D. Schmid, M. Ruckh, F. Grunwald, and H. W. Schock. Chalcopyrite/defect chalcopyrite heterojunctions on the basis of $CuInSe_2$. *Journal of Applied Physics*, 73(6):2902–2909, 1993. 13

[30] E. Korhonen, K. Kuitunen, F. Tuomisto, A. Urbaniak, M. Igalson, J.K. Larsen, L. Gütay, S. Siebentritt, and Y. Tomm. Vacancy defects in epitaxial thin film $CuGaSe_2$ and $CuInSe_2$. *Phys. Rev. B*, 86(6):64102, 2012. 13, 56

[31] A. Gerhard, W. Harneit, S. Brehme, A. Bauknecht, U. Fiedeler, M.C. Lux-Steiner, and S. Siebentritt. Acceptor activation energies in epitaxial $CuGaSe_2$ grown by MOVPE. *Thin Solid Films*, 387(1-2):67–70, 2001. 13

[32] S.M. Wasim. Transport properties of $CuInSe_2$. *Solar Cells*, 16:289–316, 1986. 13

[33] E. Arushanov, J.H. Schön, H. Matsushita, and T. Takizawa. Impurity Band in p-Type $CuInSe_2$. *physica status solidi (a)*, 176(2):1009–1016, 1999. 13

[34] C. Strothkämper, A. Bartelt, R. Eichberger, C. Kaufmann, and T. Unold. Microscopic mobilities and cooling dynamics of photoexcited carriers in polycrystalline $CuInSe_2$. *Phys. Rev. B*, 89(11):115204, 2014. 13

[35] T. Unold, H. Hempel, C. Strothkämper, C.A. Kaufmann, R. Eichberger, and A. Bartelt. Charge carrier mobilities and dynamics in thin film compound semiconductor materials from transient Thz absorption. In *Photovoltaic Specialist Conference (PVSC), 2014 IEEE 40th*, pages 2066–2069, 2014. 13

[36] L. Gütay, D. Regesch, J.K. Larsen, Y. Aida, V. Deprédurand, and S. Siebentritt. Influence of copper excess on the absorber quality of $CuInSe_2$. *Applied Physics Letters*, 99:15192, 2011. 13

[37] D. Regesch, L. Gütay, J.K. Larsen, V. Deprédurand, D. Tanaka, Y. Aida, and S. Siebentritt. Degradation and passivation of $CuInSe_2$. *Applied Physics Letters*, 101(11):112108, 2012. 13, 15, 47, 49

[38] R. Noufi, R. Axton, C. Herrington, and S.K. Deb. Electronic properties versus composition of thin films of $CuInSe_2$. *Applied Physics Letters*, 45(6):668, 1984. 14

[39] I. Dirnstorfer, M. Wagner, D.M. Hofmann, M.D. Lampert, F. Karg, and B.K. Meyer. Characterization of CuIn(Ga)Se_2 Thin Films. *physica status solidi (a)*, 168(1):163–175, 1998. 14

[40] S. Siebentritt, N. Rega, A. Zajogin, and M.C. Lux-Steiner. Do we really need another PL study of $CuInSe_2$? *Physica Status Solidi C: Conferences*, 1(9):2304–2310, 2004. 15, 61

[41] A. Krysztopa, M. Igalson, L. Gütay, J.K. Larsen, and Y. Aida. Defect level signatures in $CuInSe_2$ by photocurrent and capacitance spectroscopy. *Thin Solid Films*, 535:366–370, 2013. 15, 59, 60, 62

[42] J. Heyd, G.E. Scuseria, and M. Ernzerhof. Hybrid functionals based on a screened Coulomb potential. *The Journal of Chemical Physics*, 118(18):8207, 2003. 15, 102

[43] J. Pohl and K. Albe. Intrinsic point defects in $CuInSe_2$ and $CuGaSe_2$ as seen via screened-exchange hybrid density functional theory. *Phys. Rev. B*, 87(24):245203, jun 2013. 15

[44] L.E. Oikkonen, M.G. Ganchenkova, A.P. Seitsonen, and R.M. Nieminen. Formation, migration, and clustering of point defects in $CuInSe_2$ from first principles. *Journal of Physics: Condensed Matter*, 26(34):345501, 2014. 15

[45] J. Bekaert, R. Saniz, B. Partoens, and D. Lamoen. Native point defects in $CuIn_{1-x}Ga_xSe_2$: hybrid density functional calculations predict the origin of p- and n-type conductivity. *Phys. Chem. Chem. Phys.*, 16(40):22299–22308, 2014. 15, 16

[46] J. Pohl, A. Klein, and K. Albe. Role of copper interstitials in $CuInSe_2$: First-principles calculations. *Physical Review B*, 84(12):121201, 2011. 15

[47] L.E. Oikkonen, M.G. Ganchenkova, A.P. Seitsonen, and R.M. Nieminen. Vacancies in $CuInSe_2$: new insights from hybrid-functional calculations. *Journal of Physics: Condensed Matter*, 23(42):422202, 2011. 15

[48] L.E. Oikkonen, M.G. Ganchenkova, A.P. Seitsonen, and R.M. Nieminen. Mass transport in $CuInSe_2$ from first principles. *Journal of Applied Physics*, 113(13):133510, 2013. 16

[49] L.E. Oikkonen, M.G. Ganchenkova, A.P. Seitsonen, and R.M. Nieminen. Redirecting focus in $CuInSe_2$ research towards selenium-related defects. *Phys. Rev. B*, 86(16):165115, 2012. 16

[50] S.M. Sze and K.K. Ng. Physics and Properties of Semiconductors. 2006. 16, 17, 33, 53

[51] P. Würfel. *Physics of Solar Cells - From Basic Principles to Advanced Concepts*. Wiley-VCH Verlag GmbH & Co. KGaA, Weinheim, Germany, 2009. 17

[52] R. Scheer and H.W. Schock. *Chalcogenide Photovoltaics: Physics, Technologies, and Thin Film Devices*. Wiley-VCH Verlag GmbH & Co. KGaA, Weinheim, Germany, 2011. 19, 20, 21, 22, 57, 105

[53] A.R. Burgers, J.A. Eikelboom, A. Schonecker, and W.C. Sinke. Improved treatment of the strongly varying slope in fitting solar cell I-V curves. In *Photovoltaic Specialists Conference, 1996., Conference Record of the Twenty Fifth IEEE*, pages 569–572, 1996. 20, 53

[54] S.S. Hegedus and W.N. Shafarman. Thin-film solar cells: device measurements and analysis. *Progress in Photovoltaics: Research and Applications*, 12(23):155–176, 2004. 24, 25

[55] C.A. Gueymard, D. Myers, and K. Emery. Proposed reference irradiance spectra for solar energy systems testing. *Solar Energy*, 73(6):443–467, 2002. 24

[56] X.X. Liu and J.R. Sites. Solar-cell collection efficiency and its variation with voltage. *Journal of Applied Physics*, 75(1):577, 1994. 25

[57] P. Blood and J.W. Orton. *The Electrical Characterization of Semiconductors Majority Carriers and Electron States*. Academic Press Limited, London, 1992. 26, 38

[58] T. Walter, R. Herberholz, C. Müller, and H.W. Schock. Determination of defect distributions from admittance measurements and application to Cu(In,Ga)Se_2 based heterojunctions. *Journal of Applied Physics*, 80(8):4411–4420, 1996. 29, 30, 99, 100, 103, 110

[59] M. Sakhaf and M. Schmeits. Capacitance and conductance of semiconductor heterojunctions with continuous energy distribution of interface states. *Journal of Applied Physics*, 80(12):6839, 1996. 32

[60] R. Herberholz, M. Igalson, and H.W. Schock. Distinction between bulk and interface states in $CuInSe_2$/CdS/ZnO by space charge spectroscopy. *Journal of Applied Physics*, 83(1):318, 1998. 32

[61] J.L. Pautrat, B. Katircioglu, N. Magnea, D. Bensahel, J.C. Pfister, and L. Revoil. Admittance spectroscopy: A powerful characterization technique for semiconductor crystals - Application to ZnTe. *Solid-State Electronics*, 23(11):1159–1169, 1980. 32

[62] S.D. Baranovskii, T. Faber, F. Hensel, and P. Thomas. On the Einstein Relation for Hopping Electrons. *physica status solidi (b)*, 205(1):87–90, 1998. 33

[63] M Schmitt, U Rau, and J Parisi. Charge carrier transport via defect states in Cu(In,Ga)(Se,S)$_2$ thin films and Cu(In,Ga)(Se,S)$_2$/CdS/ZnO heterojunctions. *Phys. Rev. B*, 61(23):16052–16059, jun 2000. 33

[64] U. Reislöhner, H. Metzner, and C. Ronning. Hopping Conduction Observed in Thermal Admittance Spectroscopy. *Physical Review Letters*, 104(22):226403, 2010. 33

[65] P. Zabierowski and M. Igalson. Thermally assisted tunnelling in Cu(In,Ga)Se_2-based photovoltaic devices. *Thin Solid Films*, 361-362:268–272, feb 2000. 33

[66] G. Paasch, T. Lindner, and S. Scheinert. Variable range hopping as possible origin of a universal relation between conductivity and mobility in disordered organic semiconductors. *Synthetic Metals*, 132(1):97–104, dec 2002. 33

[67] N.F. Mott and E.A. Davies. *Electronic Processes in Non-Crystalline Materials*. Oxford University Press, London, 1979. 33

[68] J.H. Scofield. Effects of series resistance and inductance on solar cell admittance measurements. *Solar Energy Materials and Solar Cells*, 37(2):217–233, 1995. 33, 34, 40

[69] T.P. Weiss, A. Redinger, J. Luckas, M. Mousel, and S. Siebentritt. Admittance spectroscopy in kesterite solar cells: Defect signal or circuit response. *Applied Physics Letters*, 102(20):202105, 2013. 34

[70] W. Schottky. Halbleitertheorie der Sperrschicht. *Naturwissenschaften*, 26(52):843, 1938. 34

[71] A. Niemegeers and M. Burgelman. Effects of the Au/CdTe back contact on IV and CV characteristics of Au/CdTe/CdS/TCO solar cells. *Journal of Applied Physics*, 81(6):2881, 1997. 35

[72] T. Eisenbarth, T. Unold, R. Caballero, C.A. Kaufmann, and H.W. Schock. Interpretation of admittance, capacitance-voltage, and current-voltage signatures in Cu(In,Ga)Se_2 thin film solar cells. *Journal of Applied Physics*, 107(3):034509, 2010. 35, 59, 62

[73] W. Meyer and H. Neldel. Über die Beziehungen zwischen der Energiekonstanten ϵ und der Mengenkonstanten a in der Leitwertstemperaturformel bei oxydischen Halbleitern. *Zeitschrift für technische Physik*, 18(12):588–592, 1937. 36, 59, 102

[74] A. Yelon, B. Movaghar, and H.M. Branz. Origin and consequences of the compensation (Meyer-Neldel) law. *Physical Review B*, 46(19):12244–12250, 1992. 36

[75] A. Yelon, B. Movaghar, and R.S. Crandall. Multi-excitation entropy: its role in thermodynamics and kinetics. *Reports on Progress in Physics*, 69(4):1145, 2006. 36

[76] W. Greiner, L. Neise, and H. Stöcker. *Thermodynamics and Statistical Mechanics*. Springer-Verlag, New York, 1 edition, 1995. 36

[77] H. Eyring. The Activated Complex in Chemical Reactions. *The Journal of Chemical Physics*, 3(2):107, 1935. 36

[78] J.A.M. AbuShama, S.W. Johnston, R.S. Crandall, and R. Noufi. Meyer-Neldel rule and the influence of entropy on capture cross-section determination in Cu(In,Ga)Se_2. *Applied Physics Letters*, 87(12):123502, 2005. 37

[79] D. Abou-Ras, T. Kirchartz, and U. Rau. *Advanced Characterization Techniques for Thin Film Solar Cells*. Wiley-VCH Verlag GmbH & Co. KGaA, Weinheim, Germany, 2011. 39

[80] Hans Rau. Vapour composition and critical constants of selenium. *The Journal of Chemical Thermodynamics*, 6(6):525–535, 1974. 42

[81] G. Sauerbrey. Verwendung von Schwingquarzen zur Wägung dünner Schichten und zur Mikrowägung. *Zeitschrift für Physik*, 155(2):206–222, 1959. 42

[82] L. Assmann, J.C. Bernède, A. Drici, C. Amory, E. Halgand, and M. Morsli. Study of the Mo thin films and Mo/CIGS interface properties. *Applied Surface Science*, 246(1-3):159–166, jun 2005. 44

[83] N. Kohara, S. Nishiwaki, Y. Hashimoto, T. Negami, and T. Wada. Electrical properties of the Cu(In,Ga)Se2/ MoSe2/Mo structure. *Solar Energy Materials and Solar Cells*, 67(1-4):209–215, mar 2001. 44, 47

[84] A.M. Gabor, J.R. Tuttle, D.S. Albin, M.A. Contreras, R. Noufi, and A.M. Hermann. High-efficiency $CuIn_xGa_{1-x}Se_2$ solar cells made from $(In_x,Ga_{1-x})_2Se_3$ precursor films. *Applied Physics Letters*, 65(2):198, 1994. 44, 45

[85] R.R. Potter. Enhanced photocurrent ZnO/CdS/$CuInSe_2$ solar cells. *Solar Cells*, 16:521–527, jan 1986. 46

[86] U.P. Singh and S.P. Patra. Progress in Polycrystalline Thin-Film Cu(In,Ga)Se_2 Solar Cells. *International Journal of Photoenergy*, 2010:468147, 2010. 46

[87] L. Stolt, J. Hedström, J. Kessler, M. Ruckh, K.O. Velthaus, and H.W. Schock. ZnO/CdS/$CuInSe_2$ thin-film solar cells with improved performance. *Applied Physics Letters*, 62(6):597, 1993. 47

[88] M.B. Ård, K. Granath, and L. Stolt. Growth of Cu(In,Ga)Se_2 thin films by coevaporation using alkaline precursors. *Thin Solid Films*, 361-362:9–16, 2000. 47

[89] P.E. Russell. Properties of the Mo-$CuInSe_2$ interface. *Applied Physics Letters*, 40(11):995, 1982. 47

[90] W.N. Shafarman and J.E. Phillips. Direct current-voltage measurements of the Mo/$CuInSe_2$ contact on operating solar cells. In *Photovoltaic Specialists Conference, 1996., Conference Record of the Twenty Fifth IEEE*, pages 917–919, 1996. 47

[91] K. Orgassa, H.W. Schock, and J.H. Werner. Alternative back contact materials for thin film Cu(In,Ga)Se_2 solar cells. *Thin Solid Films*, 431-432:387–391, 2003. 47

[92] J.H. Scofield, A. Duda, D. Albin, B.L. Ballard, and P.K. Predecki. Sputtered molybdenum bilayer back contact for copper indium diselenide-based polycrystalline thin-film solar cells. *Thin Solid Films*, 260(1):26–31, 1995. 47

[93] M.A. Martínez and C. Guillén. Effect of r.f.-sputtered Mo substrate on the microstructure of electrodeposited $CuInSe_2$ thin films. *Surface and Coatings Technology*, 110(1-2):62–67, nov 1998. 47

[94] K.H. Yoon, S.K. Kim, R.B.V. Chalapathy, J.H. Yun, J.C. Lee, J. Song, and B.T. Ahn. Characterization of a Molybdenum Electrode Deposited by Sputtering and Its Effect on Cu(In,Ga)Se_2 Solar Cells. *Journal of the Korean Physical Society*, 45(4):1114–1118, 2004. 47

[95] D. Schmid, M. Ruckh, and H.W. Schock. A comprehensive characterization of the interfaces in Mo/CIS/CdS/ZnO solar cell structures. *Solar Energy Materials and Solar Cells*, 41-42:281–294, jun 1996. 47

[96] S.S. Li, B.J. Stanbery, C.H. Huang, C.H. Chang, Y.S. Chang, and T.J. Anderson. Effects of buffer layer processing on CIGS excess carrier lifetime: application of dual-beam optical modulation to process analysis [of solar cells]. In *Photovoltaic Specialists Conference, 1996., Conference Record of the Twenty Fifth IEEE*, pages 821–824, may 1996. 47

[97] M.A. Contreras, M.J. Romero, B. To, F. Hasoon, R. Noufi, S. Ward, and K. Ramanathan. Optimization of CBD CdS process in high-efficiency Cu(In,Ga)Se2-based solar cells. *Thin Solid Films*, 403-404:204–211, 2002. 47, 67

[98] U. Rau and M. Schmidt. Electronic properties of ZnO/CdS/Cu(In,Ga)Se2 solar cells - aspects of heterojunction formation. *Thin Solid Films*, 387(1-2):141–146, 2001. 47

[99] V. Deprédurand, Y. Aida, J.K. Larsen, T. Eisenbarth, A. Majerus, and S. Siebentritt. Surface treatment of solar cells grown under Cu-excess. *Proceedings of the 37th IEEE Photovoltaic Specialists Conference*, pages 874–877, 2011. 48, 66

[100] Y. Aida, V. Deprédurand, J.K. Larsen, H. Arai, T. Eisenbarth, M. Kurihara, A. Majerus, N. Fèvre, and S. Siebentritt. Improved CIS solar cells with absorbers grown under Cu-excess. In *Proceedings of the 26th European Photovoltaic Solar Energy Conference and Exhibition*, pages 2855 – 2859, 2011. 48, 68

[101] S. Siebentritt, L. Gütay, D. Regesch, Y. Aida, and V. Deprédurand. Why do we make Cu(In,Ga)Se_2 solar cells non-stoichiometric? *Solar Energy Materials and Solar Cells*, 119:18–25, 2013. 49

[102] P. Jackson, D. Hariskos, R. Wuerz, O. Kiowski, A. Bauer, T.M. Friedlmeier, and M. Powalla. Properties of Cu(In,Ga)Se_2 solar cells with new record efficiencies up to 21.7%. *physica status solidi - Rapid Research Letters*, 9(1):28–31, 2015. 49

[103] V. Probst, J. Palm, S. Visbeck, T. Niesen, R. Tölle, A. Lerchenberger, M. Wendl, H. Vogt, H. Calwer, W. Stetter, and F. Karg. New developments in Cu(In,Ga)(S, $Se)_2$ thin film modules formed by rapid thermal processing of stacked elemental layers. *Solar Energy Materials and Solar Cells*, 90(18-19):3115–3123, 2006. 49

[104] M. Powalla, M. Cemernjak, J. Eberhardt, F. Kessler, R. Kniese, H.D. Mohring, and B. Dimmler. Large-area CIGS modules: Pilot line production and new developments. *Solar Energy Materials and Solar Cells*, 90(18-19):3158–3164, 2006. 49

[105] E. Wallin, U. Malm, T. Jarmar, O.L.M. Edoff, and L. Stolt. World-record Cu(In,Ga)Se/*text*2 -based thin-film sub-module with 17.4% efficiency. *Progress in Photovoltaics: Research and Applications*, 20(7):851–854, 2012. 49

[106] V. Deprédurand, D. Tanaka, Y. Aida, M. Carlberg, N. Fèvre, and S. Siebentritt. Current loss due to recombination in Cu-rich $CuInSe_2$ solar cells. *Journal of Applied Physics*, 115(4):044503, 2014. 49, 50, 53

[107] M. Turcu, O. Pakma, and U. Rau. Interdependence of absorber composition and recombination mechanism in Cu(In,Ga)(Se,$S)_2$ heterojunction solar cells. *Applied Physics Letters*, 80(14):2598, 2002. 49, 50, 53

[108] P. Migliorato, J.L. Shay, H.M. Kasper, and S. Wagner. Analysis of the electrical and luminescent properties of $CuInSe_2$. *Journal of Applied Physics*, 46(4):1777, 1975. 49

[109] V. Deprédurand, T. Bertram, D. Regesch, B. Henx, and S. Siebentritt. The influence of Se pressure on the electronic properties of $CuInSe_2$ grown under Cu-excess. *Applied Physics Letters*, 105(17):172104, 2014. 49, 56, 61

[110] V. Deprédurand, T. Bertram, and S. Siebentritt. Influence of the Se environment on Cu-rich CIS devices. *Physica B: Condensed Matter*, 439:101–104, apr 2014. 49

[111] T. Bertram, V. Deprédurand, and S. Siebentritt. Electrical Characterization of Defects in Cu-Rich Grown CuInSe $_2$ Solar Cells. *IEEE Journal of Photovoltaics*, 6(2):546–551, 2016. 49

[112] ASTM. Reference Solar Spectral Irradiance: Air Mass 1.5, downloaded from: http://rredc.nrel.gov/solar/spectra/am1.5/, 2016. 52

[113] J. Tauc and A. Abrahám. Thermal Breakdown in Silicon $p - n$ Junctions. *Phys. Rev.*, 108(4):936–937, nov 1957. 53

[114] K.G. McKay. Avalanche Breakdown in Silicon. *Phys. Rev.*, 94(4):877–884, 1954. 53

[115] C. Zener. A Theory of the Electrical Breakdown of Solid Dielectrics. *Proceedings of the Royal Society of London. Series A, Containing Papers of a Mathematical and Physical Character*, 145(855):523–529, 1934. 53

[116] S. Lany and A. Zunger. Light- and bias-induced metastabilities in $Cu(In,Ga)Se_2$ based solar cells caused by the (V_{Se}-V_{Cu}) vacancy complex. *Journal of Applied Physics*, 100(11):113725, 2006. 56

[117] C. Persson, Y.J. Zhao, S. Lany, and A. Zunger. n-type doping of $CuInSe_2$ and $CuGaSe_2$. *Phys. Rev. B*, 72(3):35211, 2005. 56

[118] H. Oheda. Phase-shift analysis of modulated photocurrent: Its application to the determination of the energetic distribution of gap states. *Journal of Applied Physics*, 52(11):6693, 1981. 58

[119] Ch. Hurtes, M. Boulou, A. Mitonneau, and D. Bois. Deep-level spectroscopy in high-resistivity materials. *Applied Physics Letters*, 32(12):821, 1978. 58

[120] J.L. Pautrat. Electric field and impurity concentration effects on the ionization energy of impurities. Application to acceptors in ZnTe. *Solid-State Electronics*, 23(6):661–670, 1980. 59

[121] Susanne Siebentritt and Uwe Rau, editors. *Wide-Gap Chalcopyrites*, volume 86 of *Springer Series in Materials Science*. Springer-Verlag, Berlin/Heidelberg, Germany, 2006. 61

[122] A.F. Tasch and C.T. Sah. Recombination-generation and optical properties of gold acceptor in silicon. *Physical Review B*, 1(2):800–809, 1970. 61

[123] J. Camassel, P. Merle, H. Mathieu, and A. Chevy. Excitonic absorption edge of indium selenide. *Physical Review B*, 17(12):4718–4725, jun 1978. 66

[124] J. Herrero and J. Ortega. Electrochemical Synthesis of Photoactive In_2Se_3 Thin Films. *Solar Energy Materials*, 16:477–485, 1987. 66

[125] V. Deprédurand, T. Bertram, M. Thévenin, N. Valle, J.N. Audinot, and S. Siebentritt. Alternative Etching for Improved Cu-rich $CuInSe_2$ Solar Cells. *MRS Proceedings*, 1771:163–168, 2015. 78

[126] L. Choubrac, T. Bertram, H. ElAnzeery, and S. Siebentritt. Better Cu(In,Ga)Se_2 solar cells based on surface treated stoichiometric absorbers. *physica status solidi (a), submitted*, 2016. 78